Investigation into the Geodynamics of Planetary Ice-Ocean Systems

Application to Jupiter's Icy Moon Europa

by

Divya Allu Peddinti

A Dissertation Presented in Partial Fulfillment
of the Requirements for the Degree
Doctor of Philosophy

Approved August 2017 by the
Graduate Supervisory Committee:

Allen McNamara, Chair
Amanda Clarke
Steven Desch
Edward Garnero
Mikhail Zolotov

ARIZONA STATE UNIVERSITY

December 2017

ABSTRACT

The Jovian moon Europa's putative subsurface ocean offers one of the closest astrobiological targets for future exploration. It's geologically young surface with a wide array of surface features aligned with distinct surface composition suggests past/present geophysical activity with implications for habitability. In this body of work, I propose a hypothesis for material transport from the ocean towards the surface via a convecting ice-shell. Geodynamical modeling is used to perform numerical experiments on a two-phase water-ice system to test the hypotheses. From these models, I conclude that it is possible for trace oceanic chemistry, entrapped into the newly forming ice at the ice-ocean phase interface, to reach near-surface. This new ice is advected across the ice-shell and towards the surface affirming a dynamical possibility for material transport across the ice-ocean system, of significance to astrobiological prospecting. Next, I use these self-consistent ice-ocean models to study the thickening of ice-shell over time. Europa is subject to the immense gravity field of Jupiter that generates tidal heating within the moon. Analysis of cases with uniform and localized internal tidal heating reveal that as the ice-shell grows from a warm initial ocean, there is an increase in the size of convection cells which causes a dramatic increase in the growth rate of the ice-shell. Addition of sufficient amount of heat also results in an ice-shell at an equilibrium thickness. Localization of tidal heating as a function of viscosity controls the equilibrium thickness. These models are then used to understand how compositional heterogeneity can be created in a growing ice-shell. Impurities (e.g. salts on the surface) that enter the ice-shell get trapped in the thickening ice-shell by freezing. I show the distribution pattern of heterogeneities that can form within the ice-shell at different times. This may be of potential application in

identifying the longevity and mobility of brine pockets in Europa's ice-shell which are thought to be potential habitable niches.

DEDICATION

To Mum and Dad for all their patience, support, and humour, and my brother for the unceasing motivation.

ACKNOWLEDGMENTS

This work would not have come to fulfillment without the immense patience and the constant advice of my mentor, Allen McNamara. I would like to acknowledge his support and thank him for sharing valuable tricks and methods of scientific approach. I would also like to thank all the members of my supervising academic committee: Edward Garnero, Mikhail Zolotov, Steven Desch and Amanda Clarke for their criticism, suggestions, conversations and the encouragement.

I would like to thank all the members, particularly the staff, of the School of Earth and Space Exploration for the resources and the excellent work environment. Many thanks to Mark Stevens for the technical assistance and maintenance of the clusters. I would also like to acknowledge the staff at the ASU Noble Science Library for their excellent collection of books and journals, and their on- and off-line resources. They have all been critical in keeping the working mind stimulated.

I am grateful to the NASA Outer Planets Program for funding my research as well as supporting my attendance at several research conferences and workshops that have been valuable towards reviewing my work.

TABLE OF CONTENTS

Page

CHAPTER Page

APPENDIX Page

LIST OF TABLES

LIST OF FIGURES

PREFACE

Water, water, everywhere,
… Nor any drop to drink.

The Rime of the Ancient Mariner, S. T. Coleridge

Water is one of the essential constituents of life as we know it and thus "follow the water" has been the driving theme of astrobiology for several years. Although extreme (heat, chemical, pressure etc.) environments are known to harbor hardy forms of life, it is the icy moons and ocean planets that most excite the prospects of finding extraterrestrial life. However, it is not the mere presence of water but the circulation of dissolved mineral constituents and its accessibility to the surface that are essential to detecting any life on these watery planets. As alluded to by the lines from the classic poem quoted above, it is necessary to understand the dynamics of ice-ocean systems to determine their astrobiological potential. This dissertation aims to contribute towards understanding the physics of these seemingly ubiquitous ice bounded oceans in planetary systems. The scope of this work is limited to pure water-ice system and serves as a guide to the fundamental physics of this system in a planetary context.

Along with Neptune, I have always considered Jupiter as one of the most fascinating planetary bodies of our solar system due to its massive family of diverse moons, and its electrical phenomena. While the idea of alien life never seemed strange to me, that there exists an organized science to study it seemed fantastic. If the depths of our oceans harbor so many weird, varied and even intelligent life-forms, what then could be thriving in the alien seas? Volcanic Io has always been a personal favorite, but its icy, ruby-freckled sibling is just as enigmatic. It is the abode of the closest planetary subsurface ocean and it is imperative to understand this ice-ocean system in order to evaluate the potential of extraterrestrial life elsewhere in the cosmos. I hope this work emphasizes its significance.

I am forever indebted to my parents, and my brother for providing me the best education as well as allowing free reign of my career. I couldn't overstate the extent of their encouragement. My gratitude to the British Library at my hometown for drawing my attention to the wonders of art and science. I would like to thank the following people for all the small but significant joys: V, M, N, H, Si and all the bean-to-bar chocolate makers.

Stranger in a strange land
Land of ice and snow
Trapped inside this prison
… Preserved in time for all to see

Stranger in a Strange Land, A. F. Smith

CHAPTER 1

INTRODUCTION

Since time immemorial, humans have looked skywards with wonder and curiosity. Is the sky infinite? Are the stars indefinite? Are we alone? The technological and scientific advancements over the past few centuries have furthered this wonder and curiosity into an organized science based on observation and analysis. We are still awed by the grandeur of the universe albeit with a better sense of the scale and dynamics of it. Four centuries ago, when Galileo glanced through his telescope and identified the dance of four celestial objects around Jupiter [*Siderius Nuncius*, 1610], he discovered a miniature Solar System. In fact, it is hypothesized that the Galilean moon system accreted from a circumplanetary disk around Jupiter similar to the circumsolar disk [*Canup and Ward*, 2009]. Europa, the smallest of these four moons, was first visited by Pioneer [*Fimmel et al.*, 1974, 1980] and later, Voyager revealed detailed images of an intriguing moon with a putative subsurface ocean [*Smith et al.*, 1979; *Alexander et al.*, 2009]. The Galileo space-mission thereafter provided majority of the information we know about Europa, the ocean moon.

Four centuries after the discovery of the four Jovian moons and four decades of spacecraft visits later, the internal structure of Europa is well understood. However, critical questions related to its evolution and astrobiological potential still remain. Europa is a rocky moon, roughly 1562 km in radius, with a water envelope, a silicate mantle and an Fe-rich core [*Anderson et al., 1997*]. It has a geologically young surface with an average age < 100 Myr [*Zahnle et al.,* 2003]. The gravity data also indicate a global H_2O layer that is approximately 80-170 km thick [*Anderson et al.*, 1998; *Billings and*

Kattenhorn, 2005]. The detection of an induced magnetic signal [*Khurana et al.*, 1998; *Kivelson et al.*, 2000] revealed a possible global salty, subsurface ocean under an icy crust of debated thickness. Additionally, the observed geology such as ridges and bands also suggests the presence of a subsurface ocean [*Pappalardo et al.*, 1999]. Below, I will summarize what we know about this ice-ocean system focusing on the dynamics: heat and mass transfer across the system and the prevailing hypotheses and impending questions associated with it. I will briefly address its astrobiological potential and habitability before leading into a synthesis of how this knowledge motivated this dissertation and its results.

1.1 Geology of the Icy Surface

The icy surface of Europa is smooth and exhibits a sparsely cratered surface. Therefore, it is inferred that it has a geologically young surface [*Carr et al.*, 1998; *Zahnle et al.*, 2003], an indicator of a potentially active interior at least in the recent geological past. Additionally, it exhibits an array of surface features ranging from the ubiquitous ridges to the enigmatic chaotic terrains [*Greeley et al.*, 1998], suggestive of various geological processes. The spacecraft images together with spectral measurements also show visibly distinct non-ice material [*McCord et al.*, 1998; *Zolotov and Kargel*, 2009] concentrated at the several surface features. The observed geology and composition allows us to estimate the thickness of the ice-shell [*Carr et al.*, 1998; *Rathbun et al.*, 1998; *Pappalardo et al.*, 1999], and to speculate about the dynamics of the ice-ocean system. This is briefly discussed in the following sub-sections.

Surface Features and Stress Sources

The surface of a planetary body represents a net sum of all the forces, exterior and interior, experienced by the body over its geological history. Hence, it provides a glimpse into the interior dynamics, composition and potential habitability. Europa's surface features (figure 1.1) include ridges, bands, cycloids, pits, domes, spots, craters and chaotic terrains [*Greeley et al.*, 1998, 2000]. These geological features suggest the presence of less viscous material beneath the visible crust as well as the action of tectonic, and tidal forces, and other internal processes.

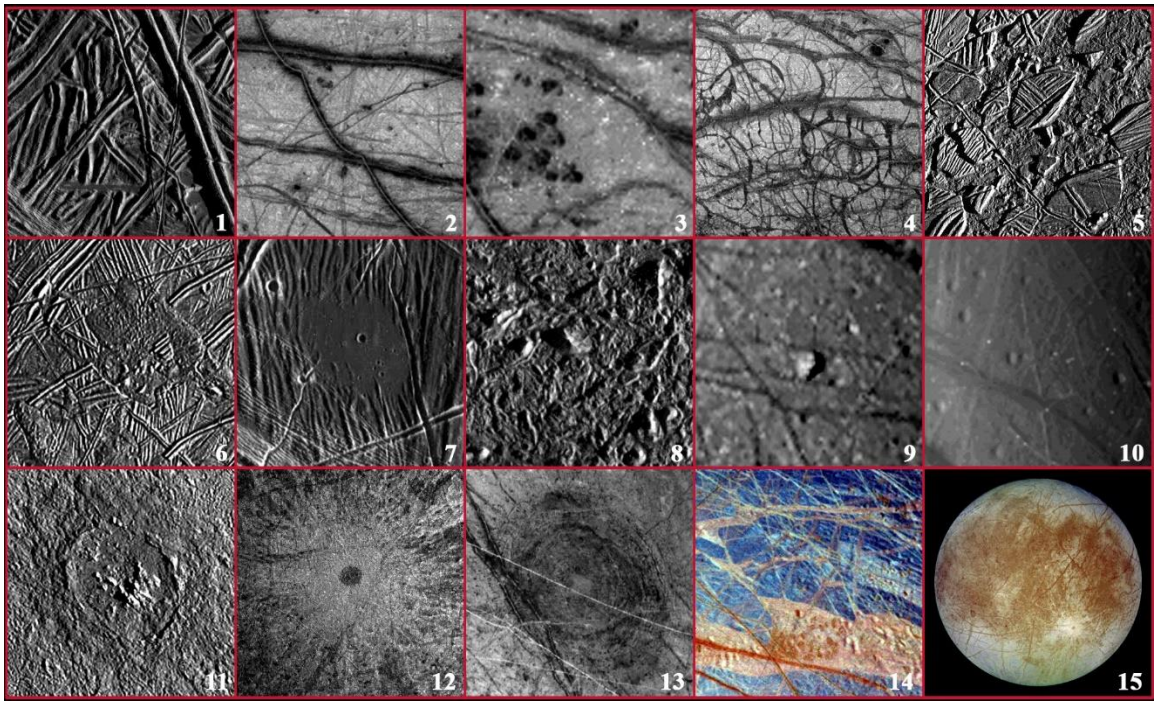

Figure 1.1. Examples of Surface Features of Europa (From *NASA/JPL*). Shown here are images captured by Galileo spacecraft's Solid State Imager at various resolutions. On the top row from left to right: 1. Ridges and lineaments, 2. Triple bands, 3. Dark spots, 4. Pull-apart terrain and 5. Raft terrain (chaos). In the middle row (from left to right): 6. Flows, 7. Puddle, 8. Mottled terrain, 9. Knobs and 10. Pits. The bottom row (from left to right): 11. Crater, 12. Crater ejecta, 13. Macula, 14. Infrared-Bright/Dark terrain. The rightmost image on the bottom shows a 15. Global view of Europa with several surface features forming the visibly distinct "red criss-cross" network. Features such as bands, pits and chaos indicate the possible presence of liquid water under the icy surface.

Pits, spots, domes and chaos regions have been speculated to be surface expressions of rising ice diapirs [*Pappalardo et al.,* 1998a; *Rathbun et al*., 1998]. They have also been suggested to be produced by water sills within the ice-shell [*Michaut and Manga*, 2014]. The chaotic terrain, consisting of blocks of crustal material in a hummocky matrix, is thought to have been formed by partial melting atop convective diapirs [*Figueredo et al*., 2002; *Schenk et al.*, 2004; *Collins et al.*, 2000; *Spaun et al.*, 1998; *Sotin et al.*, 2002] and more recently hypothesized to indicate collapse of the ice-crust over subsurface lakes [*Schmidt et al.*, 2011].

Ridges constitute the most morphologically common features on Europan surface and different types of ridges including double ridges and ridge complexes have been imaged. Several ridge formation mechanisms have been proposed including cryovolcanic processes [*Kadel et al*., 1998], wedging models [*Turtle et al.*, 1998] as well as upwarping by diapirism [*Head et al*., 1999]. The diurnal tidal stresses generated due to orbit around Jupiter are considered to be important in forming ridges via a process called *tidal pumping* similar to terrestrial sea ice whereby liquid water from ocean seeps through the shell and freezes on the surface [*Pappalardo and Coon*, 1996; *Greenberg et al*., 1998; *Tufts et al*., 2000]. Crystallization of liquid water intrusions such as sills within the ice-shell have also been proposed to form ridges on the surface [*Dombard et al.*, 2012; *Craft et al.*, 2013; *Johnston and Montesi*, 2014]. Ridges are often closely associated with bands which are also common features on Europa's surface. Tidal pumping mechanism [*Tufts et al*., 1999] as well as buoyancy driven mechanism [*Prockter et al*., 2002] similar to mid-ocean ridge spreading have been suggested for band formation. *Nimmo et al*. (2003)

suggested that thermal and/or compositional buoyancy in a thick ice-shell could also produce this topography.

The different mechanisms proposed to explain the observed surface deformation on Europa are driven by various stress sources. The sources of stress and strain rates include diurnal tides, non-synchronous rotation, impacts, and density variations [*Nimmo and Manga*, 2009]. Tectonic stresses are thought to be responsible for cracking the upper part of ice crust [*Lee et al*., 2005] and perhaps allow subsurface material to be exposed on the surface. The tidal stresses generated due to eccentric orbit around Jupiter are regarded as the key source of internal heating for sustaining a subsurface ocean and driving ice-shell convection that could lead to surface deformation.

In summary, competing hypotheses for explaining the surface geology require either a thin, conductive ice-shell [e.g. *Greenberg et al.*, 1998] or a thick, convecting ice-shell [e.g., *McKinnon*, 1999; *Pappalardo and Head*, 2001]. In this study, although I do not examine surface feature formation, I investigate, in chapter 4, how the ice-shell thickness changes with time and the effect of tidal heating on the growth rate of the shell. This work could have implications for predicting the formation of surface features at different times of ice-shell evolution on Europa.

Surface Composition

The surface of Europa possesses a high albedo indicating the dominant presence of water ice [*Kuiper*, 1957; *Pilcher et al.*, 1972; *McCord et al.*, 1998]. However, it also exhibits distinct non-ice components visible as the 'reddish brown stripes' crisscrossing its surface. Spectral measurements have revealed sulfur-rich materials thought to be delivered from Io via Jupiter's magnetosphere [*Carlson et al*., 2005; *Spencer et al.*,

2006]. However, it is also speculated that hydrated minerals are emerging from the deeper interior [*McCord et al*., 2002] which may be modified by radiolytic processes at the surface [*Moore et al.*, 2007]. The endogenic origin of surface material is thought to indicate not only the chemical composition of the ocean but also subsurface processes in the ice-ocean system that transport the material to the surface. Cryovolcanism is thought to operate on Europa providing a mechanism to transport oceanic material onto the surface [*Fagents*, 2003; *Carlson et al*., 2009]. For a thin ice-shell, cryovolcanic processes include melt-through mechanism assisted by tidal and tectonic cracking of the shell [*Greenberg et al*., 1999; *O'Brien et al.*, 2002]. In thicker ice-shells, warm plumes rising to the surface are suggested to transport oceanic material towards the surface [*Head and Pappalardo*, 1999; *Prockter et al*., 2002]. These models would still require a method to weaken the stagnant lid above the warm ice-layer in order for the material to reach onto the surface. Partial melting near the heads of warm diapirs leading to surface disruption has been suggested [*Sotin et al.*, 2002]. Terrestrial mantle convection models sometimes use a low viscosity *sticky air* approach [*Crameri et al.*, 2012] or plastic yielding at the surface to simulate tectonic plates [e.g., *Tackley*, 2000b]. Han et al. (2011) had introduced mechanical weakening of the ice-shell on Enceladus to allow evolution of hemispheric dichotomy in thermal convection. Similar methods can be employed to ice-convection models for Europa to deviate from a stagnant-lid convection regime [e.g., *Showman and Han*, 2005]; however in the scope of this dissertation, I examine the effect of an ice-ocean interface on transport of potential oceanic material towards the surface by ice-convection (chapter 3) via simple numerical experiments and choose not to impose any artificial weakening of the stagnant-lid.

1.2 Thickness of Ice-Shell

The thickness of the ice-shell on Europa remains uncertain [*Billings and Kattenhorn,* 2005]. The mechanism of material transport from the ocean to the surface and back depends on the thickness of the ice-shell. Since vertical transport of material from the ocean towards the surface could potentially transport microorganisms and biological nutrients, the thickness of the shell, which determines this vertical transport, also influences astrobiological detection [*Pappalardo and Head,* 2001]. The thickness of the ice-shell also determines the mode of ice deformation. At low stresses and strains, ice deforms elastically. However, the ice-shell of Europa mostly exhibits viscoelastic behavior. Its cold surface is brittle and it overlies an elastically deforming crust and the remaining lower portion of the ice-shell behaves in a ductile manner [*Watts,* 2001; *Nimmo and Manga,* 2009]. This has allowed modeling of convection in the ice-shell in a manner similar to terrestrial mantle convection. The viscoelastic behavior of ice is also used to estimate tidal dissipation in the ice that might control the ice-shell thickness over time. Presence of salty impurities in the ice, and salinity of the ocean would change the ice-viscosity and its melting behavior, which would also affect the ice-shell thickness.

Both thin and thick ice-shell models have been proposed to explain the formation of different morphological features of the icy-surface. Thin ice-shells (<10 km thick) are suggested by surface features such as cycloids and ridges and favor melt-through mechanisms [*Greenberg et al.*, 1998; *Rudolph and Manga,* 2009], as well as tectonic and tidal cracking [*Hoppa and Tufts,* 1999; *Hoppa et al.,* 1999a] of the crust. Thin-shell models are also invoked to support transport of oceanic material to the surface via direct emplacement onto the surface [e.g., *Greenberg and Geissler,* 2002]. Rising diapirs driven

by compositional and thermal buoyancy in thick ice-shells are thought to form chaotic terrains and domes [*Collins and Nimmo*, 2009], and allow material transport via advection [*Sotin et al.*, 2002]. Thus, a number of numerical and analytical models provide estimates of ice-shell thickness ranging from ~ 3 to 50 km [*Mitri and Showman*, 2005; *Billings and Kattenhorn*, 2005]. This uncertainty in shell thickness stems from poor constraints on material properties of ice such as its grain size and bulk modulus. Furthermore, a single ice-shell thickness cannot reconcile the size and age of all the observed surface features. For example, morphologies of large impact craters such as Tyre and Callanish indicate an ice-shell thicker than 20 km [Schenk, 2002]. The paucity of impact craters and the crater size-frequency-distribution of secondaries of Pwyll impact feature indicate a young age ~ 40-90 Myr [*Zahnle et al.*, 2003; *Bierhaus et al.*, 2001; *Schenk et al.*, 2004]. In contrast, some of the oldest material in the ridged plains is thought to have formed by tectonic processes in a thinner shell [*Greenberg et al.*, 1998; *Geissler et al.*, 1998b]. Therefore, investigating the time evolution of ice-shell thickness may provide a better approach towards predicting the current shell thickness as well as explain the pre-existing geology.

1.3 Dynamics of Ice-Ocean System

The H_2O layer of Europa has been inferred to consist of an ice-shell overlying a liquid water ocean. Depending on the thickness of the ice-shell, it is either primarily conducting or it is thick enough to convect. Tidal dissipation generated due to the eccentric Jovian orbit of Europa is an important heat source that drives the dynamics of the ice-ocean system. In addition to heat generated by any radioactive decay in its rocky interior, the tidal dissipation is expected to be an important factor in determining the thickness of the

ice-shell. Several studies explored the dynamics of a thin (~ 1-10 km) ice-shell over a thick ocean. In this dissertation, I examine different aspects of ice convection in a thick ice-shell overlying a liquid ocean.

Tidal Heating

Europa is are subject to strong tidal deformation as it orbits Jupiter. Solid tides are raised diurnally on Europa due to its eccentric orbit around Jupiter and due to its orbital resonance with Io and Ganymede [*Greenberg and Geissler*, 2002]. The tidal heating generated favors the presence of a subsurface ocean in Europa [*Ojakangas and Stevenson,* 1989; *Tobie et al.,* 2003]. Both the silicate interior and the ice-shell are subject to tidal stresses. The presence of a subsurface ocean decouples the ice-shell from the silicate interior and enhances the tidal dissipation distribution within the ice layer [*Tobie et al.,* 2005]. The tidal dissipation is a function of viscosity of ice and hence the rheology of ice determines the tidal deformation model used to determine the magnitude of the heating generated inside the ice-shell. For a Newtonian rheology with no grain-size dependence, ice on Europa behaves in a viscoelastic manner. Hence ice is modeled as a Maxwell viscoelastic material [*Ojakangas and Stevenson,* 1989; *Tobie et al.,* 2005]. This assumption is made while describing material relaxation times when the forcing period is close to their Maxwell time (ratio between the viscosity and shear modulus) [*Turcotte and Schubert,* 2002]. For Newtonian rheology of ice, Europa satisfies this criterion, and hence the Maxwell relaxation model is used to determine tidal dissipation as a function of viscosity of ice [*Sotin et al.,* 2009]. In reality, the ice viscosity is grain-size dependent and therefore Maxwell model only provides a first order approximation of tidal dissipation generated. Showman and Han (2004) performed numerical simulations of ice-

shell convection with tidal heating derived from the Maxwell model. They find that for pure thermal convection, the stresses generated are too small to generate surface features such as domes. Other convection models that incorporate Maxwell model, suggest runaway tidal heating within the plumes promoting partial melting and formation of features such as chaos [*Wang and Stevenson*, 2000; *Sotin et al.*, 2002; *Tobie et al.*, 2003]. Maxwell model in the above models is described to be appropriate to an ice-shell with no lateral variation in ice-viscosity, and hence warrants caution in applying the results to Europa [*Barr and Showman*, 2009]. Mitri and Showman (2008) modeled a variable ice viscosity structure and elastic parameters, with compressible Maxwell viscoelastic rheology to show that tidal heating is strongly temperature dependent within a convective plume supporting spatial localization of tidal heating in the ice-shell.

Thus, the tidal dissipation in ice is a strong function of temperature-dependent viscosity which may be variable in both space and time. Therefore, it would be predicted that change in temperature structure of ice-shell as it cools over time would change the viscosity and affect the magnitude of tidal dissipation in ice. Conversely, changes in amount of tidal dissipation in ice would be expected to affect the thickness of the ice-shell. Mitri and Showman (2005) examine the effect of perturbations in heat flux on ice-shell thickness. However, since their system is an ice-shell of fixed thickness, any dynamic feedback between the shell growth and tidal dissipation is only inferred but not observed. In chapter 4, I examine the effect of tidal dissipation in ice (both diffuse and localized modes) upon ice-shell growth rate as the shell forms from an initial ocean that cools over time.

Convection in the Ice-Shell

At the pressure and temperature regime of Europa, the behavior of a thick layer of ice can be likened to the behavior of rock in Earth's mantle. This has allowed numerical modeling of ice using the fluid dynamical methods used to study terrestrial mantle convection. Thermal buoyancy in ice is generated due to the temperature gradient across the shell. The temperature gradient causes warm ice to be less dense than cold ice. Thus, warm ice rises and cold ice sinks resulting in thermochemical advection. Presence of additional salts also adds compositional buoyancy to this convecting system. Ice-shells thicker than 10 km have been predicted to undergo solid-state convection once it exceeds a critical Rayleigh number [*Stengel et al*., 1982; *Pappalardo et al*., 1998; *Turcotte and Schubert*, 2002]. Numerical simulations of ice convection on Europa with temperature-dependent viscosity and tidal heating have suggested the formation of surface features such as pits [*Showman and Han*, 2004]. Thermochemical diapirism in ice has also been invoked to explain the formation of domes [*Pappalardo and Barr*, 2004]. Ice convection in the presence of salts can potentially produce large scale surface features [*Han and Showman*, 2005]. Inclusion of variable yield stresses in convection models suggests chaos formation [*Showman and Han*, 2005]. Strong-temperature dependent tidal heating within the rising convective plumes has been suggested to generate chaos terrain [*Wang and* Stevenson, 2000; Sotin *et al.*, 2002; *Tobie et al.*, 2003].

Tidal dissipation in ice has been suggested to vary across the ice-shell, and localized heating in a convecting shell is expected to produce partial melting [*Mitri and Showman*, 2008]. If tidal dissipation varies spatially, then as the ice-shell thickness changes we would expect it to be heterogeneous over time. Coupled convection models

have concluded that heterogeneous temperature structure can substantially affect tidal dissipation rate and hence the thermal convection in the ice-shell [*Han and Showman*, 2010; 2011]. These models do not consider a dynamically evolving ice-shell; however they examine ice-shells of different thicknesses for the effect of heterogeneous tidal dissipation. Mitri and Showman (2005) studied the effect of tidal heating rate on the conductive-convective transitions and the change in ice-shell thickness. They infer the changes in ice-shell thickness by extrapolating the results from the constant shell-thickness models. Their models do not include an ocean layer, thus prohibiting any dynamic evolution of the system.

The rheology of pure water-ice is an important factor in determining the style of ice convection. Viscosity of ice on Europa is dependent on the grain-size which is poorly constrained. Several numerical studies of ice-convection investigated the effect of rheology of ice for different creep mechanisms (grain sizes) [*Barr et al.*, 2004; *Barr and Pappalardo*, 2005*; Freeman et al.*, 2006; *Barr and McKinnon*, 2007]. The heat flow and thickness of a convecting shell has been calculated for variable grain sizes in order to constrain the best rheology of ice [*Ruiz and Tejero*, 2003; *Ruiz et al*., 2007]. The rheology of ice that is contaminated with non-ice material may suggest a different tidal dissipation model than the commonly used Maxwell model of tidal dissipation [*Barr and Showman*, 2009]. While a non-Newtonian rheology may be realistic for Europan ice over the geological timescale, the uncertainties in the material properties of ice (grain size etc.) only tend to complicate the numerical experiment by introducing more uncertainty. Therefore, for first order study of ice-ocean systems, it is sufficient to use the Newtonian rheology of ice [*McKinnon*, 1999].

All of the convection studies described above, while demonstrating important behaviors of ice convection do not consider the change in ice-shell thickness with time. The models employ a fixed ice-shell thickness; however few models infer the changes in the ice-shell thickness [e.g., *Mitri and Showman*, 2005]. In the chapters 3, 4, and 5 of this dissertation I explore different aspects of convection in an ice-shell that forms by freezing from an initial warm ocean based on the water-ice phase diagram. Thus, a dynamic shell thickness is achieved in these models which may be important in evaluating the effect of ice-ocean interface in the system as well as in determining temporal changes in ice-convection patterns as the shell grows.

1. 4 Astrobiology and Habitability

The detection of salts on Europa's surface is considered to be an indicator of water-silicate interaction and possible existence of hydrothermal systems, a potential abode for biology [*McCollom,* 1999]. Although the habitable environments are largely determined by ocean-silicate interactions and thus the composition of ocean, the dynamics of ice-shell determine the material circulation across the ice-ocean-silicate system and hence the possible detection of habitable environments within the ice-ocean system. It has also been speculated that regions in the ice-shell such as the fractures where melt-through can occur, or brine pockets within the ice-shell maybe suitable for life to exist [*Greenberg et al*., 2000; *Marion et al*., 2003; *Lipps and Rieboldt,* 2005]. Thermal diapirs generated by ice-convection and the lower parts of the stagnant lid are thought to be warm enough to be habitable as well [*Price,* 2003; *Ruiz et al*., 2007]. The preservation and detection of any potential biosignatures on the surface [*Figueredo et al.,* 2003] would also be determined by the thickness of the ice-shell [*Greenberg et al*., 2000; *Pappalardo and*

Head, 2001] and how it changes with time. Europa's habitability would thus depend on its thermochemical evolution which can be described as a synthesis of ice-ocean dynamics including compositional effects of brines, hydrothermal processes at water-rock interface, and chemical alteration at the surface besides the initial accretionary and differentiation processes [*Kargel et al.*, 2000]. The spacecraft detection of any bio-signatures at the surface would thus be related to the time evolution of ice-shell thickness and the timescales of material transport across it. In this dissertation study, I propose and demonstrate a simple hypothesis for material transport via ice convection as well as the entrapment of heterogeneities in a forming ice-shell (chapters 3 and 5).

1.5 Summary

Several morphological features on Europan surface as well as the observed surface composition can be explained via convection in a thick ice-shell and its interaction with the silicate interior via the liquid ocean in between. This dissertation employs a two-phase system consisting of an ice-shell upon a liquid ocean and addresses few aspects of ice-ocean systems that are expected to be influenced by advection in the ice-shell. Chapter 2 describes the governing equations of fluid dynamics, and numerical methods that are used in our geodynamical models. These models are modified to best represent the water-ice system as relevant to icy moons such as Europa. Chapter 3 describes the application of these geodynamical models to demonstrate the possible material transport across the ice-ocean system and towards the surface, via advection in ice. This study has potential implications for detection of oceanic material at the surface. Chapter 4 describes the methods and results of numerical experiments to investigate the effect of different modes of internal tidal heating on the ice-shell thickness and growth rate. This study

provides an insight into time evolution of ice-shell thickening, its freeze-over and equilibrium states. Using the two-phase models already developed, Chapter 5 describes the entrapment and distribution of heterogeneities within the ice-shell as the shell grows over time with potential applications for formation of brine inclusions in ice and their mobility in the ice-shell over time.

References

Alexander, C., Carlson, R., Consolmagno, G., Greeley, R., & Morrison, D. (2009). The Exploration history of Europa. In *Europa*, edited by Pappalardo, R. T., McKinnon, W. B., & Khurana, K. K. Tucson: University of Arizona Press, pp 3-26.

Anderson, J. D., Lau, E. L., Sjogren, W. L., Schubert, G., & Moore, W. B. (1997). Europa's differentiated internal structure: inferences from two Galileo encounters. *Science, 276,* 1236-1239.

Anderson, J. D., Schubert, G., Jacobsen, R. A., Lau, E. L., Moore, W. B., & Sjogren, W. L. (1998). Europa's differentiated internal structure: inferences from four Galileo encounters. *Science*, *281,* 2019-2022.

Barr, A. C., & McKinnon, W. B. (2007). Convection in ice I shells and mantles with self-consistent grain size. *J. Geophys. Res*., *112,* E02012, 10.1029/2006JE002781.

Barr, A. C., & Pappalardo, R. T. (2005). Onset of convection in the icy Galilean satellites: influence of rheology. *J. Geophys. Res., 110*, E12005, 10.1029/2004JE002371.

Barr, A. C., & Showman, A. P. (2009). Heat Transfer in Europa's icy shell. In *Europa*, edited by Pappalardo, R. T., McKinnon, W. B., & Khurana, K., pp. 405-430, Tucson: Univ. of Arizona Press.

Barr, A.C., Pappalardo, R.T., & Zhong, S. (2004). Convective instability in ice I with non- Newtonian rheology: Application to the icy Galilean satellites. *J. Geophys. Res*., *109,* doi:10.1029/2004JE002296.

Bierhaus, E. B., Chapman, C. R., Merline, W. J., Brooks, S. M., & Asphaug, E. (2001). Pwyll secondaries and other small craters on Europa. *Icarus*, *153,* 264-276.

Billings, S. E., & Kattenhorn, S. A. (2005). The great thickness debate: Ice shell thickness models for Europa and comparisons with estimates based on flexure at ridges. *Icarus, 177,* 397–412.

Canup, R.M., & Ward, W.R. (2009). *Origin of Europa and the Galilean Satellites*. In *Europa* edited by R. T. Pappalardo, W. B. McKinnon, and K. K. Khurana, pp. 431–451, Tucson: Univ. Arizona Press.

Carlson, R. W., Anderson, M. S., Mehlman, R., & Johnson, R. E. (2005). Distribution of hydrate on Europa: Further evidence for sulfuric acid hydrate. *Icarus, 177,* 461-471.

Carlson, R. W., Calvin, W. M., Dalton, J. B., Hansen, G. B., Hudson, R. L., Johnson, R. E., McCord, T. B., & Moore, M. H. (2009). Europa's Surface Composition. In *Europa* edited by R. T. Pappalardo, W. B. McKinnon, and K. K. Khurana, pp. 431–451, Tucson: Univ. Arizona Press.

Carr, M. H., et al. (1998). Evidence for a subsurface ocean on Europa. *Nature, 391*, 363-365.

Collins, G. C., Head, J. W., Pappalardo, R. T., & Spaun, N. A. (2000). Evaluation of models for the formation of chaotic terrain on Europa. *J. Geophys. Res., 105*, 1709-1716.

Collins, G. C., & Nimmo, F. (2009). Chaotic terrain on Europa. In *Europa* edited by R. T. Pappalardo, W. B. McKinnon, and K. K. Khurana, pp. 259–281, Tucson: Univ. Arizona Press.

Craft, K. L., Patterson, W. & Lowell, R. T. (2013). Sill emplacement in Europa's ice shell as a mechanism for double ridge formation. In 44th *Lunar and Planetary Science Conference,* Woodlands, Texas.

Crameri, F., Tackley, P. J., Meilick, I., Gerya, T. V., & Kaus, B. J. P. (2012). A free plate surface and weak oceanic crust produce single-sided subduction on Earth. *Geophys. Res. Lett., 39,* L03306, doi:10.1029/2011GL050046.

Dombard, A. J., Patterson, G. W., Lederer, A. P., & Prockter, L. M. (2012). Flanking fractures and the formation of double ridges on Europa. *Icarus*, *223*, 74-81.

Fagents, S. A. (2003). Considerations for effusive cryovolcanism on Europa: The post-Galileo perspective. *J. Geophys. Res., 108*(E12), 5139.

Figueredo, P. H., Chuang, F. C., Rathbun, J., Kirk, R. L., & Greeley, R. (2002). Geology and origin of Europa's mitten feature (Murias Chaos). *J. Geophys. Res., 107*, doi:10.1029/2001JE001591.

Fimmel, R. O., Swindell, W., & Burgess, E. (1974). *Pioneer Odyssey: Encounter with a Giant*. NASA SP-349, NASA Scientific and Technical Information Office, Washington, DC.

Fimmel, R. O., Van Allen, J. A., & Burgess, E. (1980). *Pioneer: First to Jupiter, Saturn and Beyond*. NASA SP-446, Washington DC.

Galilei, G. (1610). *Siderius Nuncius*. Translated by E. S. Carlos (1929) in *A Source Book in Astronomy* (H. Shapley and Howarth, ed.). New York: McGraw-Hill.

Geissler, P. et al. (1998b). Evolution of lineaments on Europa: clues from Galileo multispectral imaging observations. *Icarus, 135*, 107-126.

Greeley, R., et al. (1998). Europa: Initial Galileo geological observations. *Icarus, 135*, 4-24.

Greeley, R., et al. (2000). Geological mapping of Europa. *J. Geophys. Res., 105*, 22559-22578.

Greenberg, R., & Geissler, P. (2002). Europa's dynamic icy crust. *Meteoritics & Planetary Sci., 37*, 1685-1710.

Greenberg, R., Geissler, P., Hoppa, G., Tufts, B. R., Durda, D. D., Pappalardo, R., Head, J. W., Greeley, R., Sullivan, R., & Carr, M. H. (1998). Tectonic processes on Europa: tidal stresses, mechanical response, and visible features. *Icarus, 135*, 64-78.

Greenberg, R., Geissler, P., Tufts, B. R., & Hoppa, G. V. (2000). Habitability of Europa's crust: the role of tidal-tectonic processes. *J Geophys Res., 105*:17,551–17,562.

Greenberg, R., Hoppa, G. V., Tufts, B. R., Geissler, P., Riley, J., & Kadel, S. (1999). Chaos on Europa. *Icarus, 141,* 263–286.

Han, L., & Showman, A. P. (2005). Thermo-compositional convection in Europa's icy shell with salinity. *Geophys. Res. Lett., 32,* L20201, doi:10.1029/2005GL023979.

Han, L., & Showman, A. P. (2011). Coupled convection and tidal dissipation in Europa's ice shell using non-Newtonian grain-size-sensitivity (GSS) creep rheology. *Icarus, 212,* 262-267.

Han, L., & Showman, A.P. (2010). Coupled convection and tidal dissipation in Europa's ice shell. *Icarus,* doi:10.1016/j.icarus.2009.12.028.

Han, L., Tobie, G., & Showman, A. P. (2011). The impact of a weak south pole on thermal convection in Enceladus' ice shell. *Icarus, 218,* 320-330.

Head, J. W., & Pappalardo, R. T. (1999). Brine mobilization during lithospheric heating on Europa: Implications for formation of chaos terrain, lenticula texture, and color variations. *J. Geophys. Res., 104,* 27143-27155.

Head, J. W., Pappalardo, R. T., & Sullivan, R. (1999). Europa: Morphological characteristics of ridges and triple bands from Galileo data (E4 and E6) and assessment of a linear diapirism model. *J. Geophys. Lett., 104,* 24223-24235.

Hoppa, G. V., & Tufts, B. R. (1999). Formation of cycloidal features on Europa. In *Lunar and Planetary Science XXX*, Abstract #1599.

Hoppa, G. V., Tufts, B. R., Greenberg, R., & Geissler, P. E. (1999a). Formation of cycloidal features on Europa. *Science, 285,* 1899-1902.

Johnston, S. A., & Montesi, L. G. J. (2014). Formation of ridges on Europa above cyrstallizing water bodies inside the ice shell. *Icarus, 237,* 190-201.

Kadel, S. D., Fagents, S. A., Greeley, R., & the Galileo SSI Team. (1998). Trough-bounding ridge pairs on Europa – considerations for an endogenic model of formation. In *Lunar and Planetary Science XXIX*, Abstract #1078. Lunar Planetary Institute, Houston.

Kargel, J. S., Kaye, J. Z., Head, J. W., Marion, G. M., Sassen, R., Crowley, J. K., Ballesteros, O.P., Grant, S. A., & Hogenboom, D. L. (2000). Europa's crust and ocean: Origin, composition, and the prospects for life. *Icarus*, *148*, 226–265.

Khurana, K. K., Kivelson, M. G., Stevenson, D. J., Schubert, G., Russell, C. T., Walker, R. J., & Polanskey, C. (1998). Induced magnetic fields as evidence for subsurface oceans in Europa and Callisto. *Nature*, *395*, 777-780.

Kivelson, M. G., Khurana, K. K., Russell, C. T., Volwerk, M., Walker, R. J., & Zimmer, C. (2000). Galileo magnetometer measurements: a stronger case for a subsurface ocean at Europa. *Science*, *289*, 1340-1343.

Kuiper, G. P. (1957). Infrared observations of planets and satellites. *Astron. J.*, *62*, 291-306.

Lee, S., Pappalardo, R. T., & Makris, N. C. (2005). Mechanics of tidally driven fractures in Europa's ice shell. *Icarus*, *177*, 367-379.

Lipps, J. H., & Rieboldt, S. (2005). Habitats and taphonomy of Europa. *Icarus*, *177*, 515-527.

Marion, G. M., Fritsen, C. H., Eicken, H., & Payne, M. C. (2003). The search for life on Europa: limiting environmental factors, potential habitats, and Earth analogues. *Astrobiology*, *3*:785–811.

McCollom, T. M. (1999). Methanogenesis as a potential source of chemical energy for primary biomass production by autotrophic organisms in hydrothermal systems on Europa. *J. Geophys. Res.*, *104*(E12), 30729-30742.

McCord, T. B., Hansen, G. B., Fanale, F. P., Carlson, R. W., Matson, D. L., Johnson, T. V., Smythe, W. D., Crowley, J. K., Martin, P. D., Ocampo, A., Hibbitts, C. A.,

Granahan, J. C., and the NIMS team. (1998). Salts on Europa's surface detected by Galileo's near infrared mapping spectrometer. *Science, 280,* 1242-1245.

McCord, T. B., Teeter, G., Hansen, G. B., Sieger, M. T., & Orlando, T. M. (2002). Brines exposed to Europa surface conditons. *J. Geophys. Res., 107*(E1), 5004, 10.1029/2000JE001453.

McKinnon, W. B. (1999). Convective instability in Europa's floating shell. *Geophys. Res. Lett., 26,* 951-954.

Michaut, C., & Manga, M. (2014). Domes, pits, and small chaos on Europa produced by water sills. *J. Geophys. Res. Planets*., *119*, doi: 10.1002/2013JE004558.

Mitri, G., & Showman, A. P. (2005). Convective-conductive transitions and sensitivity of a convecting ice shell to perturbations in heat flux and tidal-heating rate: implications for Europa. *Icarus, 177,* 447-460.

Mitri, G., & Showman, A.P. (2008). A model for the temperature-dependence of tidal dissipation in convective plumes in icy satellites: Implications for Europa and Enceladus. *Icarus, 195,* 758–764.

Moore, M. H., Hudson, R. L., & Carlson, R. W. (2007). The radiolysis of SO_2 and H_2S in water ice: implications for the icy jovian satellites. *Icarus, 189,* 409-423.

Nimmo, F., & Manga, M. (2009). Geodynamics of Europa's ice shell. In *Europa after Galileo*, edited by Pappalardo, R. T., McKinnon, W. B., & Khurana, K., pp. 382–404, Tucson: Univ. of Arizona Press.

O'Brien, D. P., Geissler, P., & Greenberg, R. (2002). A melt-through model for chaos formation on Europa. *Icarus, 156,* 152–161.

Ojakangas, G. W., & Stevenson, D. J. (1989). Thermal state of an ice shell on Europa. *Icarus, 81,* 220-241.

Pappalardo, R. T., et al. (1998). Geological evidence for solid-state convection in Europa's ice shell. *Nature, 391*, 365–368.

Pappalardo, R. T., et al. (1999). Does Europa have a subsurface ocean? Evaluation of the geological evidence. *J. Geophys. Res., 104*(E10), 24015-24055.

Pappalardo, R. T., & Head, J. W. (2001). The thick-shell model of Europa's geology: implications for crustal processes. In *Lunar and Planetary Science Conference XXXII*, Abstract #1866. Lunar Planetary Institute, Houston.

Pappalardo, R., & Coon, M. D. (1996). A sea ice analog for the surface of Europa. In *Lunar and Planetary Science Conference XXVII*, pp. 997-998. Lunar Planetary Institute, Houston.

Pilcher, C. B., Ridgeway, S. T., & McCord, T. B. (1972). Galilean satellites: Identification of water frost. *Science, 178*, 1087-1089.

Price, P. B. (2003). Life in solid ice on Earth and other planetary bodies. In *Bioastronomy* 2002: Life among the stars. In: Norris R and Stootman F (eds) IAU Symposium series no. *213*, pp 363–366.

Prockter, L. M., Head, J., Pappalardo, R., Sullivan, R., Clifton, A. E., Gliese, B., Wagner, R., & Neukum, G. (2002). Morphology of Europan bands at high resolution: A mid-ocean ridge-type rift mechanism. *J. Geophys. Res. 107*, 1-26.

Rathbun, J. A., Musser, G., & Squyres, S. W. (1998). Ice diapirs on Europa: Implications for liquid water. *Geophys. Res. Lett., 25*, 4157–4160.

Rudolph, M. L., & Manga, M. (2009). Fracture penetration in planetary ice shells. *Icarus, 199*, 536-541.

Ruiz, J., Montoya, L., Lopez, V., & Amils, R. (2007). Thermal diapirism and the habitability of the icy shell of Europa. *Orig. Life. Evol. Biosph., 37*, 287-295.

Schenk, P. M., & Pappalardo, R. (2004). Topographic variations in chaos on Europa: implications for diapiric formation. *Geophys. Res. Lett., 31*, L1703, doi:10.1029/2004GL019978.

Schenk, P. M., Chapman, C. R., Zahnle, K. M., & Jeffrey, M. (2004). Ages and interiors: The cratering record of the Galilean satellites. *Jupiter: The Planet, Satellites and Magnetosphere* edited by Bagenal, F. et al. Cambridge: Cambridge Univ., pp. 427-456.

Schmidt, B. E., Blankenship, D. D., Patterson, G. W., & Schenk, P. M. (2011). Active formation of "chaos terrain" over shallow subsurface water on Europa. *Nature, 479*, 502–505.

Showman, A. P., & Han, L. (2004). Numerical simulations of convection in Europa's ice shell: implications for surface features. *J. Geophys. Res., 109*, E01010.

Showman, A.P., & Han, L. (2005). Effects of plasticity on convection in an ice shell: Implications for Europa. *Icarus, 177*, 425–437.

Smith, B. A., & the Voyager Imaging Team. (1979). The Galilean satellites of Jupiter: Voyager 2 imaging science results. *Science, 206,* 951-972.

Sotin, C., Head III, J. W., & Tobie, G. (2002). Europa: Tidal heating of upwelling thermal plumes and the origin of lenticulae and chaos melting. *Geophys. Res. Lett., 29*(23), 2109, doi:10.1029/2001GL013884.

Spaun, N. A., Head, J. W., Collins, G. C., Prockter, L. M., & Pappalardo, R. T. (1998). Conamara chaos region, Europa: Reconstruction of mobile polygonal ice blocks. *Geophys. Res. Lett., 25*, 4277–4280.

Spencer, J. R., Grundy, W. M., Dumas, C., Carlson, R. W., McCord, T. B., Hansen, G. B., & Terrile, R. J. (2006). The nature of Europa's dark non-ice surface material: spatially resolved high spectral resolution spectroscopy from the Keck telescope. *Icarus, 182*, 202-210.

Stengel, K. C., Oliver, D. S., & Booker, J. R. (1982). Onset of convection in a variable-viscosity fluid. *J. Fluid Mech., 120*, 411-431.

Tackley, P. J. (2000b). Self-consistent generation of tectonic plates in time-dependent, three-dimensional mantle convection simulations. 1. Pseudoplastic yielding. *Geochem. Geophys. Geosyst., 1*, 2000GC000036.

Tobie, G., Choblet, G., & Sotin, C. (2003). Tidally heated convection: Constraints on Europa's ice shell thickness. *J. Geophys. Res., 108*(E11), 5124, doi:10.1029/2003JE002099.

Tobie, G., Mocquet, A., & Sotin, C. (2005). Tidal dissipation within large icy satellites: Applications to Europa and Titan. *Icarus, 177*, 534-549.

Tufts, B. R., Greenberg, R., Hoppa, G., & Geissler, P. (1999). Astypalaea Linea: A large scale strike-slip fault on Europa. *Icarus*, *141*, 53-64.

Tufts, B. R., Greenberg, R., Hoppa, G., & Geissler, P. (2000). Lithospheric dilation on Europa. *Icarus*, *146*, 75-97.

Turcotte, D. L., & Schubert, G. (2002). Geodynamics: Applications of Continuum Physics to Geological Problems. New York: Wiley.

Turtle, E. P., Melosh, H. J., & Phillips, C. B. (1998). Tectonic modeling of the formation of europan ridges. *Eos Trans. AGU*., *79*, F541.

Wang, H., & Stevenson, D. J. (2000). Convection and internal melting of Europa's ice shell. In *Lunar and Planetary Science XXXI*, Abstract #1293. Houston: Lunar and Planetary Institute.

Watts, A. B. (2001). *Isostasy and Flexure of the Lithosphere*. Cambridge: Cambridge Univ.

Zahnle, K., Schenk, P., Levison, H., & Dones, L. (2003). Cratering rates in the outer solar system. *Icarus*, *163*, 263-289.

Zolotov, M. Y., & Kargel, J. S. (2009). On the chemical composition of Europa's icy shell, ocean, and underlying rocks. *Europa*, edited by Pappalardo, R. T., McKinnon, W. B., & Khurana, K. K. Tucson: University of Arizona Press, pp 431-451.

CHAPTER 2

GOVERNING EQUATIONS OF FLUID DYNAMICS

In this chapter, I describe the main equations of fluid dynamics that are solved by the numerical methods. The numerical methods that are used in performing the geodynamical experiments are also summarized.

In fluid dynamics, in a given domain, we mainly track the velocity field that describes the flow. We compute the temperature and viscosity in order to solve the velocity and pressure of each fluid parcel designated as an element. The numerical solvers perform this operation iteratively until we solve the equations of fluid flow to the required accuracy. The basic equations of fluid flow treat the fluid as a continuum since the phenomena we study in our numerical models are macroscopic. This allows us to assign an average velocity and density to our fluid elements and ignore the fluctuations at the molecular level.

Conservation Laws

The fundamental theorem of calculus states that the sum of infinitesimal changes in a quantity over space adds up to the net change in the quantity. Thus, equation of conservation of a quantity is equivalent to computing the sum of all fluxes. In order to compute the flow of heat and mass within the domain, the numerical methods iteratively solve the equations of conservation of mass, momentum and energy. These three equations can be described as follows.

The law of conservation of mass states that the mass of a closed system will remain constant over time. In differential form, for a given volume, the continuity equation can be written as,

$$\frac{\partial \rho}{\partial t} + \nabla \bullet (\rho \vec{u}) = 0 \qquad 2.1$$

Where ρ is the density, t is time and $\vec{u}$ is the velocity.

[1] In a steady state situation such as a constant flow field, $\frac{\partial \rho}{\partial t} = 0$ and therefore, the equation of conservation of mass simplifies to $\nabla \bullet (\rho \vec{u}) = 0$ 2.2

[2] When density remains constant, i.e. for an incompressible fluid, $\frac{\partial \rho}{\partial t} = 0$ and $\nabla \rho = 0$.

The equation 2.1 now becomes, $\nabla \bullet \vec{u} = 0$ 2.3

For a general scalar function of time and position, $f(x, t)$, we can define the total derivative or the material derivative as,

$$\frac{Df}{Dt} = \frac{\partial f}{\partial t} + \vec{u} \bullet \nabla f \qquad 2.4$$

Thus, equation 2.1 can also be written as,

$$\frac{D\rho}{Dt} + \rho \bullet \nabla \vec{u} = 0 \qquad 2.5$$

Equation 2.1 is the Eulerian form of the law, which monitors the flow characteristics in a fixed control volume and is better suited for fluid dynamics (computing velocity etc.). Equation 2.5 is in the Langrangian form, which is useful in tracking individual particles in a flow field and is better suited for position tracking etc. The law of conservation of momentum states that if no external forces act on a closed system of objects, the momentum remains the same. Thus,

Rate of change of momentum within a volume = Rate of momentum entering/leaving the volume + External forces applied to the volume

Alternatively, as the Newton's second law of motion states, the imbalance of forces on a fluid parcel results in the acceleration of the parcel.

Therefore,

$$\rho \frac{D\vec{u}_i}{Dt} = -\frac{\partial p}{\partial x_i} + \frac{\partial \tau_{ij}}{\partial x_j} + \rho g_i \qquad 2.6$$

Where ρ is the density and $\vec{u}$ is the velocity vector; thus this term indicates the net force on the fluid parcel due to its acceleration. On the right side of the equation, p is the pressure, τ_{ij} is the deviatoric stress tensor, and g is the acceleration due to gravity; t is the time and x is the position coordinate.

In fluid flow, the forces include stresses (hydrostatic and dynamic pressure as well as viscous stresses) and buoyancy force (body force) as expressed in the three terms on the right in equation 2.6 in that order. If we expand this equation, we get,

$$\rho\left(\frac{\partial \vec{u}}{\partial t} + (\vec{u}\cdot\nabla)\vec{u}\right) = -\nabla p - \nabla\cdot\bar{\bar{\tau}} + \rho\vec{g} \qquad 2.7$$

The terms on the left are the inertial forces and the terms on the right constitute stress forces as described above. Specifically, $\frac{\partial \vec{u}}{\partial t}$ is the unsteady term, and $(\vec{u}\cdot\nabla)\vec{u}$ is the convective acceleration. While p and τ describe the pressure and viscous/elastic forces respectively, $\rho\,\vec{g}$ is the buoyancy or driving force in fluid flow.

Equation 2.7 is referred to as the Navier-Stokes equation of fluid flow. The stress terms can be expanded further in order to obtain different functional forms of this equation to describe fluid flow as applicable to different flow problems. For an elastic material, the deviatoric stress (τ) is related to strain ($\dot{\varepsilon}$) while for viscous fluid flow, it is related to strain-rate ($\bar{\bar{\dot{\varepsilon}}}$).

The linearized strain rate tensor, $\overline{\overline{\dot{\varepsilon}}}$ can be defined in terms of velocity components in x- and y-directions as follows,

$$\overline{\overline{\dot{\varepsilon}}} = \begin{pmatrix} 2\frac{\partial u_x}{\partial x} & \frac{\partial u_x}{\partial y} + \frac{\partial u_y}{\partial x} \\ \frac{\partial u_y}{\partial x} + \frac{\partial u_x}{\partial y} & 2\frac{\partial u_y}{\partial y} \end{pmatrix} \tag{2.8}$$

$$\overline{\tau} = -\overline{\overline{\eta}}\,\overline{\overline{\dot{\varepsilon}}} \tag{2.9}$$

The negative sign is due to the convention for stress direction (in this case, the stresses are pointing inwards).

Therefore equation 2.7 for fluid deformation becomes,

$$\rho\left(\frac{\partial \vec{u}}{\partial t} + (\vec{u}\cdot\nabla)\vec{u}\right) = -\nabla p + \nabla\cdot\overline{\overline{\eta}}\,\overline{\overline{\dot{\varepsilon}}} + \rho\vec{g} \tag{2.10}$$

Where $\overline{\overline{\eta}}$ is the viscosity tensor.

For a material with isotropic viscosity, the viscosity tensor reduces to a scalar value. Thus,

$$\rho\left(\frac{\partial \vec{u}}{\partial t} + (\vec{u}\cdot\nabla)\vec{u}\right) = -\nabla p + \nabla\cdot\eta\,\overline{\overline{\dot{\varepsilon}}} + \rho\vec{g} \tag{2.11}$$

We can define a static reference model which consists of a reference fluid at some constant, reference temperature T_R that experiences hydrostatic compression. Let's also define a reference gravitational acceleration, $\vec{g}_R$ and, a reference density ρ_R. Hence the sum of these reference values and the respective deviatoric values would be equal to the actual value of the parameter. Therefore,

$$\left.\begin{aligned} p &= p_R + \tilde{p} \\ \rho &= \rho_R + \tilde{\rho} \\ \vec{g} &= \vec{g}_R + \tilde{\vec{g}} \end{aligned}\right\} \qquad 2.12$$

The deviatoric values are indicated with a ~ symbol and these deviations are easy to compute numerically while solving the fluid flow. Also, density is a function of hydrostatic pressure, which is a function of depth and increases in the direction of $\vec{g}_R$. Thus,

$$\nabla \cdot p_R = \rho_R \vec{g}_R \qquad 2.13$$

When we substitute equations 2.12 and 2.13 into the equation 2.11, we find that hydrostatic pressure plays no role in convection and the equation 2.11 simplifies to,

$$\rho\left(\frac{\partial \vec{u}}{\partial t} + (\vec{u}\cdot\nabla)\vec{u}\right) = -\nabla\tilde{p} + \nabla\cdot\eta\dot{\tilde{\varepsilon}} + \rho_R\tilde{\vec{g}} + \tilde{\rho}\vec{g}_R + \tilde{\rho}\tilde{\vec{g}} \qquad 2.14$$

The dynamic pressure, $\tilde{p}$ is the non-hydrostatic component of pressure and drives the convection. Thereafter we refer to $\tilde{p}$ as *P*, the dynamic pressure. In equation 2.14, the terms consisting of $\tilde{\vec{g}}$ are neglected since the real value of $\vec{g} = \vec{g}_R$. The equation for conservation of momentum can thus be written as,

$$\rho\left(\frac{\partial \vec{u}}{\partial t} + (\vec{u}\cdot\nabla)\vec{u}\right) = -\nabla P + \nabla\cdot\eta\dot{\tilde{\varepsilon}} + \tilde{\rho}\vec{g}_R \qquad 2.15$$

Now, we examine the law of conservation of energy which states that the internal energy of an object is the net sum of the heat transferred to the object and the work done by the object. Therefore, if we consider an infinitesimal element in a fixed space (Eulerian frame), we can express the change in its total energy over an infinitesimal time

as the net sum of energy advected and conducted and the work done by the element. Thus, we can write the equation for conservation of energy as,

$$\rho \frac{DU}{Dt} = \nabla \cdot (k \nabla T) + \overline{\overline{\theta}} : \nabla \vec{u} + \rho H \qquad 2.16$$

Where ρ is the density, U is the internal energy, k is the thermal conductivity, T is the temperature, $\overline{\overline{\theta}}$ is the stress tensor and $\vec{u}$ is the velocity. H is the rate of internal heat production per unit mass.

From the principles of thermodynamics, $dU = TdS - PdV$ 2.17

Where U is the internal energy, T is the temperature, S is the entropy, P is the pressure, and V is the specific volume. Specific volume is a function of density, ρ and thus, equation 2.16 can be written as,

$$\rho T \frac{DS}{Dt} = \nabla \cdot (k \nabla T) + \frac{P}{\rho} \frac{d\rho}{dt} + \overline{\overline{\theta}} : \nabla \vec{u} + \rho H \qquad 2.18$$

Further, entropy is a function of temperature and pressure. So,

$$\frac{DS}{Dt} = \frac{c_p}{T} \frac{DT}{Dt} - \frac{\alpha}{\rho} \frac{Dp}{Dt} \qquad 2.19$$

Where c_p is the temperature-dependent specific heat capacity at constant pressure and α is the coefficient of thermal expansion.

In equation 2.18, the pressure terms from the full stress tensor are removed. This reduces the stress term to viscous dissipation or frictional heating described by ϕ. Thus after further simplification, the thermal energy equation now becomes,

$$\rho c_p \frac{DT}{Dt} = \nabla \cdot (k \nabla T) + \alpha T \frac{Dp}{Dt} + \phi + \rho H \qquad 2.20$$

On the left side, we have the advection term together with the time-dependent term. On the right side of the equation, we have the conduction term, the adiabatic term together with the viscous dissipation and heat production terms in that order.

Recalling equation 2.12, we have $p = p_R + \tilde{p}$

$$\frac{Dp}{Dt} = \frac{Dp_R}{Dt} + \frac{D\tilde{p}}{Dt} = \frac{\partial p_R}{\partial t} + \vec{u} \cdot \nabla p_R + \frac{D\tilde{p}}{Dt} \qquad 2.21$$

Since reference pressure is independent of time, $\frac{\partial p_R}{\partial t} = 0$. Also from equation 2.13,

$\nabla \cdot p_R = \rho_R \vec{g}_R$ and since $\vec{g} = \vec{g}_R$ and we use the unit vector in *z*-direction, we have,

$$\frac{Dp}{Dt} = \vec{u}_z \rho_R \vec{g}_z + \frac{D\tilde{p}}{Dt} \qquad 2.22$$

Therefore, equation 2.20 can be written as,

$$\rho c_p \frac{DT}{Dt} = \nabla \cdot (k \nabla T) + \alpha T \left(\vec{u}_z \rho_R \vec{g}_z + \frac{D\tilde{p}}{Dt} \right) + \phi + \rho H \qquad 2.23$$

Since in our reference frame gravity is always measured in the z-direction, we can drop the subscript for the gravity term and use a scalar *g* value. Hence, the dimensional form of the equations for the three laws of conservation of mass, momentum and energy for an incompressible fluid are as follows:

Conservation of mass: $\nabla \bullet \vec{u} = 0$

Conservation of momentum: $\rho\left(\frac{\partial \vec{u}}{\partial t} + (\vec{u} \cdot \nabla)\vec{u}\right) = -\nabla P + \nabla \cdot \eta \dot{\bar{\varepsilon}} + \tilde{\rho} g$

Conservation of energy: $\rho c_p \frac{DT}{Dt} = \nabla \cdot (k \nabla T) + \alpha T\left(\vec{u}_z \rho_R g + \frac{D\tilde{p}}{Dt}\right) + \phi + \rho H$

2.24

The numerical solvers solve the non-dimensional forms of the above equations. Non-dimensionalisation allows us to scale (up/down) the problem and also produces certain non-dimensional parameters such as Rayleigh number that are used to describe the characteristics of the fluid flow. The non-dimensionalisation of these equations is described below.

Non-Dimensionalisation of Equations

In order to non-dimensionalize the equations in 2.24, we introduce the following variable transformations. The prime $'$ notation indicates the non-dimensional form of variable while the unprimed notation indicates the dimensional value.

Density: $\rho = \rho_0 \rho'$ 2.25

Viscosity: $\eta = \eta_0 \eta'$ 2.26

Temperature: $T = \Delta T T'$ 2.27

Velocity: $u = \frac{\kappa_0}{h} u'$ 2.28

Pressure: $p = \frac{\eta_0 \kappa_0}{h^2} p'$ 2.29

Strain rate: $\dot{\bar{\varepsilon}} = \frac{\kappa_0}{h^2} \dot{\bar{\varepsilon}}'$ 2.30

Time: $$t = \frac{h^2}{\kappa_0} t' \qquad 2.31$$

Heat: $$H = \frac{\kappa_0 c_{p_0} \Delta T}{h^2} H' \qquad 2.32$$

Additionally,

$$\nabla = \frac{1}{h} \nabla' \qquad 2.33$$

$$\kappa = \kappa_0 \kappa' \qquad 2.34$$

$$\alpha = \alpha_0 \alpha' \qquad 2.35$$

$$c_p = c_{p_0} c'_p \qquad 2.36$$

Where ρ_0, η_0, κ_0, α_0, and c_{p0} are the reference values of density, viscosity, thermal diffusivity, thermal expansivity, gravity and specific heat capacity respectively; *h* refers to the thickness of the system while ΔT is the temperature difference across the system (between the surface and the base of the system).

Using the variable transformations given by equations 2.25-2.36, we obtain the non-dimensional equations of the conservation laws given in equation 2.24. Therefore, we have,

$$\left.\begin{aligned} &\nabla' \cdot \vec{u}' = 0 \\ &\frac{1}{\mathrm{Pr}} \rho' \left(\frac{\partial \vec{u}'}{\partial t'} + (\vec{u}' \cdot \nabla') \vec{u}' \right) = -\nabla' p' + \nabla' \cdot \eta' \dot{\bar{\varepsilon}}' + \frac{h^3}{\eta_0 \kappa_0} \tilde{\rho} g \\ &\rho' c'_p \frac{DT'}{Dt'} = \rho' c'_p \nabla' \cdot (\kappa' \nabla' T') + Di \alpha' T' \left(\vec{u}'_z \rho_R + \frac{\alpha \Delta T}{Ra} \frac{Dp'}{Dt'} \right) + \frac{Di}{Ra} \phi' + \rho' H' \end{aligned}\right\} \qquad 2.37$$

In the above equations, we have three non-dimensional parameters, each of which is a collection of constants, which describe different characteristics of fluid flow.

$$\text{Prandtl Number, } \mathrm{Pr} = \frac{\eta_0}{\rho_0 \kappa_0} \tag{2.38}$$

The Prandtl number is a ratio of the heat flux to conductive heat flux and compares the diffusion of momentum and heat.

$$\text{Dissipation Number, } Di = \frac{\alpha_0 g h}{c_{p_0}} \tag{2.39}$$

The dissipation number is the ratio of the depth to the temperature scale height that governs the amount of non-dimensional viscous dissipation and adiabatic heating (energy eq. in 2.37).

$$\text{Rayleigh Number, } Ra = \frac{\alpha_0 \rho_0 g \Delta T h^3}{\kappa_0 \eta_0} \tag{2.40}$$

The Rayleigh number provides a measure of the convective vigor of the fluid.

Approximate Equations

We can further simplify the non-dimensional equations in 2.37 according to the specific flow problem being studied. Thus, we can obtain problem-specific approximations that are then solved by the numerical solver.

Infinite Prandtl Number Approximation: For terrestrial silicate mantle convection, the Prandtl number (*Pr*), computed from equation 2.38 is approximately 10^{23}. For this study, we compute the value of $Pr \sim 10^{19}$ for ice on Europa (assuming $\eta \sim 10^{16}$ Pa-s and $\rho \sim 917$ kg m^{-3}). Therefore on the left hand side of the equation for momentum conservation in

2.37, we apply the infinite Pr number approximation, according to which the coefficient of inertia term is so small that the inertia can be neglected. Hence, since $1/Pr \sim 0$, the non-dimensional equation for momentum conservation reduces to the non-dimensional *Stokes Equation* given by,

$$-\nabla' p' + \nabla' \cdot \eta' \dot{\bar{\bar{\varepsilon}}}' + \frac{h^3}{\eta_0 \kappa_0} \tilde{\rho} g = 0 \qquad 2.41$$

Furthermore, the deviatoric density or the density anomaly can be defined as,

$$\tilde{\rho} = \Delta\rho C - \alpha \Delta T T \rho_R + \frac{\tilde{p}}{k_B} \rho_R \qquad 2.42$$

Where C is a non-dimensional variable such that $C = 0$ if the density is ρ, and $C = 1$ if the density is ρ' i.e. it is the fraction of dense material.

Therefore, using the variable transformations, equation 2.41 becomes,

$$-\nabla' p' + \nabla' \cdot \eta' \dot{\bar{\bar{\varepsilon}}}' + \left(\frac{\Delta\rho C h^3 g}{\eta_0 \kappa_0} \right) \hat{z} - \left(\frac{\alpha_0 \rho_0 g \Delta T h^3}{\eta_0 \kappa_0} \right) \alpha' \rho' T \hat{z} + \left(\frac{h^3 g \rho_0}{\eta_0 \kappa_0 k_B} \right) \rho' \tilde{p} \hat{z} = 0 \qquad 2.43$$

Where $\hat{z}$ is the unit vector for direction of gravity, g. We substitute the non-dimensional parameters (eq. 2.38-2.40) for the collection of constants within the parentheses and introduce another non-dimensional parameter called the buoyancy number that is a measure of density. Thus,

$$-\nabla' p' + \nabla' \cdot \eta' \dot{\bar{\bar{\varepsilon}}}' + RaBC\hat{z} - RaT\alpha' \rho' \hat{z} + \left(\frac{h^3 g \rho_0}{\eta_0 \kappa_0 k_B} \right) \tilde{p} \hat{z} = 0 \qquad 2.44$$

Where Buoyancy Number, $B = \dfrac{\Delta\rho}{\rho_0 \alpha_0 \Delta T}$ 2.45

Equation 2.44 is the non-dimensional momentum conservation equation under the *Anelastic Liquid Approximation* (*ALA*). The term *anelastic* refers to setting the term $\partial\rho/\partial t$ equal to zero in the mass conservation equation, thus excluding the propagation of sound waves.

Now, we assume that the dynamic pressure has only a negligible impact on density and thus, $\tilde{p} \sim 0$. This is the *Truncated Anelastic Liquid Approximation* (*TALA*).

$$-\nabla' p' + \nabla' \cdot \eta' \dot{\bar{\bar{\varepsilon}}}' + RaBC\hat{z} - RaT\alpha'\rho'\hat{z} = 0 \qquad 2.46$$

For an incompressible fluid, since there is no compression, $\rho = \rho_0$ and thus, $\rho' = 1$. This is the *Extended Boussinesq Approximation* (*EBA*).

$$-\nabla' p' + \nabla' \cdot \eta' \dot{\bar{\bar{\varepsilon}}}' + RaBC\hat{z} - RaT\alpha'\hat{z} = 0 \qquad 2.47$$

Boussinesq Approximation (*BA*): Under this approximation the non-dimensional values of ρ', α', c_p' and κ' are all constant i.e equal to one. Also, the dissipation number, *Di* ~ 0 (the high viscosity of the layer maintains a large ΔT across the system). We drop the prime notation from all the variables. Therefore, under the Boussinessq approximation, the three non-dimensional equations of conservation of mass, momentum and energy can be written as,

$$\left.\begin{aligned} &\nabla \cdot \vec{u} = 0 \\ &-\nabla p + \nabla \cdot \eta \dot{\bar{\bar{\varepsilon}}} = Ra\left(T - BC\right)\hat{z} \\ &\frac{DT}{Dt} = \frac{\partial T}{\partial t} + \left(\vec{u} \cdot \nabla\right)T = \nabla^2 T + H \end{aligned}\right\} \qquad 2.48$$

Numerical Method

For the geodynamical modeling in all our numerical experiments, we use the two-dimensional finite element mantle convection code Citcom [*Moresi and Solomatov*, 1995; *Moresi and Gurnis*, 1996]. Specifically, we use the thermochemical version of this code that has been modified for compositional rheology [*McNamara et al*., 2010; *Li et al*., 2014; *Allu Peddinti and McNamara*, 2015]. This finite element code solves the non-dimensional equations of 2.48. Since we study the ice-ocean system, we incorporate the water-ice Ih rheology in the code (adapted from the phase diagram in *Dunaeva et al*. (2010)) to determine the phase change with depth. In our numerical models, we use the ratio tracer method [e.g., *Tackley and King*, 2003] with compositional tracers for the species of ice and water.

We use a two dimensional, Cartesian geometry for the two-phase ice-ocean system. The initial conditions and the boundary conditions of the model are defined according to the dynamics of the problem being solved. The problem-specific numerical methods are described in the next three chapters to study the dynamics of the ice-shell in a two-phase ice-ocean system.

References

Allu Peddinti, D., & McNamara, A. K. (2015). Material transport across Europa's ice shell. *Geophys. Res. Lett.*, *42*, 4288-4293.

Dunaeva, A. N., Antsyshkin, D. V., & Kuskov, O. L. (2010). Phase diagram of H_2O: thermodynamic functions of the phase transitions of high-pressure ices. *Solar Sys. Res.*, *44*, 202-222.

Li, M., McNamara, A. K., & Garnero, E. J. (2014). Chemical complexity of hotspots caused by cyclic oceanic crust through mantle reservoirs. *Nature Geoscience*, *7*, 336-370.

McNamara, A. K., Garnero, E. J., & Rost, S. (2010). Tracking deep mantle reservoirs with ultra-low velocity zones. *Earth and Planetary Science Letters*, *299*(1-2), 1-9, doi:10.1016/j.epsl.2010.07.042.

Moresi, L., & Gurnis, M. (1996). Constraints on the lateral strength of slabs from three dimensional dynamic flow models. *Earth and Planetary Science Letters*, *138*(1-4), 15-28, doi:10.1016/0012-821x(95)00221-W.

Moresi, L. N., & Solomatov, V. S. (1995). Numerical Investigation of 2d Convection with Extremely Large Viscosity Variations. *Physics of Fluids*, *7*(9), 2154-2162, doi:10.1063/1.868465.

Schubert, G., Turcotte, D. L., & Olson, P. (2001). *Mantle Convection in the Earth and Planets*. Cambridge: Cambridge University Press.

Tackley, P. J., & King, S. D. (2003), Testing the tracer ratio method for modeling active compositional fields in mantle convection simulations. *Geochemistry Geophysics Geosystems*, *4*(4), 8302, doi:10.1029/2001gc000214.

CHAPTER 3

MATERIAL TRANSPORT ACROSS EUROPA'S ICY SHELL

The results of the study presented in this chapter have been published under the title "Material transport across Europa's ice shell" in Geophysical Research Letters, 2015. Citation: Allu Peddinti, D., and A. K. McNamara (2015), Material transport across Europa's ice shell, *Geophys. Res. Lett.*, 42, 4288-4293, doi:10.1002/2015GL063950.

3.1 Abstract

Jupiter's moon Europa exhibits a deformed icy surface with salt deposits concentrated along the varied geological features. The topographic alignment of salt deposits has been speculated to indicate an endogenic sourcing of the material. Two-way transport of salts from a liquid-water ocean beneath the ice shell to the surface, and vice versa, has been speculated. We present dynamical models that demonstrate the incorporation of newly frozen ice into convective plumes within the ice shell, caused by convection within the ice shell that drives dynamic topography along the ice-ocean boundary. The new ice that forms at the freezing front can be transported by the rising ice plumes toward the surface until it is blocked by a high-viscosity lid at the surface. Weakening of the lid by tidal or tectonic forces could then lead to the surface detection of ocean trace chemistry captured in the newly formed ice.

3.2 Introduction

The detection of putative oceanic material [*Zolotov and Kargel*, 2009] on the surface of Europa could have profound implications in evaluating its astrobiological potential [*Kargel et al*., 2000; *Greenberg et al*., 2000]. Surface detection of a potential biosignature from the deep ocean relies upon the material transport through the ice shell, and the

thickness of the ice shell [*Billings and Kattenhorn*, 2005] would determine the time scale and mechanism of this process. Previous studies [*McKinnon,* 1999; *Pappalardo et al*., 1998; *Barr and McKinnon*, 2007] identify that a thick ice shell is expected to undergo solid state convection. However, irrespective of thickness of the shell, two important aspects would govern the chemical transfer across the system. One is a mechanism to break through the viscous lid [*McKinnon,* 1999] of the ice shell in order to reach the surface. Second, for any oceanic material to reach the surface, it must first be transferred across the solid-liquid phase boundary between the ice shell and the ocean. The latter aspect is particularly important for a thick (>~20–30 km) convecting ice shell [*Pappalardo and Head*, 2001] which is the model we explore in this study. The phase boundary between solid ice (i.e., the ice shell) and liquid water (i.e., the subshell ocean) produces a high-viscosity contrast and marks a dynamical boundary. The low-viscosity water exhibits more vigorous convection than the solid state convection in ice. Thus, the high-viscosity contrast between the solid ice and liquid water effectively decouples the two layers and the resultant H_2O system consists of two convecting layers—a convecting ice shell over a convecting liquid ocean. In this study, we aim at exploring the convective material transport across this two-phase system.

In the H_2O system, increasing pressure decreases the melting temperature (figure 3.1). Hence, pressure-induced melting occurs at depth. In terrestrial glaciology, "ice-pump" mechanism is described [*Lewis and Perkin*, 1986; *Fricker et al*., 2001; *Robin et al*., 2014], where ice growth or accretion at the base of the ice shelves occurs by the supercooling of the water (produced by melting at depth) in the immediate vicinity of the ice surface [*Lewis and Perkin*, 1986; *Cook et al*., 2006]. It has also been suggested that

advective motion and ocean currents would augment the melting and deposition process at the base of the ice shelves. The rate of melting and deposition at the ice-water interface would be constant in a steady state ice pump. Previous studies [*Vance and Goodman*, 2009; *Soderlund et al*., 2014] have suggested that the ice-pump accretion mechanism could be operating in Europa's ice-ocean system. Hence, new ice could be forming at the base of the ice shell in Europa aided by topography generated by ocean currents at the ice-ocean interface. Although ice pump may be an important mechanism, in this study, we simply explore the process of formation and transport of the newly frozen ice from the ocean through the ice shell by convective ice plumes.

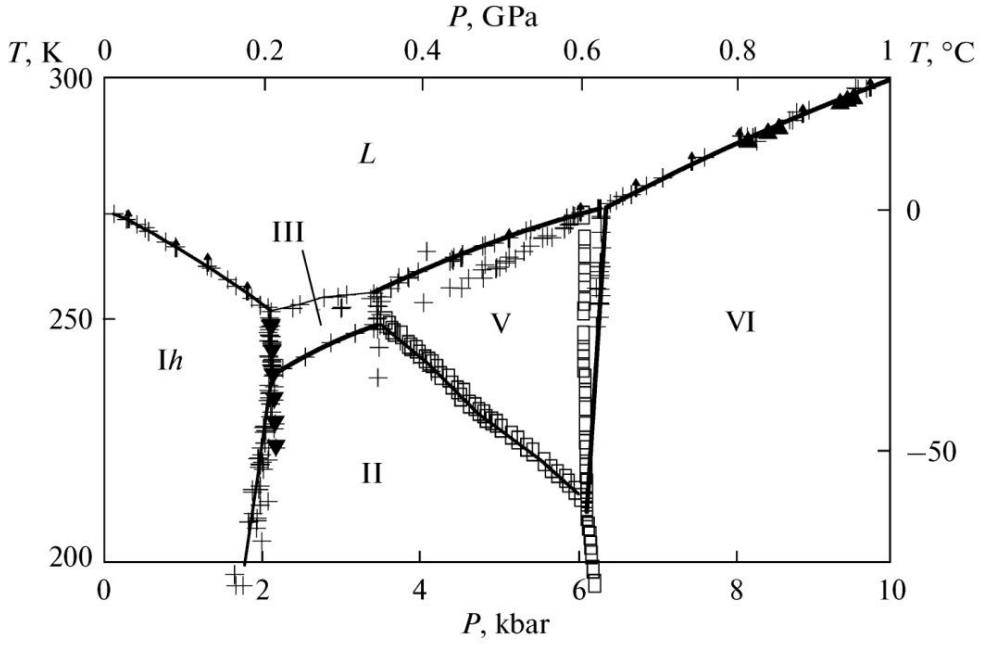

Figure 3.1. Phase Diagram of Water-Ice (From *Dunaeva et al*. (2010)). Shown here is a part of the phase diagram of water-ice. Ice can exist as several polycrystalline phases (I through XII) as a function of pressure and temperature. Terrestrial ice as well as ice on Europa, that is relevant to our current study, exists in the hexagonal I*h* phase. We thus use the left-part of the above phase diagram (Ice-liquid or I*h*-L interface) where the increase in pressure decreases the melting temperature.

3.3 Hypothesis

We hypothesize that ice is continually being created (by freezing) at the base of the ice shell, beneath upwelling regions within the ice. If so, trace amounts of aqueous compounds from the ocean could be captured by freezing in the newly formed ice at the phase boundary and then be incorporated into the warmer thermal plumes within the ice shell. The rising ice plumes could thus potentially lead to surface detection of the entrapped oceanic chemistry.

Figure 3.2 shows a conceptual sketch of this process within the two layered convecting system. The base of the ice shell is self-consistently defined by the freezing/melting pressure of H_2O. This freezing/melting pressure increases with decreasing temperature [e.g., *Dunaeva et al.*, 2010], so the base of the ice shell will be deeper beneath colder, downwelling ice and shallower beneath warmer, upwelling ice (as exaggeratedly shown by a thick bold line in Figure 3.2). This is determined by the equation [*Dunaeva et al*., 2010],

$$T(P) = a + bP + c\ln P + d/P + e\sqrt{P} \qquad 3.1$$

a = 273.0159; b = - 0.0132; c = - 0.1577; d = 0.0; and e = 0.1516

Where T is the temperature in Kelvin, P is the pressure in bar; and coefficients a, b, c, d, and e are obtained from experimental data.

Convection within the ice generates radial stresses on the top and bottom boundaries of the ice shell. At the top surface, which is a compositional boundary, these radial stresses drive the formation of dynamic topography [e.g., *Han and Showman*, 2005]. However, because the bottom of the ice shell is defined by a phase boundary (the freezing/melting pressure), the radial stresses act to drive the material across the freezing

pressure. Therefore, there is no actual dynamic topography generated. Upwellings within the ice shell generate radial stress that pulls the base of the ice shell upward to lower pressure. Any liquid water that fills that space will therefore cross into the solid phase due to decompression freezing. This new ice can then be incorporated into the warm rising plumes and be transported across the ice shell toward the surface. Conversely, downwellings within the ice shell generate radial stresses that push the base of the ice shell deeper to higher pressure. As this ice is exposed to higher pressure than the freezing/melting pressure, it will melt into the liquid ocean below.

When water from the ocean freezes to form new ice, some trace chemistry could be captured into it in the interstices of pure ice or as clathrates [*Zolotov and Kargel*, 2009]. This could result in transport of trace ocean chemistry into and across the ice shell as the rising plumes capture the newly formed ice and stir it into the convecting ice shell. Similarly, if surface chemistry gets incorporated into the convecting ice shell, some of it could ultimately enter the ocean across the phase boundary as ice melts beneath downwellings. Thus, chemical circulation from the surface to the ocean and back across the ice shell in between could be plausible in this two-phase convecting system.

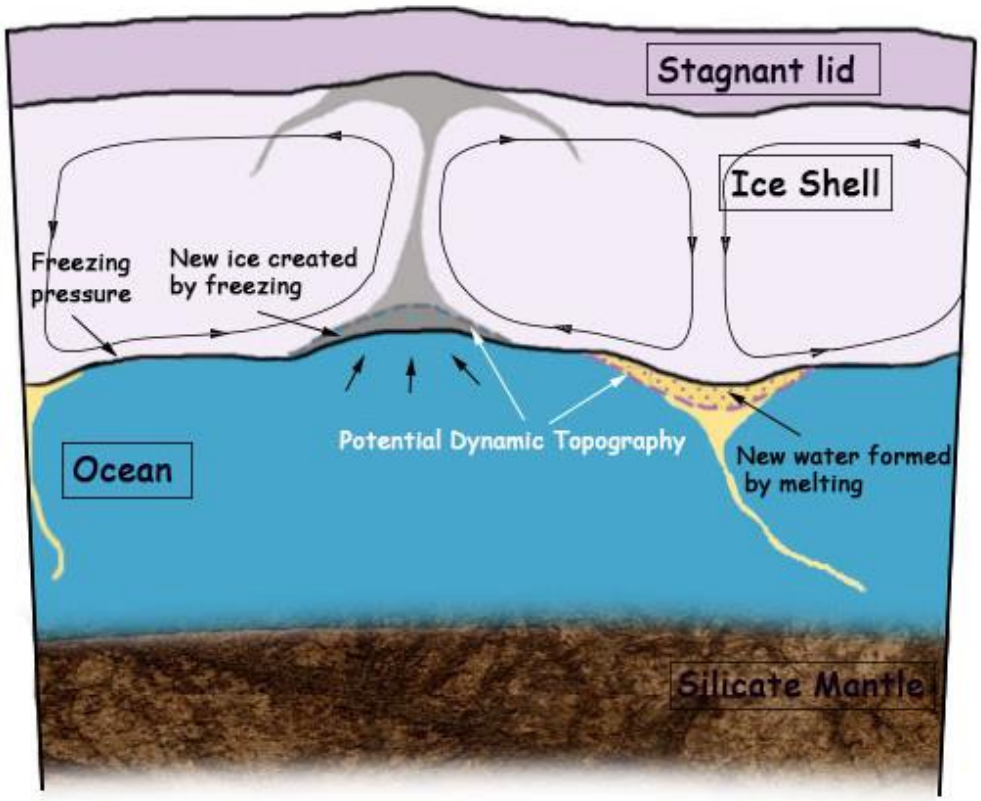

Figure 3.2. Hypothesis for formation and transport of new ice and new melt across the ice-ocean system. Sketch of upper few hundreds of km of Europa that shows the ice-ocean system (~100-150 km) with highly exaggerated phase boundary topography showing the convecting ice-shell (pale purple) over the convecting ocean (blue) separated by the phase change boundary (bold black line). The viscous, stagnant lid that forms atop the ice-shell is also shown (darker purple) and the entire ice-ocean system overlies the silicate mantle (brown shaded region) that extends downwards. Convection cells are represented by arrows. Relatively warmer plumes form within the convecting ice-shell, driving dynamic topography that would be developed if the ice/ocean boundary was a compositional boundary instead of a phase boundary. Ocean water fills this newly created void space (blue/grey stippled region), freezing to form new ice (grey) that is incorporated into the convecting ice-shell. Similarly new water forms by melting (purple-yellow dotted matrix) as the cold ice plumes push ice downwards and the cold water plumes (yellow) mix this newly melted water down into the convecting ocean. We hypothesize that if any trace chemistry from the ocean can be trapped into the newly frozen ice, it could be circulated across the system by means of the dynamic process schematically presented here. Furthermore, if chemistry from the surface gets incorporated into the convecting ice-shell, some of it should be expelled in the melt formed at the base of the downwellings into the ocean below.

3.4 Modeling

We test the hypothesis that convection induced dynamic topography on the bottom of the ice shell can drive the transfer of material across the phase boundary by performing numerical thermochemical convection calculations of the entire two-phase H_2O layer. We adapt our thermochemical version of the two-dimensional mantle convection code, Citcom [*Moresi and Gurnis*, 1996; *McNamara et al*., 2010], that solves the dimensionless equations for conservation of mass, momentum, and energy under the Boussinesq approximation.

$$\left.\begin{aligned} &\text{Conservation of mass: } \nabla \cdot \vec{u} = 0 \\ &\text{Conservation of momentum: } -\nabla P + \nabla \cdot \left(\eta \dot{\varepsilon}\right) = Ra\left(T - BC\right) \\ &\text{Conservation of energy: } \frac{\partial T}{\partial t} + \left(\vec{u} \cdot \nabla\right) T = \nabla^2 T \end{aligned}\right\} \quad 3.2$$

where $\vec{u}$ is velocity, P is the dynamic pressure, η is the dynamic viscosity, $\dot{\varepsilon}$ is the strain rate, T is the temperature, C is the composition and t is the time. The composition term C refers to the densities of the two phases in the system. In the ice-ocean system in our study, pure ice and pure water have same chemical composition. However, C identifies the density difference between the two phases of ice and water. This allows us to represent the two phases i.e. ice and water in the phase panel of our figures.

Ra and *B* are two non-dimensional parameters that control the vigor of convection and are defined as follows.

The thermal Rayleigh number, $Ra = \frac{\alpha \rho g \Delta T h^3}{\kappa \eta_m}$ 3.3

where α is the thermal expansivity, ρ is the density, κ is the thermal diffusivity, and η_m is the melting viscosity of ice; g is the acceleration due to gravity and h is the thickness of the system. ΔT is a constant related to temperature (which for convenience is usually identical to the temperature difference across the system). The values of all the fixed parameters used in the model are listed in Table 3.1. The system refers to the entire H_2O layer. The base of the system is the base of the ocean (the ocean-silicate interface) and the top of the system is the ice surface atop the ice-shell (the ice-vacuum interface). In this study, the thickness of the H_2O layer is fixed at 100 km.

The density of the system is represented by the buoyancy ratio given by B as,

$$B = \frac{\Delta\rho}{\rho\alpha\Delta T} \qquad 3.4$$

where $\Delta\rho$ is a constant representing the density contrast between liquid water and solid ice at $T \sim 273.15$ K and $P \sim 1$ bar, ρ and α are material properties of ice as listed in table 3.1 and ΔT is a constant related to temperature (consistent with the temperature difference between top and bottom of the system).

Table 3.1

Parameter Values Used in the Convection Models

Parameter	**Value**
Gravitational acceleration (g)	1.3 ms^{-2}
Temperature at the surface (T_s)	95 K
Melting temperature of ice (T_m)	Function of pressure (~273.15 K)
Melting viscosity of ice (η_m)	10^{16} Pa-s
Density of ice (ρ_i)	917 kgm^{-3}
Density of water (ρ_w)	1000 kgm^{-3}
Thermal expansivity of ice (α_i)	1.6 x 10^{-4} K^{-1}
Thermal expansivity of water (α_w)	2.0 x 10^{-5} K^{-1}
Thermal diffusivity of ice (κ_i)	1.0 x 10^{-6} m^2s^{-1}
Thermal diffusivity of water (κ_w)	1.33 x 10^{-7} m^2s^{-1}

Ice Viscosity

Europa's H_2O layer is relatively thin (~100-150 km) compared to the radius (~1561 km) of the moon and hence high pressure ices are not expected to exist in its interior. Therefore, Europa's ice-shell is made of the hexagonal ice phase, ice Ih which is the ice phase prevailing on Earth. This has allowed us to extrapolate the properties of ice on Earth (such as the elastic modulus) to higher pressures relevant to Europa. A temperature-dependent ice viscosity is used [e.g., *Showman and Han*, 2004; *Mitri and Showman*, 2005] in our calculations. Three cases that differ in their temperature dependence of ice viscosity are explored. All other parameters remain fixed (Table 3.1). The viscosity of the ice shell is determined by,

$$\eta = \eta_m \exp\left(A \left(\frac{T_m}{T} - 1 \right) \right) \tag{3.5}$$

Where η (Pa s) is the viscosity, η_m (Pa s) is the melting viscosity fixed here at 10^{16} Pa s, A is the activation coefficient, T_m (K) is the melting temperature, and T (K) is the temperature. A controls the temperature dependence of ice viscosity. We vary the values of A in our study.

$$A = \ln\left(\frac{\eta_{\max}}{\eta_{\min}} \right) \tag{3.6}$$

Where η_{max} and η_{min} are the maximum and minimum values of ice-viscosity respectively.

We employ a modest temperature dependence and a high melting viscosity in our models in order to improve the computational efficiency of the models. The melting viscosity of ice for the cases presented in this study is slightly higher than the values generally adopted for Europa's ice-shell. For instance, the Showman and Han (2004)

study explores a range of values from 10^{12} Pa s to 10^{14} Pa s. Because our study employs a low-viscosity proxy fluid to represent the liquid water phase that is 1000x less viscous than the least-viscous ice, it becomes computationally prohibitive to reach these values while still maintaining adequate grid resolution. Therefore, we must use somewhat higher values for ice viscosity. For the same reason, the values of *A* explored for this study are less than the value used by Showman and Han (2004) study which is based on the Goldsby and Kohlstedt study (*J. Geophys. Res*., 106, 2001).

Proxy Fluid Approximation for the Ocean

To establish a self-consistent two-phase system, the phase diagram of water ice Ih [*Dunaeva et al*., 2010] was incorporated into the model to produce a temperature- and pressure-dependent phase change. The extreme viscosity contrast between ice and water is computationally challenging to model; however, for this problem it is only necessary to resolve the convection within the ice shell and adequately reproduce the viscous decoupling between ice and liquid ocean. Hence, our numerical model employs a low-viscosity proxy fluid to represent the ocean layer. Although the viscosity of this proxy fluid is higher than that of liquid water, it remains much lower than that of solid ice and allows a viscously decoupled, self-consistent phase boundary. Such a low-viscosity approximation has also been used in terrestrial mantle convection studies to represent a realistic scenario of free surface plates over the mantle [*Crameri et al*., 2012]. By performing an extensive set of initial comparison calculations (examining different viscosities of the proxy fluid), we found that proxy fluid viscosity that is a thousand times lower than that of the lowest viscosity in the ice was sufficient to provide adequate viscous decoupling of the layers and further reduction in viscosity did not produce a

noticeable change in dynamics of the ice portion of the system (details in the Appendix A).

Initial Condition

In order to design a simple experiment to test this hypothesis, we do not yet include the effects of tidal heating [*Tobie et al*., 2003; *Han and Showman*, 2010] which is considered to be an important source of heat generation in Europa. Therefore, the heat balance of our model is controlled by the prescribed temperature contrast across the system (from the bottom of the ocean to the surface) which we control in order to reach a steady-state ice-shell thickness over time.

All the calculations begin from an initial stable, convecting two-phase system. The initial condition is achieved by allowing a fluid layer of thickness h to self-consistently form a two- phase convecting system as it cools from the top and is heated from below. In order to achieve a convecting ice-shell over a convecting ocean layer and to maintain the stability of such a system, we adjust the value of the numerical parameter ΔT. ΔT is consistent with the temperature difference between the base and the top of the system. However, in the context of this study ΔT is merely a numerical parameter that is varied in order to attain a stable, two-phase convecting system and does not have any physical significance. We staged our system to be at thermal equilibrium, such that the average ice-shell thickness neither grows nor shrinks.

3.5 Results and Discussion

Case 1 employs a relatively moderate temperature-dependence of viscosity (A=5.0, leading to a viscosity contrast of ~ 100x across the ice-shell). A time sequence of three snapshots for this case is shown in Figure 3.3. For each snapshot, phase composition and

temperature are shown in the left and right panels, respectively. The temperature panels for each of these times reveal vigorous convection occurring within the ice-shell, with warm upwelling plumes surrounded by cooler downwellings. In the phase panels, blue represents the proxy fluid (liquid ocean) and black represents the solid ice. As new ice is formed by freezing of water crossing the phase boundary, we track it by changing the color of the element that contains it. In other words, elements that contain newly-formed ice are colored white-green, the shade of which is determined by the fraction of new ice that the element contains. The snapshots clearly show that the newly-formed ice is then advected up along the plume axis until the plume is deflected by the viscous lid at the surface. The newly formed ice is subsequently stirred into the convecting ice-shell beneath the viscous lid.

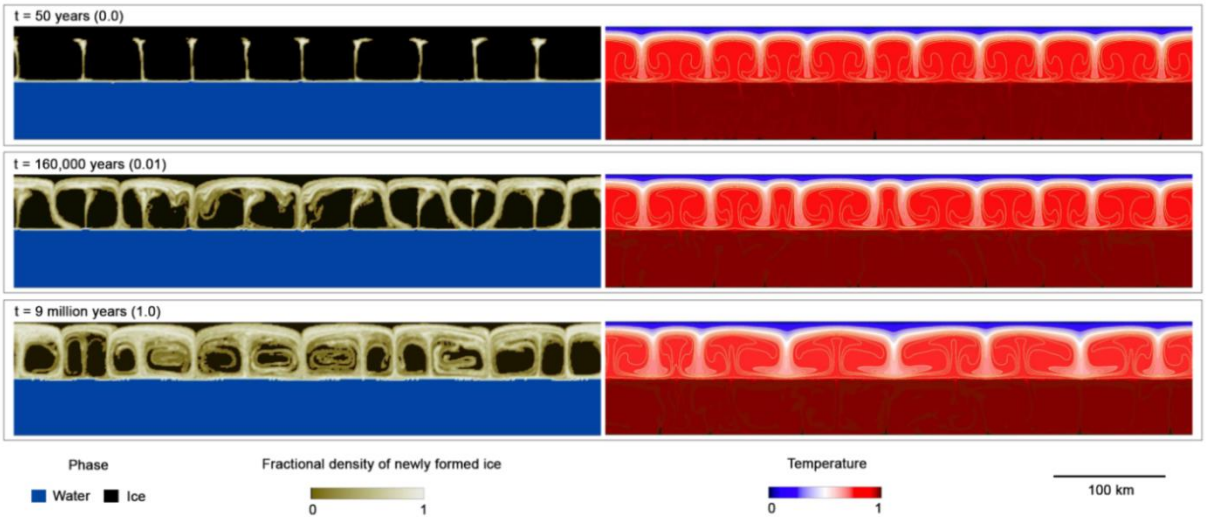

Figure 3.3. Time evolution of Case 1. The composition (phase) and temperature fields are shown for three time-snapshots in the calculation, each as an individual row. Panels on the left display composition, and panels on the right display temperature. In the composition panels, blue represents the proxy fluid (the liquid ocean) and black represents solid ice. The fractional density of newly-formed ice is superimposed on the black background (as green to white). The three rows are identified by the dimensional times and the non-dimensional times within parentheses relative to the first step shown in the first row at time, t = 0.0 when we start tracking the new ice in a convectively equilibrated system.

Cases 2 and 3 employ higher temperature-dependence of viscosity, leading to viscosity contrasts of 10,000x and 1,000,000x across the ice-shell, respectively. Snapshots from these cases are shown in figure 3.4 which includes panels showing the logarithm of viscosity, phase composition, and temperature. We find that the main effect of increasing the temperature-dependence of viscosity is to thicken the viscous lid at the top of the ice-shell. Like in case 1, new ice is formed at the base of upwelling ice plumes, advected up along the plume axis, deflected by the viscous lid, and stirred into the convecting ice-shell.

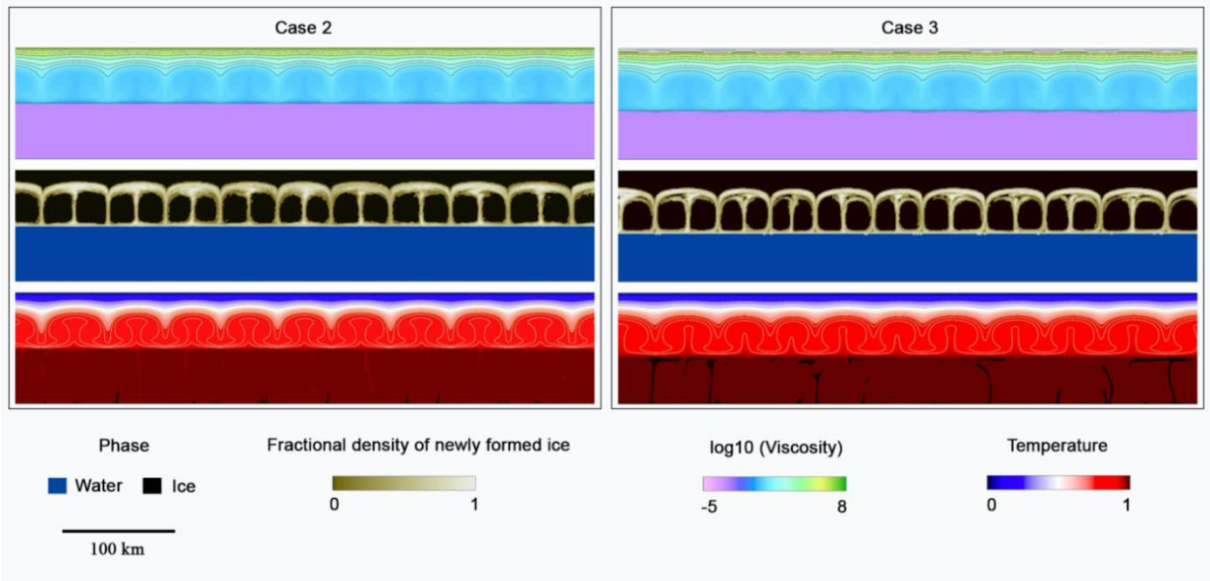

Figure 3.4. Demonstration of new ice formation for Cases 2 and 3. Top panels display the logarithm of viscosity, with contours shown for every order of magnitude increase. Middle panels display composition (phase), in which blue represents the proxy fluid (liquid ocean) and black represents solid ice. The fractional density of newly-formed ice is superposed on the black background (as green to white). Bottom panels represent temperature. The two cases shown here have higher temperature-dependence of ice viscosity across the shell than case 1 with case 2 representing a viscosity contrast of 10,000x (A=10.0) and case 3 representing a viscosity contrast of 1,000,000x (A=13.8) across the ice-shell respectively. The snapshots in cases 2 and 3 are taken at approximately 5 million years and 13 million years respectively.

While the effects of internal heating, melting viscosity of ice and numerical parameters such as grid resolution would affect the absolute amount of new ice that is formed, the physics of new ice formation at the phase boundary between the ice-shell and the ocean established here is likely to be a dynamic process occurring in convecting ice shells over liquid water oceans, including the ice-ocean system of Europa. However, it has been recognized that numerical representation of entrainment is a function of grid resolution [*Van Keken et al*., 1997] and hence finer the grid, more accurate the estimate of the amount of new ice formed and incorporated. Therefore, the amount of new ice formed and transported demonstrated in this study should be treated as an upper limit of possible new ice formation. Our experiment is focused towards understanding material transport due to radial stresses from ice-shell convection pushing/pulling the material across the phase boundary. However, other mechanisms such as "ice-pump" [*Lewis and Perkin*, 1986; *Fricker et al*., 2001, *Robin et al*., 2014] may provide additional material transport across the phase boundary.

Our Boussinesq formulation in this study does not include latent heat, adiabatic effects, viscous dissipation and tidal heating. Latent heat released upon freezing could decrease the rate of new ice formed, and therefore our calculations would provide an upper bound. Addition of compositional species (e.g., salts) may influence the freezing and melting of ice and change the estimates of new ice formed. In any case, our simple numerical experiments demonstrate the process of dynamic stress driving material across the phase boundary, which is expected to also occur in models with more complexities added.

The possibility of trace chemistry from the ocean being trapped into the freezing newly-formed ice and its subsequent integration into rising ice plumes argues for its detection at the surface subject to breaking of the viscous ice lid capping the shell. It has been proposed that weakening of the lid can occur due to the tidal forces as well as convective stresses [*Sotin et al*., 2002; *Pappalardo and Barr*, 2004; *Schmidt et al*., 2011] and tectonic stresses [*Sullivan et al*., 1998; *Greenberg et al*., 1998; *Hoppa et al*., 1999; *Prockter and Pappalardo*, 2000; *Nimmo and Gaidos*, 2002]. A recent study [*Kattenhorn and Prockter*, 2014] has also proposed the possible tectonic "subsumption" in the ice-shell which would further facilitate transport of the newly formed ice that is advected by ice plumes towards the surface. Fracturing the lid could thus expose the rising new ice to the surface and potentially allow any captured oceanic material to be detected on the surface.

Our qualitative calculations support the convective-driven process of new ice formation in the two phase convecting ice-ocean system as relevant to Europa. They also demonstrate that this new ice (from the ocean) can be integrated into the rising ice plumes, move toward the surface, and become progressively mixed into the convecting ice-shell. However, the newly-formed ice cannot penetrate the viscous lid of the ice-shell; therefore, some mechanism is required to break the lid to expose it at the surface. Possible implications of these conclusions include transport of trace ocean chemistry on to the surface and from the surface down into the ocean below – an essential while not necessary factor for any potential existence of life in the icy moon.

Appendix: Tracking new ice formation

The phase – ice or water is dynamically assigned to the tracer according to the pressure dependence of temperature described by equation 3.1. In a cooling two-phase system, the thickness of the ice and fluid layers changes continuously until a thermal equilibrium is reached. Therefore the visible change in shell thickness is likely due to bulk fluid freezing or bulk ice melting at the phase-change interface. However, when the system is at equilibrium and the thickness of the shell remains constant, the formation of ice and the formation of melt at the phase boundary offset each other. Since the aim of the numerical experiments in this study is to investigate the formation and transport of new ice into the plumes at the interface, we initiate tracking of new ice only after the ice-shell thickness reaches equilibrium. We change the color of the new ice in the shell as it forms by freezing. Tracers are used to represent the phase field – solid ice or fluid. The fractional density of new ice tracers in each element of the grid is mapped across the phase panel in the models. The fractional density is defined as the ratio of number of new ice tracers to the total number of tracers in that element.

$$Fractional\ density_{element} = \left. \frac{no.of\ tracers_{new-ice}}{no.of\ tracers_{total}} \right|_{element}$$

When new ice formed at the phase change interface is captured into the ice plumes and transported across the ice-shell, the color of the elements containing new ice is changed according to the fractional density value of each element. This allows us to track the movement of new ice across the ice-shell.

References

Barr, A. C., & McKinnon, W. B. (2007). Convection in ice I shells and mantles with self-consistent grain size. *J. Geophys. Res.*, *112*, E02012, doi:10.1029/2006JE002781.

Billings, S. E., & Kattenhorn, S. A. (2005). The great thickness debate: Ice shell thickness models for Europa and comparisons with estimates based on flexure at ridges. *Icarus, 177*, 397–412.

Cook, S. J., Waller, R. I., & Knight, P. G. (2006). Glaciohydraulic supercooling: The process and its significance. *Prog. Phys. Geogr*., *30*(5), 577–588.

Crameri, F., Tackley, P. J., Meilick, I., Gerya, T. V., & Kaus, B. J. P. (2012). A free plate surface and weak oceanic crust produce single-sided subduction on Earth. *Geophys. Res. Lett., 39*, L03306, doi:10.1029/2011GL050046.

Dunaeva, A. N., Antsyshkin, D. V., & Kuskov, O. L. (2010). Phase diagram of H_2O: Thermodynamic functions of the phase transitions of high-pressure ices. *Solar Sys. Res*., *44*, 202–222.

Fricker, H. A., Popov, S., Allison, I., & Young, N. (2001). Distribution of marine ice beneath the Amery ice shelf. *Geophys. Res. Lett., 28*, 2241–2244, doi:10.1029/2000GL012461.

Greenberg, R., et al. (1998). Tectonic processes on Europa: Tidal stresses, mechanical response, and visible features. *Icarus, 135*, 64–78.

Greenberg, R., Geissler, P., Tufts, B. R., & Hoppa G. V. (2000). Habitability of Europa's crust: The role of tidal-tectonic processes. *J. Geophys. Res., 105*, 17,551–17,562, doi:10.1029/1999JE001147.

Han, L., & Showman, A. P. (2005). Thermo-compositional convection in Europa's ice shell with salinity. *Geophys. Res. Lett., 32*, L20201, doi:10.1029/2005GL023979.

Han, L., & Showman, A. P. (2010). Coupled convection and tidal dissipation in Europa's ice shell. *Icarus, 207*, 834–844.

Hoppa, G. V., Tufts, B. R., Greenberg, R., & Geissler, P. E. (1999). Formation of cycloidal features on Europa. *Science, 285*, 1899–1902.

Kargel, J. S., Kaye, J. Z., Head, J. W., Marion, G. M., Sassen, R., Crowley, J. K., Ballesteros, O.P., Grant, S. A., & Hogenboom, D. L. (2000). Europa's crust and ocean: Origin, composition, and the prospects for life. *Icarus, 148*, 226–265.

Kattenhorn, S. A., & Prockter, L. M. (2014). Evidence for subduction in the ice shell of Europa. *Nature Geoscience, 7*, 762–767.

Lewis, E. L., & Perkin, R. G. (1986). Ice pumps and their rates. *J. Geophys. Res., 91*, 11,756–11,762, doi:10.1029/JC091iC10p11756.

McKinnon, W. B. (1999). Convective instability in Europa's floating ice shell. *Geophys. Res. Lett., 7*, 951–954, doi:10.1029/1999GL900125.

McNamara, A. K., Garnero, E. J., & Rost, S. (2010). Tracking deep mantle reservoirs with ultra-low velocity zones. *Earth Planet. Sci. Lett., 299*, 1–9.

Mitri, G., & Showman, A. P. (2005). Convective-conductive transitions and sensitivity of a convecting ice shell to perturbations in heat flux and tidal-heating rate: Implications for Europa. *Icarus, 177*, 447–460.

Moresi, L., & Gurnis, M. (1996). Constraints on the lateral strength of slabs from three-dimensional dynamic flow models. *Earth Planet. Sci. Lett., 138*, 15–28.

Nimmo, F., & Gaidos, E. (2002). Strike-slip motion and double ridge formation on Europa. *J. Geophys. Res., 107*(E4), 5021, doi:10.1029/2000JE001476.

Pappalardo, R. T., & Barr, A. C. (2004). The origin of domes on Europa: The role of thermally induced compositional diapirism. *Geophys. Res. Lett., 31*, L01701, doi:10.1029/2003GL019202.

Pappalardo, R. T., & Head, J. W. (2001). The thick-shell model of Europa's geology: Implications for crustal processes. *Lunar Planet. Sci. Conf. 32*, 1866.

Pappalardo, R. T., et al. (1998). Geological evidence for solid-state convection in Europa's ice shell. *Nature, 391*, 365–368.

Prockter, L. M., & Pappalardo, R. T. (2000). Folds on Europa: Implications for crustal cycling and accommodation of extension. *Science, 289*, 941–943.

Robin, E. B., Tinto, K., Das, I., Wolovick, M., Chu, W., Creyts, T. T., Frearson, N., Abdi, A., & Paden, J. D. (2014). Deformation, warming and softening of Greenland's ice by refreezing meltwater. *Nature Geoscience, 7*, 497–502.

Schmidt, B. E., Blankenship, D. D., Patterson, G. W., & Schenk, P. M. (2011). Active formation of "chaos terrain" over shallow subsurface water on Europa. *Nature, 479*, 502–505.

Showman, A. P., & Han, L. (2004). Numerical simulations of convection in Europa's ice shell: Implications for surface features. *J. Geophys. Res., 109*, E01010, doi:10.1029/2003JE002103.

Soderlund, K. M., Schmidt, B. E., Wict, J., & Blankenship, D. D. (2014). Ocean dynamics of Europa: Implications for chaos distribution and ice-ocean coupling. *Nature Geoscience, 7*, 16–19.

Sotin, C., Head III, J. W., & Tobie, G. (2002). Europa: Tidal heating of upwelling thermal plumes and the origin of lenticulae and chaos melting. *Geophys. Res. Lett., 29*(23), 2109, doi:10.1029/2001GL013884.

Sullivan, R., et al. (1998). Episodic plate separation and fracture infill on the surface of Europa. *Nature, 391*, 371–373.

Tobie, G., Choblet, G., & Sotin, C. (2003). Tidally heated convection: Constraints on Europa's ice shell thickness. *J. Geophys. Res., 108*(E11), 5124, doi:10.1029/2003JE002099.

Van Keken, P. E., King, S. D., Schmeling, H., Christensen, U. R., Neumister, D., & Doin, M.-P. (1997). A comparison of methods for the modeling of thermochemical convection. *J. Geophys. Res., 102*, 22,477–22,495, doi:10.1029/97JB01353.

Vance, S., & Goodman, J. C. (2009). Oceanography of an ice-covered moon. *Europa*, edited by R. T. Pappalardo,W. B.McKinnon, and K. K. Khurana, pp. 459–482, Tucson: University of Arizona Press.

Warren, S. G., Brandt, R. E., Grenfell, T. C., & McKay, C. P. (2002). Snowball Earth: Ice thickness on the tropical ocean. *J. Geophys. Res., 107*(C10), 3167, doi:10.1029/2001JC001123.

Zolotov, M. Y., & Kargel, J. S. (2009). On the chemical composition of Europa's icy shell, ocean, and underlying rocks. *Europa*, edited by R. T. Pappalardo, W. B. McKinnon, and K. K. Khurana, pp. 431–451, Tucson: University of Arizona Press.

CHAPTER 4

EVOLUTION OF ICE-SHELL THICKNESS IN AN ICE-OCEAN SYSTEM: EFFECT OF TIDAL HEATING ON SHELL THICKNESS AND GROWTH RATE

4.1 Abstract

Current astrobiological exploration of the outer solar system is largely driven by understanding planetary ice-ocean systems such as those of Europa and Enceladus. The ice-shell thickness that affects the dynamics of the ice-ocean system is determined by the balance between heat loss via convection and conduction, and the heat production via tidal dissipation and radiogenic decay. In this study, we investigate how ice-shells of such ocean moons grow, and how convection inside them evolves as the system cools. We perform geodynamical calculations to investigate the ice-shell thickness and growth rate as the system cools from a warm initial condition. We study both diffuse and localized end member modes of tidal internal heating within the ice-shell. We find that as the ice-shell cools and thickens, there is a reconfiguration of the convection patterns, increasing the size of convection cells that leads to a relatively significant increase in the ice-shell growth rate. Addition of sufficient heat also allows the ice-shell to attain an equilibrium thickness.

4.2 Introduction

Jupiter's icy moon Europa is one of the closest astrobiological targets that harbors a putative subsurface ocean underneath an ice-shell. The thickness of this ice-shell governs the dynamics, hence both material and heat transfer, of the ice-ocean system. Flexing induced by Jupiter's gravity field results in tidal dissipation within the ice and is expected to affect the ice-shell thickness [*Hussmann et al.,* 2002; *Sotin et al.,* 2004] with

implications for surface geology [*Sullivan et al.*, 1998; *Greenberg et al.*, 1998; *Nimmo and Gaidos*, 2002]. Because the tidal dissipation is a function of viscosity of ice, which in turn is temperature-dependent [*Sotin et al.*, 2002; *Han and Showman*, 2004; *Sotin et al.*, 2009; *Nimmo and Manga*, 2009], it is expected to be maximum within the ice-shell interior [*Ojakangas and Stevenson*, 1989; *McKinnon*, 1999; *Mitri and Showman*, 2005]. Upon thickening and cooling (which increases viscosity), tidal dissipation increases. This in turn increases temperature, resulting in a decrease in the ice-shell thickness and viscosity. The resultant decrease in viscosity reduces the tidal dissipation. Thus, tidal dissipation combined with self-consistent ice-shell growth, is expected to produce a stabilizing feedback.

A previous numerical study [*Mitri and Showman*, 2005] that investigated the effect of perturbations in heat flux and tidal heating on ice-shell thickness predicted transition between two end-member equilibrium states – a thin, conductive shell and a thick, convective shell for a given heat flux. In their simulations, they found that the heat flux undergoes a finite-amplitude jump at the critical Rayleigh number [*Stengel et al.*, 1982]. However, their simulations modeled a fixed ice-shell thickness, where the equilibrium heat flux and tidal flexing amplitude from the constant-thickness simulations were used to infer the changes in ice-shell thickness. Thus, these models did not note the dynamic ice-shell growth.

In this study, we examine the growth of a thickening ice-shell upon cooling. In particular, we examine how growth rate of the ice-shell depends upon the changing convective planform within the ice. We examine two end-member scenarios of tidal dissipation: (1) a diffuse dissipation in which the heating rate is constant and ubiquitous

throughout the ice-shell, and, (2) a localized dissipation that depends on viscosity and is at a maximum beneath the near-surface, high-viscosity lid of the ice-shell. Our models consist of an ice-shell self-consistently forming from a cooling ocean allowing us to directly study its growth over time.

4.3 Background

Surface and Structure

Europa, one of the four Galilean moons of Jupiter, is roughly 1561 km in radius and is differentiated [*Anderson et al.,* 1998] into a metallic core overlain by a silicate mantle bound by an ocean with an icy surface. The average surface temperature of the moon is ~ 95 K. Gravity measurements [*Anderson et al.,* 1998] estimated ~ 80-170 km thick global H_2O layer and the detection of an induced magnetic field [*Kivelson et al.,* 1997, *Khurana et al.,* 1998] by Galileo spacecraft along with examination of surface geology [*Pappalardo et al.,* 1999] had provided evidence for a global subsurface ocean within it. However, this data does not constrain the individual thicknesses of the solid ice and the liquid ocean layers. Europa also possesses a geologically young surface (<100 Myr) [*Carr et al.,* 1998; *Zahnle et al.,* 2003] peppered with various geological features including ridges, pits, domes, sparse craters [*Pappalardo et al.,* 1998], bands [*Sullivan et al.,* 1998] and chaotic terrains [*Carr et al.,* 1998] that are comprised of blocks of ridged material displaced in a hummocky matrix. This young surface has been interpreted to indicate resurfacing of the ice-crust and hence geologically recent activity within the H_2O layer. Additionally, spacecraft images and spectral measurements note the presence of colored non-ice material [*McCord et al.,* 1998; *Zolotov and Kargel,* 2009] concentrated along the morphological features. The presence of a subsurface ocean along with the

observed surface topography and the topographically aligned surface chemistry indicates current/recent geological activity. The thickness of the ice-shell and its interaction with the ocean beneath determines the material transport between the rocky interior and the surface and the detection of its potential surface signature by future space missions.

Tidal Heating

In order for a planetary body with low surface temperature and little radiogenic heating to retain a present-day liquid ocean without freezing over, it either has to consist of dissolved antifreeze compounds such as ammonia [*Deschamps and Sotin*, 2001; *Spohn and Schubert*, 2003; *Ruiz and Fairen*, 2005], or a significant internal heat source such as tidal dissipation is required [*Cassen et al.*, 1979; *McKinnon*, 1999]. The two main sources of heat in Europa are radioactive decay in its rocky interior and the tidal dissipation due to its eccentric orbit around Jupiter [*Hussmann and Spohn*, 2004; *Sotin et al.*, 2009; *Nimmo and Manga*, 2009]. While radiogenic heating due to decay of isotopes of U, Th and K may be significant in the silicate mantle, tidal dissipation is expected to be the more dominant heat source in the icy portion of the system [*Nimmo and Manga*, 2009]. Europa revolves around Jupiter with a period of 3.55 days (equal to its rotation period) in an orbit with eccentricity ~ 0.01 which leads to a diurnal variation in tidal stresses [*Nimmo and Manga*, 2009]. This diurnal component adds significantly to the tidal internal heating within the icy interior [*Sotin et al.*, 2009]. Additionally, the 1:2:4 Laplace resonance of Io, Europa and Ganymede contributes to gravity perturbations and hence enhances the tidal forcing on Europa [*Cassen et al.*, 1979; *Greenberg and Geissler*, 2002].

Approximating ice as a Maxwell solid provides a simple description of viscoelastic response of ice on Europa (whose forcing period is close to Maxwell time). For a Maxwell solid, the perturbation [*Sotin et al.*, 2002] of the elastic shear modulus (μ) is given by,

$$\delta\mu = \frac{\eta\omega\mu^2}{\mu^2 + \omega^2\eta^2} = \frac{\eta\omega}{\left(1 + \frac{\omega^2\eta^2}{\mu^2}\right)} \qquad 4.1$$

Where η is the viscosity and ω is the circular frequency of straining. This first order perturbation of the elastic response to tidal potential can be used to calculate the volumetric tidal dissipation rate [*Takeushi and Saito*, 1972; *Sotin et al.*, 2002]. Thus, the tidal dissipation generated due to the viscoelastic behavior of ice may be expressed by the following equation [*Showman and Han*, 2004],

$$q = \frac{{\varepsilon_0}^2\omega^2\eta}{2\left(1 + \frac{\omega^2\eta^2}{\mu^2}\right)}\ Wm^{-3} \qquad 4.2$$

$$\varepsilon_0 = 10^{-4} - 10^{-6};\ \omega = 2\times10^{-5}\,s^{-1};\ \mu = 4\times10^{9}\,Pa$$

where q is the tidal dissipation, ε_0 is the maximum strain rate, ω is the tidal flexing frequency, μ is the rigidity of ice and η is the viscosity of ice (which is a function of temperature and to a smaller degree, pressure). At melting temperatures, the viscosity of ice ranges between 10^{13} – 10^{15} Pas. Despite not accounting for different tidal flexing frequencies and temperatures, this model can be used to provide a good first-order approximation of tidal dissipation in the ice-shell of Europa [*Sotin et al.*, 2009]. Advanced methods have been developed to calculate the radial and lateral distribution of

tidal dissipation in the ice layer [e.g., *Tobie et al.*, 2005] and it may be interesting to incorporate this variable dissipation in the models to determine its effect on ice formation in a future study.

Ice Shell Thickness

The ice-shell thickness of Europa remains uncertain; however several methods have been used to estimate it. A number of thickness estimates are based on the observed surface topography such as craters, ridges and domes. Some features (such as ridges) are hypothesized to be formed via direct cracking of a thin ice-shell by tectonic or tidal stresses [*Greenberg et al.,* 1998]. The observed topography and isostasy methods are used to calculate the shell thickness in these hypotheses. These estimates are usually a measure of the elastic thickness of the ice-shell and do not predict the thickness of its ductile portion, and hence can be treated as a lower bound for the overall shell thickness [*Nimmo et al.*, 2003; *Billings and Kattenhorn*, 2005]. Other geological features (such as pits and domes) are hypothesized to be surface expressions of convective diapirs [*Rathbun et al.*, 1998; *Sotin et al.,* 2002] in thick ice-shells. Numerical models and theoretical calculations of convection induced dynamic topography are used to calculate the thickness of the ice-shell in this hypothesis.

Based on these several methods, the estimates of ice-shell thickness on Europa vary from very thin (1-2 km) [e.g. *Carr et al.,* 1998; *Greeley et al.,* 1998; *Hoppa et al.*, 1999a; *Greenberg et al*., 2000] upto ~ 50 km [e.g. *Pappalardo et al.,* 1998; *Rathbun et al.,* 1998; *Schenk*, 2002; *Hussmann et al.,* 2002; *Nimmo et al.,* 2003]. Flexure and other mechanical analyses based on surface topography place estimates of the elastic thickness of the ice-shell at ≤ ~ 1-5 km [e.g. *Nimmo et al.*, 2003; *Billings and Kattenhorn*, 2005].

Impact crater studies have estimated thicknesses from 3-4 km [*Turtle and Pierazzo*, 2001] to 19 km [*Schenk*, 2002]. These estimates correspond to the time of formation of the specific surface features and hence do not necessarily indicate the present shell thickness.

Ice-shell thickness is not only useful in understanding the formation of observed surface geology but also for predicting the transport, and detection of oceanic material on the surface [*Nimmo et al.,* 2005]. For example, geologic features such as chaos, lenticulae, ridges and bands are indications of surface disruption and are often associated with melt-through processes [*Greenberg et al.,* 1998]. For melt-through to occur, the ice-shell would have to be thin (~ few km). This thin shell that is in contact with the ocean is surmised to crack due to tidal or tectonic stresses leading to melting onto the surface [*Greenberg et al.*, 1998; *O'Brien et al.*, 2002]. This melt-through mechanism would thus allow direct transport of oceanic material onto the surface, supporting the endogenic origin of the surface composition observed. On the other hand, thick ice-shells show that partial melting and disruption could result from rising convective ice diapirs as well [*Pappalardo et al.*, 1998; *Sotin et al.*, 2002], allowing oceanic material to reach the surface. Our previous geodynamical study [*Allu Peddinti and McNamara*, 2015] also demonstrated that trace oceanic material could be transported across the shell via convective ice plumes.

Shell thickness is also estimated from the calculated heat loss from the surface of the moon (using values of heat from initial accretion, impact cratering as well as tidal dissipation). Heat flow has also been estimated from the thermal IR data obtained by the Galileo spacecraft [*Spencer et al.*, 1999]. Convection is expected to be the dominant

mode of heat transfer across a thicker ice-shell [*Cassen et al.*, 1979; *McKinnon*, 1999; *Showman and Han*, 2004; *Mitri and Showman*, 2005] while a thin ice layer would primarily lose heat by conduction [*Greenberg et al.*, 1998]. Hence, depending on the ice-shell thickness, different modes of heat and mass transfer are postulated to operate across the ice-ocean system of the moon. Estimating the present shell thickness and its evolution over the past ~100 Myr can thus inform future missions about the most optimal sites where a surface signature of oceanic chemistry might be detected.

4.4 Approach

Numerical models can be used to study how different factors such as the addition of tidal heating, impurities, grain-size dependent ice-viscosity, etc. affect the convective dynamics of the ice-ocean system over time. Previous geodynamic modeling studies that have considered the effects of these factors typically employ a constant ice-shell thickness. For example, Showman and Han (2004) and Mitri and Showman (2005) have investigated the effects of tidal dissipation in a convecting ice-shell of fixed thickness. Showman and Han (2004) performed 2-d numerical simulations of ice-convection to explain surface feature formation in the presence and absence of tidal heating. Mitri and Showman (2005) inferred ice-shell thickness variations for perturbations in shell heat flux. The grain-size dependency of viscosity which affects the amount of tidal heat generated in an ice-shell has also been studied [*Barr and Pappalardo*, 2005; *Barr and McKinnon*, 2007; *Han and Showman*, 2011]. The earlier studies provide a general understanding of ice-shell convection; however some questions necessitate employing an ice-shell with dynamic, self-consistent thickness. The question we address here is does the growth rate of the ice-shell change as the ice-shell thickens upon cooling. If so, is the

change in growth rate caused by changing convection patterns (e.g., changes in convection cell width)? Furthermore, how sensitive is the growth rate to the mode of internal heating (uniform versus localized)? In this study, we model a two-phase ice-ocean system that allows the ice-shell thickness to change over time, consistent with the water-ice phase diagram. We monitor the change in the ice-shell thickness and its growth rate as it forms in the presence of localized tidal internal heating in the ice. For reference, we first examine an end-member control case of an ice-ocean system without any heating. We then model another end-member case where a uniform tidal internal heating is applied in the ice-shell. Next, we examine the case with localization of the viscosity-dependent tidal internal heating in the ice for its effects on temporal variation of ice-shell thickness.

4.5 Numerical Modeling

Model Setup

The model consists of a 100 km thick, initially warm H_2O layer (non-dimensional temperature, T = 1.0) that is allowed to self-consistently freeze as it cools from the top. We use the two-dimensional mantle convection code, Citcom [*Moresi and Gurnis*, 1996], modified for thermochemical convection and compositional rheology [*McNamara et al.*, 2010; *Li and McNamara*, 2013; *Li et al*., 2014; *Allu Peddinti and McNamara*, 2015] that solves the non-dimensional equations for conservation of mass, momentum and energy under the Boussinesq approximation.

$$\left.\begin{aligned} &\nabla \cdot \vec{u} = 0 \\ &-\nabla P + \nabla \cdot \left(\eta \dot{\varepsilon}\right) = Ra\left(T - BC\right) \\ &\frac{\partial T}{\partial t} + \left(\vec{u} \cdot \nabla\right)T = \nabla^2 T \end{aligned}\right\} \quad 4.3$$

where $\vec{u}$ is velocity, P is the dynamic pressure, η is the dynamic viscosity, $\dot{\bar{\varepsilon}}$ is the strain rate, T is the temperature, C is the composition (C = 1 for water and C = 0 for ice), and t is the time. All variables are non-dimensional. Ra and B are two non-dimensional parameters that control the vigor of convection and are defined as follows.

The thermal Rayleigh number, $Ra = \frac{\alpha \rho g \Delta T h^3}{\kappa \eta_m}$ 4.4

where α, ρ, g, κ are material parameters for ice, g is the acceleration due to gravity, η_m is the melting viscosity of ice (i.e., the viscosity at the base of the ice-shell), h is the thickness of the system and ΔT is a non-dimensionalising constant for temperature (approximately consistent with the temperature difference across the shell). All values are provided in Table 4.1.

The intrinsic density is represented by the buoyancy ratio, B as:

$$B = \frac{\Delta \rho}{\rho \alpha \Delta T} \quad 4.5$$

where $\Delta\rho$ is a constant representing the density contrast between liquid water and solid ice at reference T = 273.15 K and P = 1 bar, ρ and α are material properties of ice as listed in Table 4.1. ΔT is a non-dimensionalising constant related to temperature.

Table 4.1

Fixed Parameters Used in the Models

Parameter	Value
Gravitational acceleration (g)	1.3 ms^{-2}
Temperature at the surface (T_s)	95 K
Thickness of the model (h)	100 km
Melting temperature of ice (T_m)	Function of pressure (~273.15 K)
Melting viscosity of ice (η_m)	10^{16} Pa-s
Density of ice (ρ_i)	917 kgm^{-3}
Density of water (ρ_w)	1000 kgm^{-3}
Thermal expansivity of ice (α)	1.6 x 10^{-4} K^{-1}
Thermal diffusivity of ice (κ)	1.0 x 10^{-6} m^2s^{-1}
Thermal conductivity of ice (K)	3.3 $Wm^{-1}K^{-1}$

The model self-consistently assigns the phase (water or ice) to each finite element according to the phase diagram of pure water ice Ih [*Dunaeva et al.*, 2010; *Allu Peddinti and McNamara*, 2015]. This is determined as the temperature- and pressure-dependent phase change given by,

$$T(P) = a + bP + c\ln P + d/P + e\sqrt{P} \qquad 4.6$$

a = 273.0159, b = -0.0132, c = -0.1577, d = 0.0, e = 0.1516

where T is the dimensional temperature in K, P is the dimensional pressure in bar and the coefficients a, b, c, d and e are obtained from experimental data.

Boundary Conditions

We solve the equations for mass, momentum and energy in a two dimensional Cartesian geometry. The velocity boundary conditions at all boundaries of the domain are free slip. The temperature at the top boundary is isothermal and its value is set to zero (non-dimensional). There is no heat flow at the bottom boundary of the model.

We use the ratio tracer method to advect the compositional field [e.g., *Tackley and King*, 2003] in our model with compositional tracers for the species of ice and water. Our model domain has an aspect ratio of 3 and we use over 8 million tracers to track the phase composition field.

Rheology

Ductile deformation of a material can be described [*Goldsby and Kohlstedt*, 2001] by,

$$\dot{\varepsilon} = A\sigma^n d^{-p} \exp\left(-\frac{Q+PV}{RT}\right) \qquad 4.7$$

Where ε is the strain rate, σ is the differential applied stress and d is the grain size. A, n and p are rheological constants. Q and V are activation energy and volume respectively while P, T are the pressure and temperature and R is the gas constant. While the grain size is critical in determining the deformation mechanism [*Durham et al.*, 2010], it is also less constrained for ice on Europa.

In a low stress and strain regime, as expected for Europa, ice predominantly deforms by diffusion creep [*Barr and Showman*, 2009; *Nimmo and Manga*, 2009]. Hence Newtonian flow (n = 1) with a grain-size dependence (p = 2) sufficiently describes ice deformation on Europa. A higher stress regime would result in non-Newtonian behavior, and several studies have analyzed ice-shell convection for dislocation creep [*Moore*, 2006; *Freeman et al.*, 2006; *Ruiz et al.*, 2006].

To retain simplicity and minimize the uncertainty of unknown free-parameters in our numerical experiments, our models use a Newtonian formulation for temperature-dependent ice viscosity [*Showman and Han*, 2004] given by,

$$\eta = \exp\left(A\left(\frac{T_m}{T} - 1 \right) \right) \quad 4.8$$

where η is the non-dimensional viscosity, A is an activation coefficient, T_m (K) is the melting temperature (as a function of pressure), and T (K) is the temperature. The dimensional viscosity can be calculated by multiplying with η_m, the melting viscosity of ice (10^{16} Pa-s).

Proxy Fluid Approximation

The viscosity of liquid water is many orders of magnitude lower than that of solid ice. Hence, it is numerically intractable to adequately resolve both the ice-shell and the liquid water ocean because the length-scales and timescales of convection in the ice and water layers are vastly different. Our numerical experiments are only concerned with resolving convection and heat transfer within the solid (ice-shell) portion of the model. The liquid (ocean) portion of the model only serves to introduce the phase change boundary in the model. Thus it provides a self-consistent, dynamically-changing shell thickness and an effectively stress-free bottom boundary of the ice-shell. Therefore, we do not need to simulate a realistic, vigorously convecting liquid water ocean. Instead we employ a proxy fluid approximation for the liquid ocean [*Allu Peddinti and McNamara,* 2015], in which the viscosity of the fluid is 100x less than that of the lowest viscosity ice (melting viscosity of ice). This provides a mechanical decoupling between the solid ice and the liquid ocean layers while allowing rapid heat transport throughout the liquid ocean. A similar approach has been used in geodynamical modeling of free-surface motions in terrestrial mantle convection studies where the atmosphere is modeled as a fluid that has

a much higher viscosity than air, yet lower than the viscosity of the rock layer [*Crameri et al.*, 2012].

Tidal Internal Heating

Tidal internal heating depends on viscosity which in turn is strongly temperature dependent. Hence, based on the temperature and viscosity structure of the ice-shell, the magnitude of tidal heating would vary in different regions within the ice-shell.

The schematic plot shown in Figure 4.1 illustrates the general behavior of tidal dissipation as a function of viscosity of ice. This is the shape of the curve generated by equation 4.2. Tidal dissipation is low for the both the lowest and highest viscosities and reaches a maximum value at an intermediate viscosity. The viscosity of the ice-shell is temperature dependent. Hence ice is less viscous at the base of the ice-shell and the viscosity is highest in the ice-lid at the top of the shell. Therefore, the peak tidal internal heating is expected to be produced at a depth between the viscous lid and the base of the ice-shell. We examine the effect of this localization of heat within the ice-shell on the ice-shell thickening and growth rate. We also study the diffuse heating mode, with constant tidal internal heating throughout the ice-shell. For the localized tidal heating case, we construct a simple viscosity-dependent function that is a parameterized version of equation 4.2. We use this function to maximize the tidal dissipation at a chosen viscosity value such that heating can be localized in different parts of an ice-shell. We simply describe the constant tidal heating-rate, $q = q_0$ as the base of a triangle and the peak of the triangle represents a maximum heating-rate, $q = q_{max}$. Thus, we can localize heating at certain viscosities such that the rest of the ice-shell has lower heating-rate, allowing spatial variation in heating-rate. The function resembles the plot shown in figure 4.1.

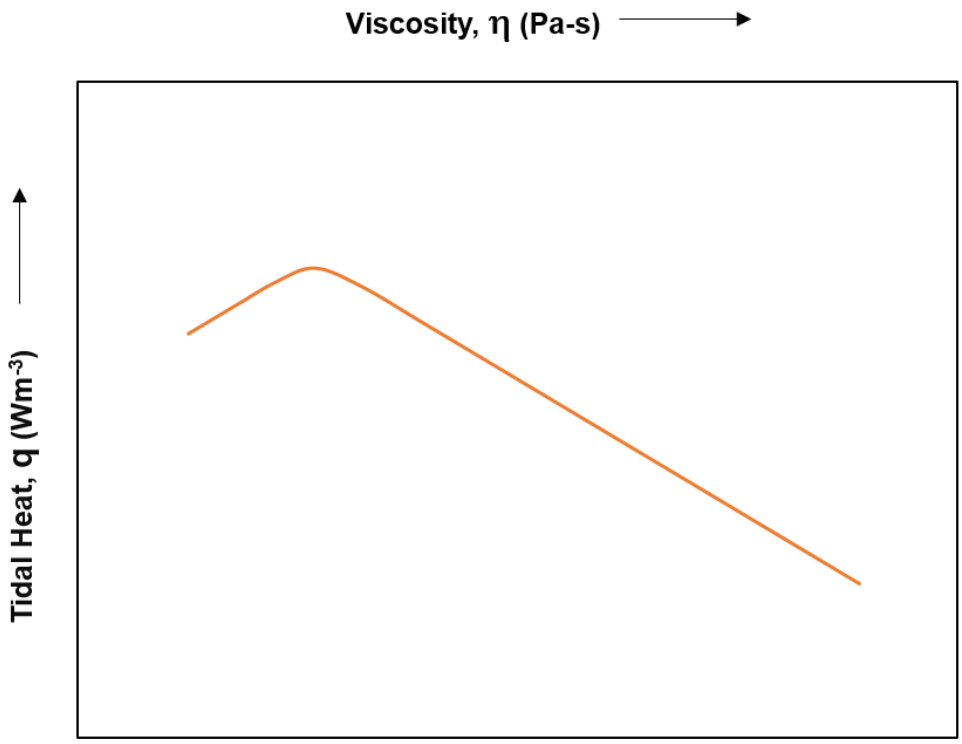

Figure 4.1. Schematic plot illustrating the functional form of tidal internal heating as a function of viscosity. Tidal heating is lowest at the lower and higher viscosities and is maximum at an intermediate viscosity value. Hence, depending on the viscosity structure of the system, the maximum tidal heating can be concentrated in different parts of the system.

Our aim is to understand if and how the growth rate of the ice-shell changes as the ice-shell thickens and if so, why. We examine how the convection patterns in the growing ice-shell affect the growth rate of the ice-shell. We hypothesize that the mode of tidal internal heating (diffuse or localized) might change (increase/decrease) the growth of the ice-shell.

In order to provide a systematic approach, we define three cases of our experiment. To simplify the experiment, we choose not to include the bottom heating (zero heat flux bottom boundary condition). Therefore, we examine the system as it cools to reach equilibrium between tidal internal heating and the surface heat loss. In order to provide a control for our numerical experiments, we first employ a case with no tidal

internal heating (Case A). In this case, the system simply cools from the top until the entire H_2O layer freezes. We then examine the diffuse heating mode in our second case, Case B. This case prescribes a constant, uniform tidal internal heating throughout the ice-shell. Finally, for the localized tidal internal heating mode, we define Case C, where the tidal internal heating within the ice-shell is a function of the viscosity of ice.

4.6 Results

We examine the ice-shell growth rate (i.e., ice-shell thickness as a function of time) for three scenarios: a control case with no internal heating (Case A), uniform tidal internal heating throughout the ice-shell (Case B), and localized tidal internal heating in the shell (Case C). We employ a temperature dependence of viscosity (A = 10.0 leading to a viscosity contrast of ~10,000X across the ice-shell).

In all of our numerical experiments, we employ non-dimensional values of the parameters. We present few of the results in dimensional units (such as temperature and viscosity); however, for quick conversion between the non-dimensional and dimensional values, we provide a list of dimensionalisation factors in Table 4.2. For example dimensional time, t (in seconds) can be calculated as,

$$t = t' \left(\frac{h^2}{\kappa} \right) \tag{4.9}$$

Where t' is the non-dimensional time, h is the thickness of the system (m) and κ is the thermal diffusivity (m^2/s). The values of h and κ are provided in Table 4.1. Therefore, a simple way to compute dimensional values from non-dimensional values using conversion factors from Table 4.2 is given by,

$\text{Parameter}_{\text{dimensional}} = \text{Parameter}_{\text{non-dimensional}}$ x Dimensionalisation factor

For calculating dimensional temperature, T, we use $T = T_s + \Delta T T'$ 4.10

Where T_s is the temperature at the surface (top of the model) and ΔT is a non-dimensional constant.

Table 4.2

Dimensionalisation Factors for the Parameters Used in the Models

Parameter	**Dimensionalisation Factor**
Thickness	h
Viscosity	η_m
Time	h^2/κ
Density	ρ_i
Heat	$K\Delta T/h^2$
Velocity	κ/h

Note: All constant values provided in Table 4.1 and ΔT is a constant temperature difference chosen across the system (~ 185 K).

It should be noted that for computational efficiency, we employ a higher melting viscosity of ice than what is hypothesized for Europa. This results in a lower Rayleigh number, and hence lower convective vigor, than is expected in reality. Therefore, one should take caution in interpreting dimensional time too rigorously as our models produce timescales that are probably longer than in reality. Instead, results should be viewed in a comparative manner between calculations.

Case A: Control case with No Internal Tidal Heating (q = 0.0)

Case A is a control case with no tidal internal heating. Since our experiments do not include bottom heating, this case is expected to completely freeze the H_2O layer as the initially warm system cools over time. Hence, this cooling problem provides a useful control to compare the experiments with tidal internal heating to, in order to better

recognize the influence that tidal heating may or may not have on ice-shell growth rate. Figure 4.2 shows four snapshots at different times. Figure 4.2(A) is a snapshot very early in the calculation (2 million years after initiation). Panels from top to bottom show the logarithm of non-dimensional viscosity, the phase (ice or water), and non-dimensional temperature respectively. At this early stage in the calculation, the system remains quite hot, and therefore, the ice-shell is thin (~ 20 km). Furthermore, the ice-shell has a high viscosity, particularly near the surface, due to the strong temperature-dependence of viscosity. The horizontally-averaged, non-dimensional root-mean-square velocity, temperature, and logarithm of viscosity are plotted as blue curves in figures 4.3(A), (B) and (C). The velocity depth profile is useful to identify the conductive, stagnant lid portion (zero velocity) of the ice-shell versus the convecting portion (non-zero velocity). At this early time, the thin ice shell is primarily a stagnant lid, transferring heat via conduction, evidenced by the zero velocities, linear temperature profile, and high viscosity. However, some advection is occurring in the lowermost portion of the shell, indicated by non-zero velocities and the slight non-linear, steepening curvature of the average temperature. Note that beneath the ice shell, temperature with depth is nearly uniform due to the vigorous convection within the low-viscosity proxy fluid (representing the liquid water ocean) that acts to rapidly homogenize temperature anomalies.

Figure 4.2(B) shows a second snapshot of Case A, at a later time (~ 9.5 million years). The ice-shell is thicker at this time (~45 km), and well-established convection cells within the ice-shell are evident by the undulating iso-contours in the viscosity and temperature fields. This snapshot intentionally captures a moment when two convection cells (towards the left in the temperature field) are in the process of merging into one

larger ice-convection shell. Before this merger, there were 9 convection cells, and afterwards, 8 cells. This is the natural response to the convective layer attempting to maintain a consistent aspect ratio of convection cell width to height as the ice shell thickens. The horizontally-averaged, non-dimensional root-mean-square velocity, temperature, and logarithm of viscosity are plotted as orange curves in figures 4.3(A), (B) and (C) respectively. Inspection of the average temperature reveals the dominance of conduction throughout the upper half of the ice shell (by the linear depth dependence of the average temperature).

Figure 4.2(C) shows a snapshot at a later time (~ 14.5 million years). The system has cooled further, leading to a much thicker ice-shell (~85 km) with larger and fewer convection cells (now 7) in comparison to the second snapshot, in figure 4.2(B). However, the aspect ratio (width/height) of each convection cell is quite small, indicating that ice shell thickness is increasing faster than the system can merge convection cells. The horizontally-averaged, non-dimensional root-mean-square velocity, temperature, and logarithm of viscosity are plotted as green curves in figures 4.3(A), (B) and (C) respectively. The mostly conductive portion of the shell remains at about ~25 km, similar to the previous snapshot. Finally, the entire system becomes frozen over, shown in figure 4.2(D) at a time ~ 20 million years after the start of the calculation. Once ice shell growth reached its maximum extent, the convection cells increased their aspect ratio, resulting in a final configuration of 2 convection cells.

Ice-shell thickness as a function of time is shown in figure 4.4. Note that the slope of this curve is the growth-rate of the ice-shell. Blue, orange, and green colored arrows indicate times of 2, 9.5, and 14.5 million years after the start of the calculation,

corresponding to the snapshots shown in figures 4.2(A), (B), and (C), respectively. After a short time (~3 million years) of rapid ice shell growth, the growth-rate remains relatively constant for the next ~5 million years. At about 8 million years after the start of the calculation, the growth rate makes a sudden and dramatic increase. This corresponds to the merging of convection cells and reconfiguration of the convective planform (as shown midway through the process in figure 4.2(B)). After the reconfiguration, the growth rate is nearly double its previous value. In dimensional values, these growth-rates are roughly 5.67 km/Myr and 8.22 km/Myr, respectively, but note our previous caveat that absolute dimensional times should be interpreted with caution, and that they are only meaningful in a comparative sense. In other words, it is the near-doubling of growth-rate that is significant, not the growth-rates themselves. The reconfiguration of convection planform, increasing the aspect ratio of convection cells, leads to more effective heat loss and therefore, more rapid cooling and thickening of the ice shell.

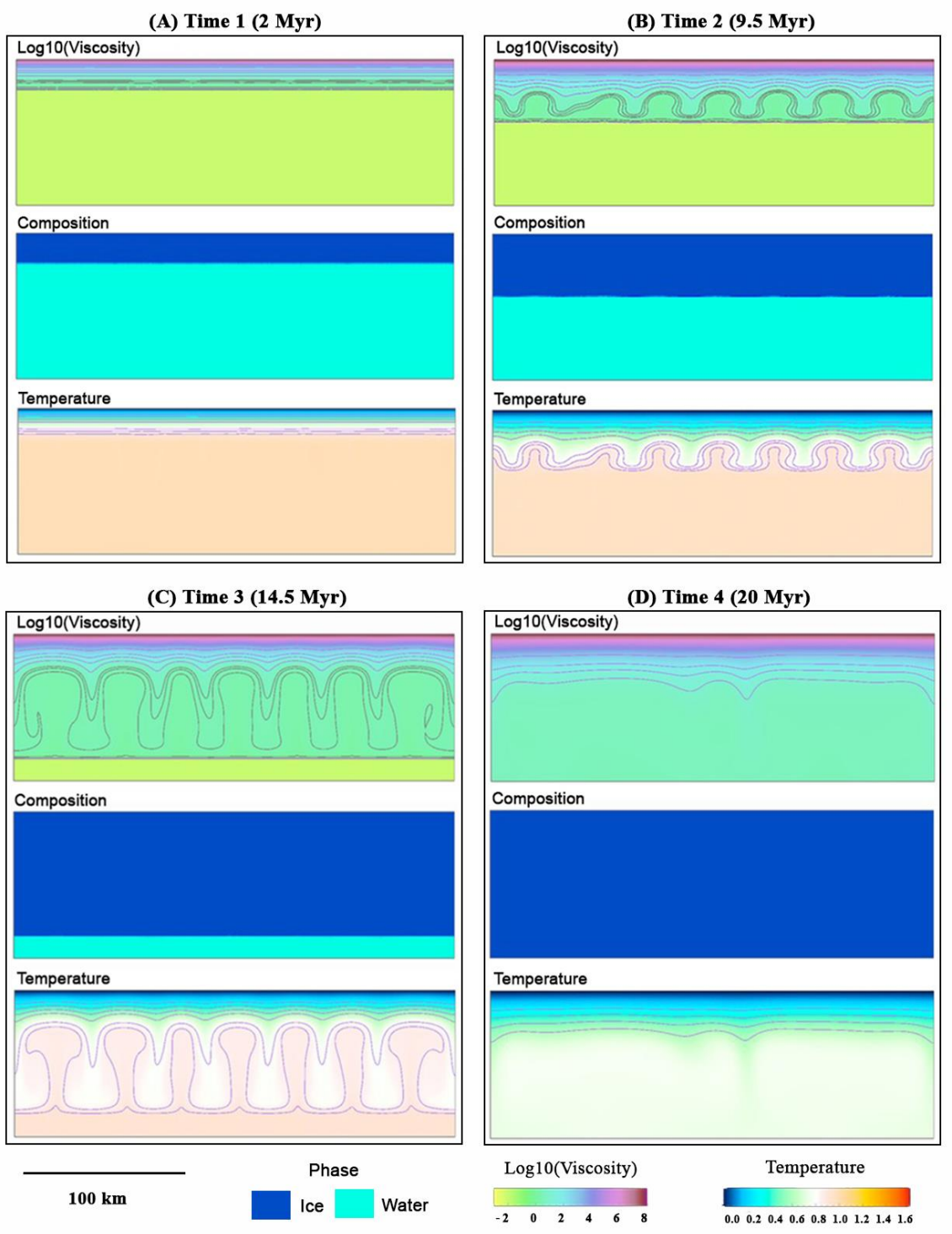

Figure 4.2. Time Snapshots from Case A. (A) 2 Myr; (B) 9.5 Myr; (C) 14.5 Myr; (D) 20 Myr from the beginning of the calculation. The top panel displays the logarithm of viscosity (yellow: low; purple: high) with the contours outlining each order of magnitude increase in viscosity. The middle panel shows the phase composition where deep blue represents ice and the light blue represents the proxy fluid (the liquid ocean). The bottom panel displays the temperature.

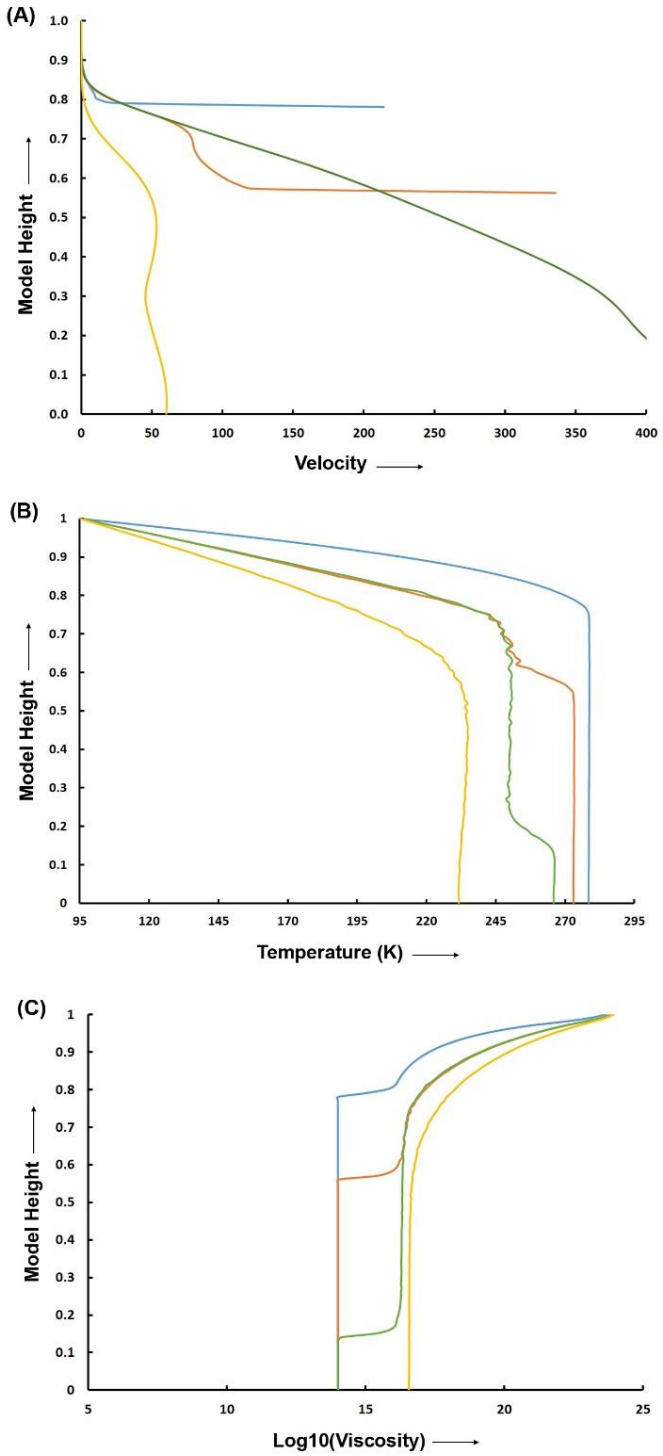

Figure 4.3. Case A**.** (A) Horizontally-averaged root-mean-squared non-dimensional velocity (speed) as a function of model height corresponding to 2 Myr (blue), 9.5 Myr (orange), 14.5 Myr (green) and 20 Myr (yellow) after start of the calculation. Velocities in the liquid water ocean layer are excluded. (B) Horizontally-averaged temperature as a function of model height, and (C) Horizontal average of logarithm of viscosity (Pas) as a function of model height corresponding to 2 Myr (blue), 9.5 Myr (orange), 14.5 Myr (green) and 20 Myr (yellow) after the start of the calculation.

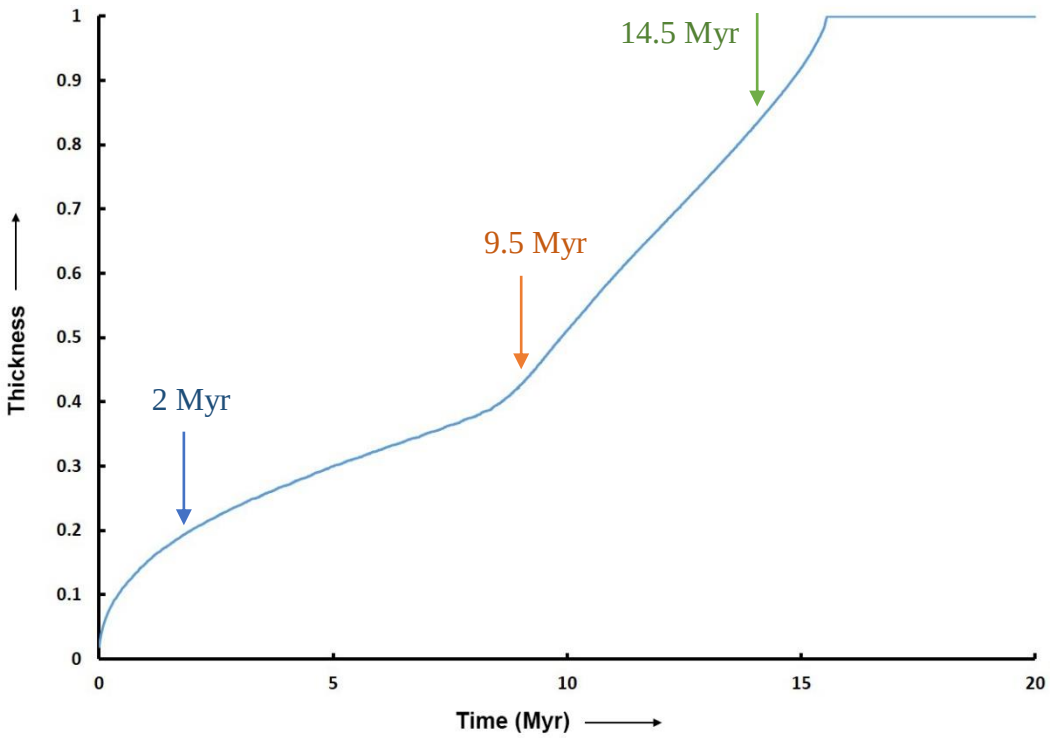

Figure 4.4. Ice-Shell thickness as a function of time: Case A. Non-dimensional shell thickness and growth rate corresponding to times 2 Myr (blue arrow), 9.5 Myr (orange arrow), and 14.5 Myr (green arrow) since the beginning of the calculation.

The Rayleigh number is often used to measure convective vigor of the system. However the Rayleigh number is simply a collection of non-dimensionalisation constants, and therefore it loses direct physical relevance when employing temperature-dependent viscosity and/or a layer of changing thickness (i.e., the ice shell) as we do in these experiments. All other things being equal, increasing the thickness of the ice shell acts to increase the vigor of convection within it, in a cubed manner. Similarly, as the ice shell cools and decreases its temperature, overall viscosity increases, decreasing the convective vigor within the ice. Taking these into account, we quantify the vigor of convection within the ice shell by an effective Rayleigh number, here denoted by Ra_{eff}, that takes these considerations into account.

$$Ra_{eff} = Ra\left(\frac{h_{ice-shell}^3}{\langle \eta \rangle}\right) \quad 4.11$$

Where $\langle \eta \rangle$ is the volume- and log-averaged non-dimensional viscosity throughout the ice-shell and $h_{ice\text{-}shell}$ is the thickness of the ice-shell. Figure 4.5 illustrates how the Ra_{eff} changes with time as the ice-shell grows. In general, the Ra_{eff} increases as the thickness increases due to cooling. At a later time corresponding to the merging of convection cells and resultant increase in convection cell aspect ratio, as noted in figure 4.4, Ra_{eff} undergoes a sharp increase, demonstrating increasing convective vigor at that time. When the system entirely freezes into an ice-shell, and the ice-shell thickness remains nearly constant, the Ra_{eff} decreases as the system cools further.

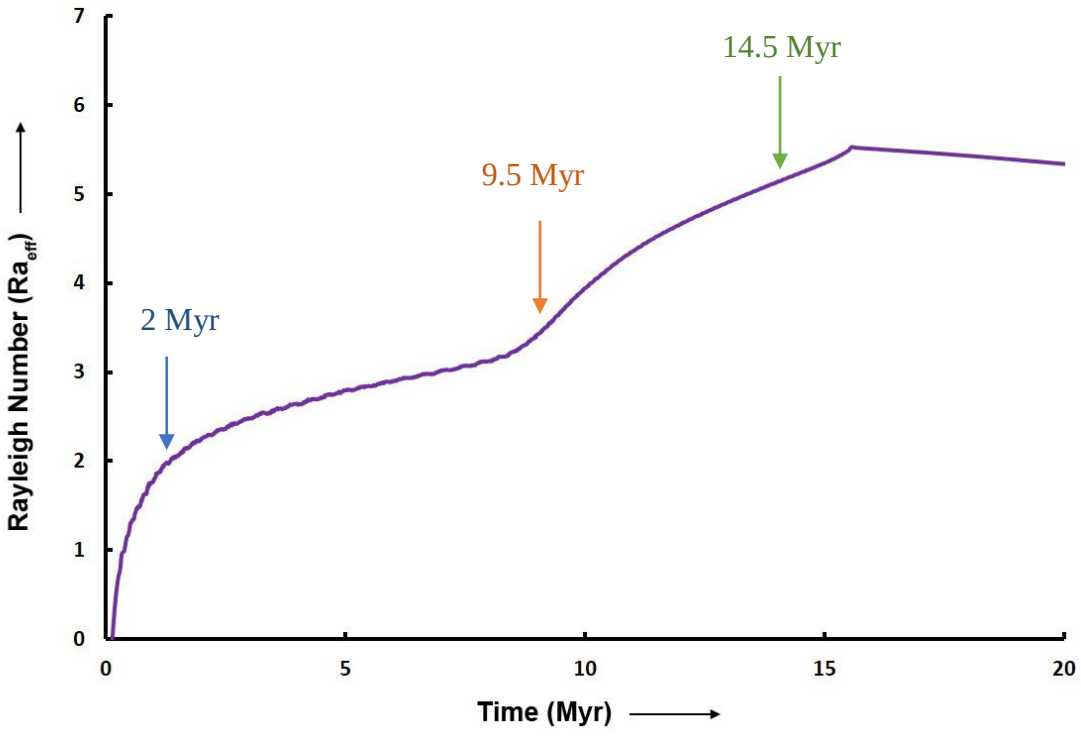

Figure 4.5. Rayleigh number as a function of time: Case A. Logarithm of effective Rayleigh number corresponding to times 2 Myr (blue arrow), 9.5 Myr (orange arrow), and 14.5 Myr (green arrow) since the beginning of the calculation.

In summary, without heat sources, an initially hot ocean system will ultimately cool to a completely frozen H_2O layer, as expected. Initially, a thin ice-shell quickly forms, and heat is transferred primarily by conduction. As the system cools further, the ice-shell thickness increases and undergoes convection beneath a stagnant/sluggish viscous lid that remains at the top ~25 km. As the ice-shell thickens, the aspect ratio (width/depth) of convection cells decreases, which becomes an unstable convective planform. The convective system responds by merging convection cells, increasing the average aspect ratio of the remaining cells. Once it does, ice-shell growth rate dramatically increases, and the ice-shell thickens faster than the convective planform can respond. Once ice-shell growth stops due to the H_2O layer becoming completely frozen, convection cells merge once again, resulting in only two cells.

Case B: Uniform Tidal Internal Heating in the Ice-Shell (q = constant)

In Case B, we apply a uniform tidal internal heating-rate (non-dimensional value of 10) throughout the entire ice-shell. As a consequence, the total amount of heating will increase as the ice-shell thickens. Figure 4.6(A) shows an early snapshot of this case (~ 2 million years from the beginning of the calculation), when the initial warm ocean layer has slightly cooled to form a thin ice-shell. The corresponding horizontally-averaged velocity, temperature, and logarithm of viscosity as functions of the model height are shown as blue curves in figures 4.7(A), (B) and (C). Because the system is still hot at this early time, the ice-shell is thin and heat is transferred mostly by conduction, although there is some advection of ice at the base of the shell. The temperature-dependence of viscosity leads to the formation of a high viscosity stagnant/sluggish lid, encompassing

most of the shell. At this time, the ice-shell exhibits similar characteristics to the ice-shell in the early stage of Case A (figure 4.2(A)).

Figure 4.6(B) shows a snapshot at ~ 11 million years after the start of the calculation. The ice-shell has thickened to ~ 35 km, and convection occurs in the bottom half of the ice-shell, as evidenced by the temperature field and the horizontally-averaged velocity and temperature curves (orange curves in figure 4.7(A) and 4.7(B)). The velocity curve in figure 4.7(A) (in orange color) identifies a conducting viscous ice-lid atop the shell above the advecting ice. At this time, the convection planform is undergoing a merging of convection cells, from 9 cells to 6, in the right half of the ice-shell. Figure 4.6(C) provides a snapshot at a later time (~ 13 million years after initiation). From the temperature panel, it is clear that the merging of convection cells has completed. Therefore, now there are 6 ice-convection cells instead of 9, resulting in a larger aspect ratio for all cells. Inspection of the horizontally-averaged velocity as a function of model-height (green curve, figure 4.7(A)) indicates an increased vigor of convection compared to earlier times.

Unlike Case A, in which the lack of additional heat source had caused the entire system to freeze over, Case B reaches an equilibrium thickness (~ 55 km) due to the internal tidal heating in the ice. Figure 4.6(D) shows a snapshot about 35 million years since the beginning of the experiment. The ice-convection pattern has further changed since the previous snapshot, with only 4 convection cells instead of 6.

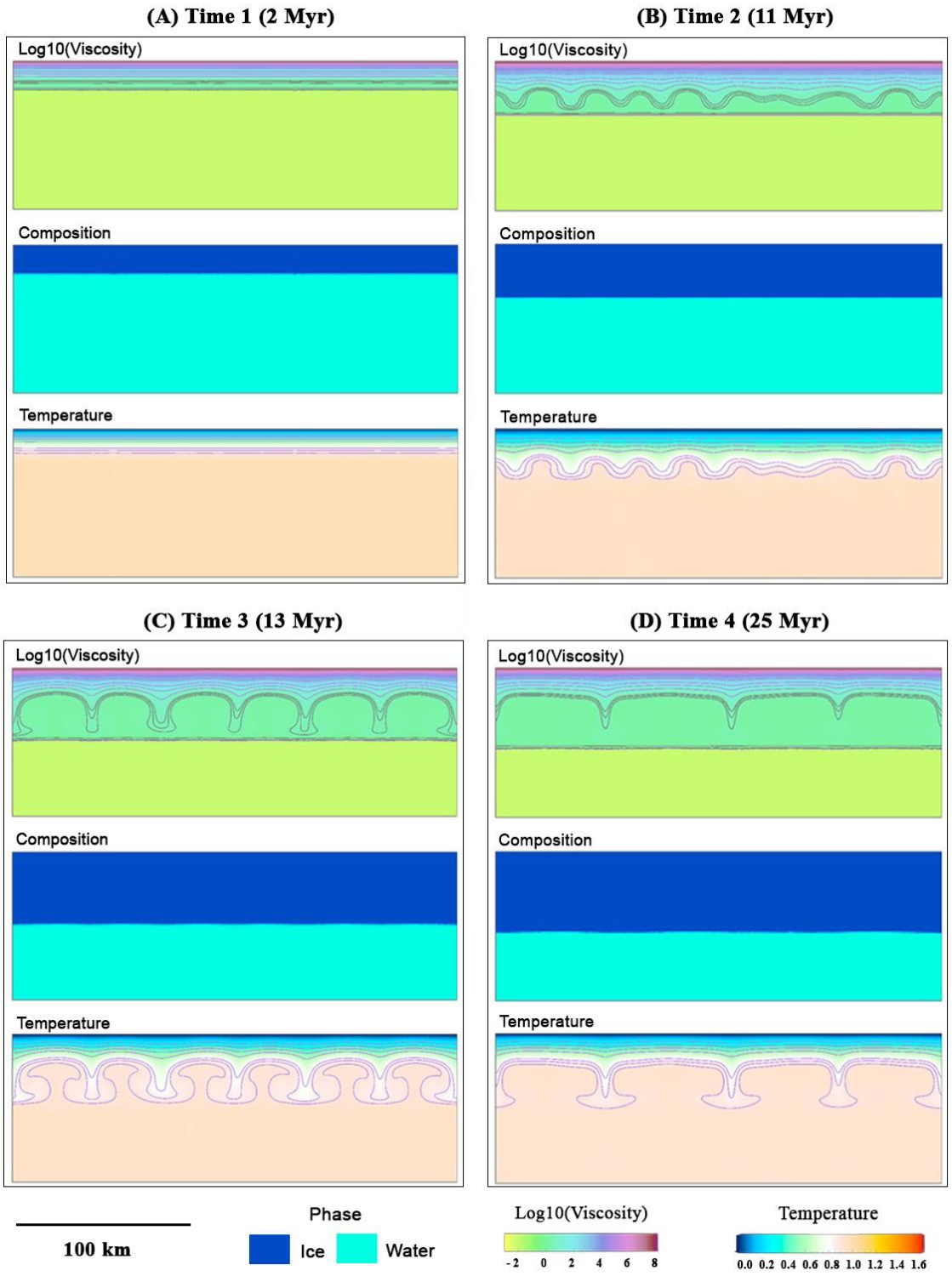

Figure 4.6. Time Snapshots from Case B. (A) 2 Myr; (B) 11 Myr; (C) 13 Myr; (D) 35 Myr from the beginning of the calculation. The top panel displays the logarithm of viscosity (yellow: low; purple: high) with the contours outlining each order of magnitude increase in viscosity. The middle panel shows the phase composition where deep blue represents ice and the light blue represents the proxy fluid (the liquid ocean). The bottom panel displays the temperature.

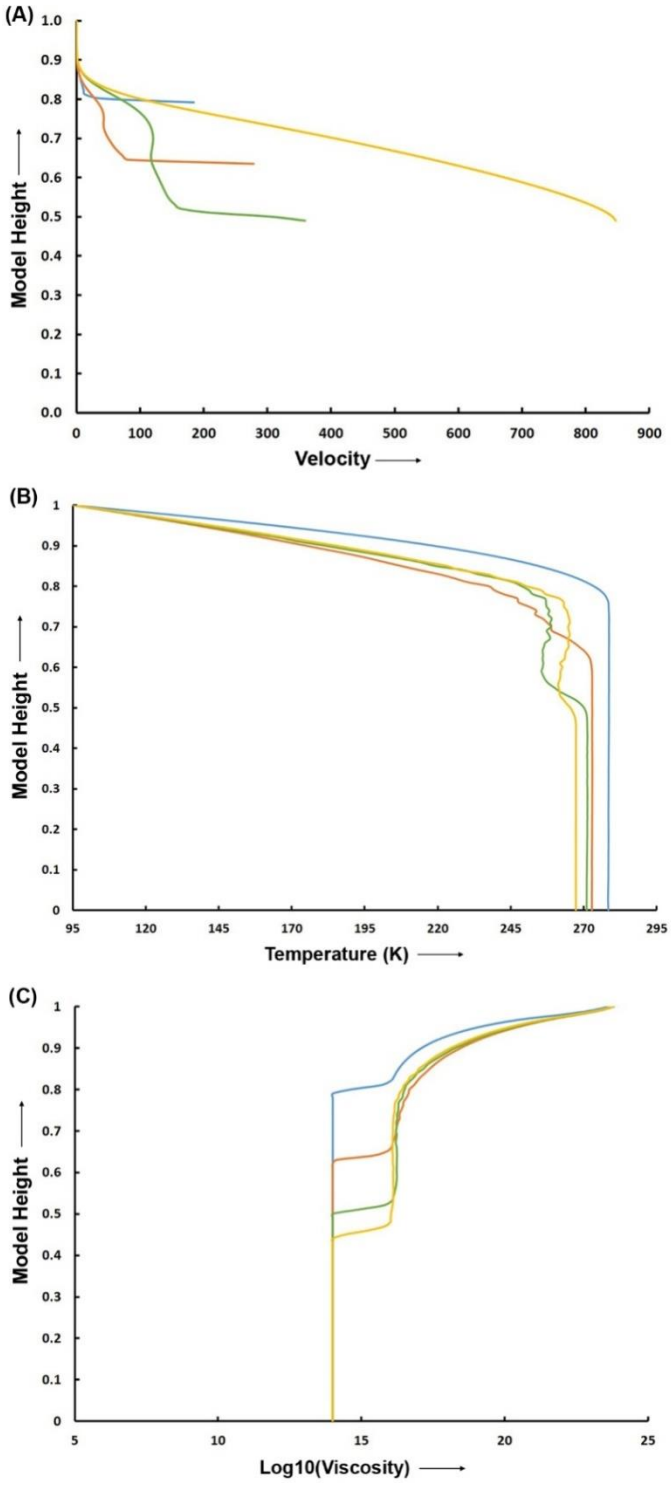

Figure 4.7. Case B**.** (A) Horizontally-averaged root-mean-squared non-dimensional velocity (speed) as a function of model height corresponding to 2 Myr (blue), 11 Myr (orange), 13 Myr (green) and 35 Myr (yellow) after the start of the calculation. Velocities in the liquid water ocean layer are excluded. (B) Horizontally-averaged temperature as a function of model height, and (C) Horizontal average of logarithm of viscosity (Pas) as a function of model height corresponding to 2 Myr (blue), 11 Myr (orange), 13 Myr (green) and 35 Myr (yellow) after the start of the calculation.

Figures 4.8 and 4.9 show the ice-shell thickness and effective Rayleigh number, respectively, versus time. Blue, orange, and green arrows, point out the times of the snapshots shown in figures 4.6 (A), (B), and (C) respectively. Similar to Case A, we find a dramatic increase in ice-shell growth-rate and convective vigor associated with the merging of convection cells at around 11 million years. The Rayleigh number (Ra_{eff}), which indicates the vigor of convection, and changes with ice-shell thickness over time, also becomes nearly constant when the shell thickness remains unchanged (figure 4.9).

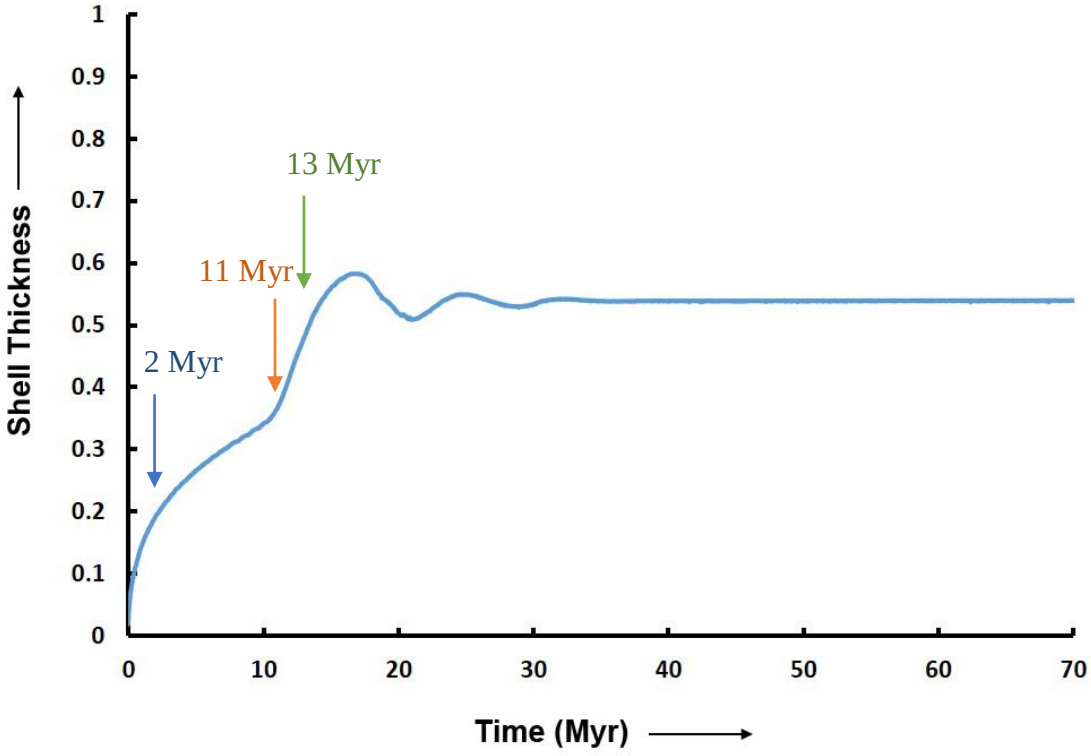

Figure 4.8. Ice-Shell thickness as a function of time: Case B. Non-dimensional shell thickness and growth rate corresponding to 2 Myr (blue arrow), 11 Myr (orange arrow), and 13 Myr (green arrow) since the beginning of the calculation.

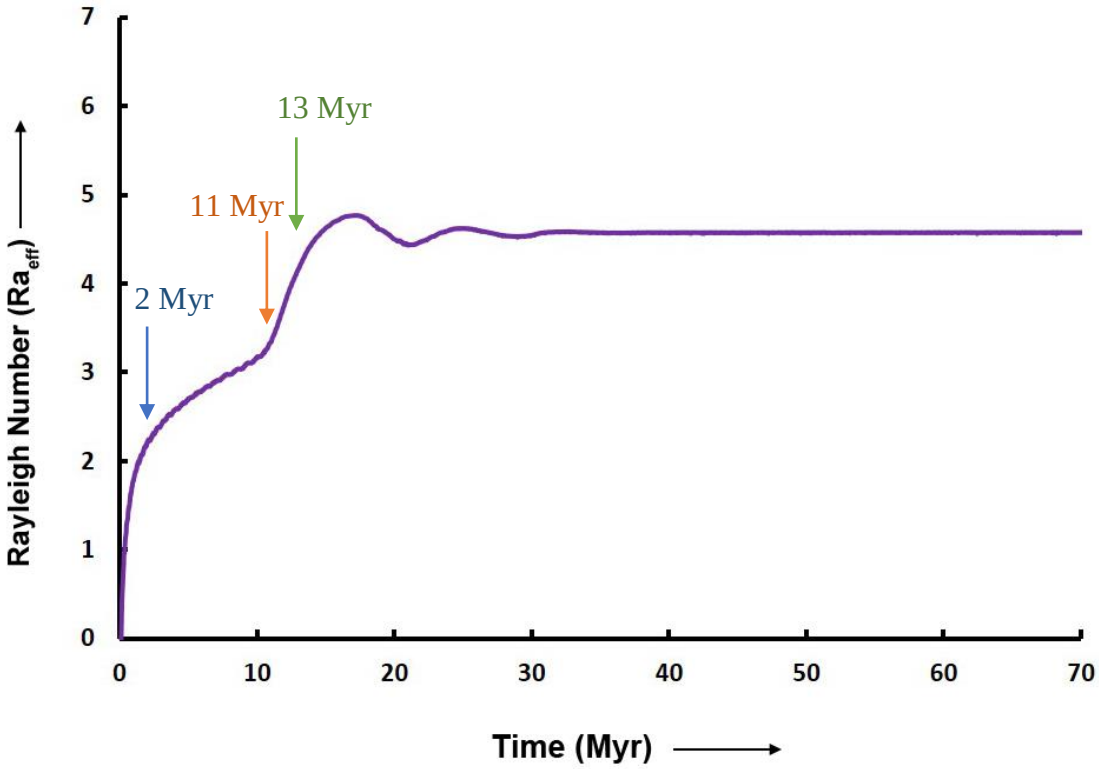

Figure 4.9. Rayleigh number as a function of time: Case B. Logarithm of effective Rayleigh number corresponding to 2 Myr (blue arrow), 11 Myr (orange arrow), and 13 Myr (green arrow) years since the beginning of the calculation.

As expected, the major difference between Case B (uniform tidal heating-rate) and the control Case A (no heat sources) is that the system doesn't completely freeze over when an adequate amount of tidal heating is employed. The inclusion of tidal heating allows for an equilibrium ice shell thickness of about 55 km (specific to Case B) in which the heat produced balances the heat lost. What is similar between the cases, however, is that as the ice-shell thickens, its convective planform undergoes a transition in which convection cells merge to increase the average aspect ratio of each cell. As it does, the growth-rate experiences a sudden and dramatic increase. Interestingly, shortly before reaching equilibrium, the model predicts a short-lived overshoot of ice-shell thickness, in which

the ice-shell briefly over-thickens (by about 5 km) before shrinking back down to its equilibrium thickness.

Case C: Viscosity-dependent Tidal Internal Heating in the Ice-Shell

Whereas Case B employed a constant, uniform tidal heating-rate, here we investigate more physically-consistent scenarios in which heating-rate depends on viscosity. As described in equation 4.2 and schematically illustrated in figure 4.1, tidal heating-rate exhibits a maximum for intermediate viscosities. It is unclear how to directly apply this formulism to our models for two reasons: (1) it is unclear what the viscosity magnitude and variation is within Europa's ice shell, and (2) as described earlier, our models employ a Rayleigh number (hence viscosity magnitude) that is likely higher than exists on Europa. Therefore, we examine the three different variations in which the peak heating-rate (i.e., the maximum in figure 4.1) is positioned in different locations within the ice shell. Cases C1, C2, and C3 have peak heat-rates in the upper, middle, and lower portions of the ice-shell, respectively. For each case, we impose a maximum non-dimensional heating rate value (i.e. peak heat-rate) of $q_{max} = 30.0$. We define a non-dimensional base heating rate value $q_0 = 10.0$ (equivalent to the heating-rate value used in Case B).

(1) In Case C1, the tidal heating rate is localized (maximum) in the upper portion of the shell (i.e. the convecting ice underneath the viscous lid). Figure 4.10 (A) shows an early time snapshot (~ 11 million years) of a thick, convecting ice-shell. An additional panel at the bottom of the snapshot shows the logarithm of non-dimensional tidal heating rate within the ice-shell. The maximum heating rate is concentrated within a narrow range of ice-viscosities. At this time, reconfiguration of the ice-convection planform begins to occur when the convection cells on the right half merge together (as evidenced in the

temperature panel). The ice-shell is convecting under a highly viscous lid as indicated by the ice-velocities, the temperature and viscosity across the ice-shell (blue curves in figures 4.11(A), (B) and (C)). The rest of the shell has lower heating rate diffused throughout the ice, as shown in the heat panel. Figure 4.10(B) shows a snapshot ~ 30 million years after initiation. The ice-convection cells from previous time have merged, resulting in a change in convection pattern. The corresponding ice-velocity, temperature and viscosity as functions of model height are shown by the orange curves in figures 4.11 (A), (B) and (C). Examining the growth of the shell over time (blue curve in figure 4.12), there is a dramatic increase in the growth rate when the ice-convection pattern changes. The ice-shell growth rate changes until it becomes zero which we speculate represents an equilibrium shell thickness (at ~ 54 km) when the heat lost via advection is balanced by tidal heat production within the shell. The change in vigor of convection (Ra_{eff}) with time is shown by the blue curve in figure 4.13. As the ice-shell thickens, and the viscosity increases, the vigor of convection increases and when the shell thickness remains constant, the ice-shell convects at nearly fixed Ra_{eff}.

(2) Next, in Case C2, we examine localization of tidal heating rate in the middle of the ice-shell. As shown in figure 4.1, the tidal heating rate is maximum at an intermediate viscosity. Hence we expect this experiment to best represent the equation 4.2. Figure 4.14(A) shows a snapshot of the model about 11 million years after initiation. The maximum tidal heating rate is localized at the intermediate viscosities within the ice-shell, in a relatively lower part of the shell compared to figure 4.10(A). The convection pattern of the shell changes as the ice grows and this is evident from comparing the temperature panels in figure 4.14(A), and at a later time in the snapshot shown in figure

4.14(B), about 35 million years since the beginning. The convection cells outlined by the undulating iso-contours in the temperature panel change shape and size as they merge together. The ice-shell growth rate increases as the convection pattern changes (orange curve in figure 4.12). The growth rate eventually becomes zero when the ice-shell reaches an equilibrium state where the heat lost is balanced by the tidal heat produced in the ice. The ice-shell thickness remains nearly constant at about 51 km. The vigor of convection i.e. the effective Ra number, which increases as the ice-convection patterns change and the shell thickens, also becomes uniform when the system attains an equilibrium state (orange curve in figure 4.13).

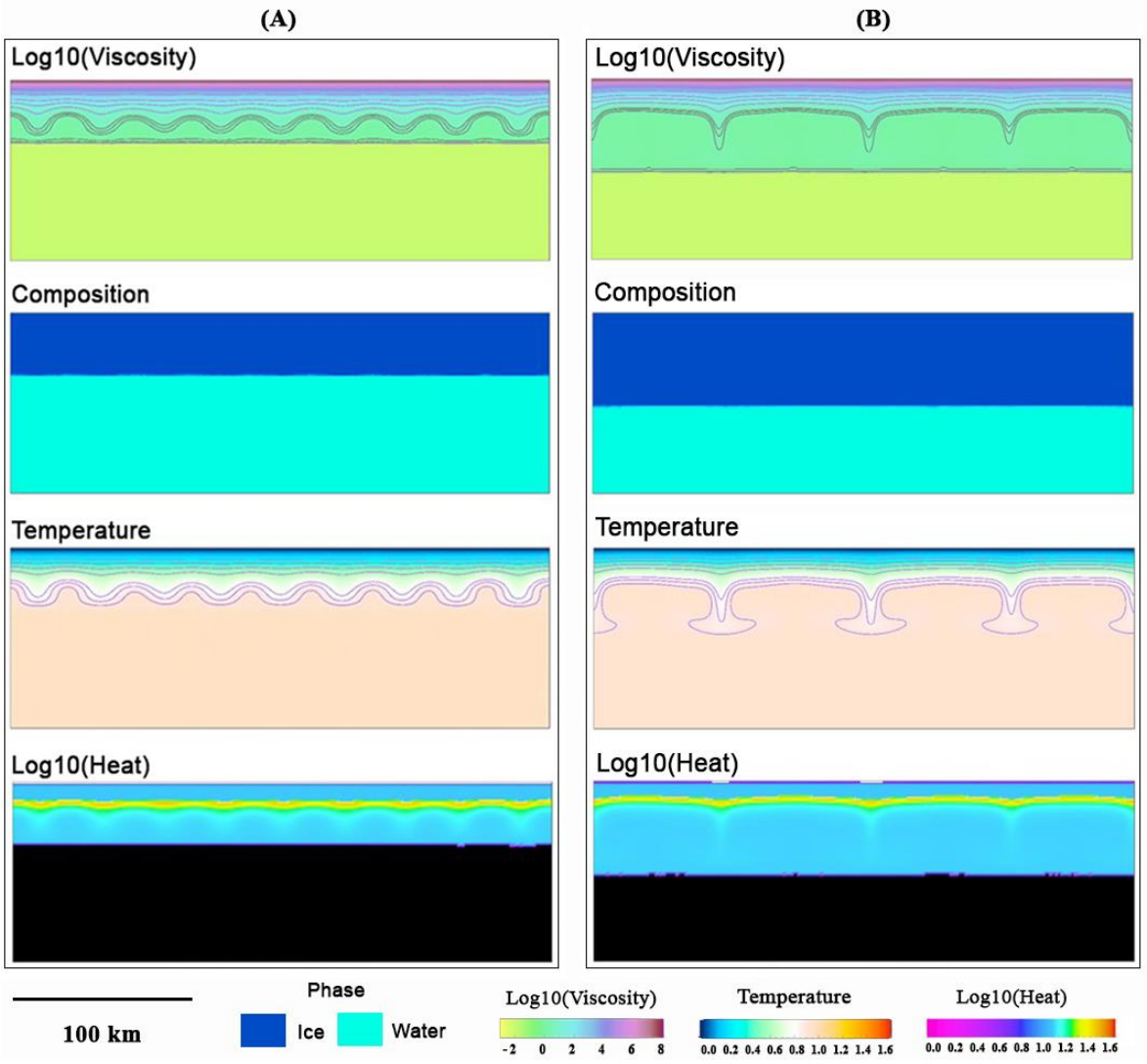

Figure 4.10. Time Snapshots from Case C1: Maximum heating localized under the viscous lid. (A) 11 Myr; (B) 30 Myr from the beginning of the calculation. The top panel displays the logarithm of viscosity (yellow: low; purple: high) with the contours outlining each order of magnitude increase in viscosity. The second panel shows the composition (phase) where deep blue represents ice and the light blue represents the proxy fluid (the liquid ocean). The third panel displays the temperature and the bottom panel shows the logarithm of heat (magenta: low; orange: high). There is no heating in the fluid layer and is hence shown in black in the heat panel.

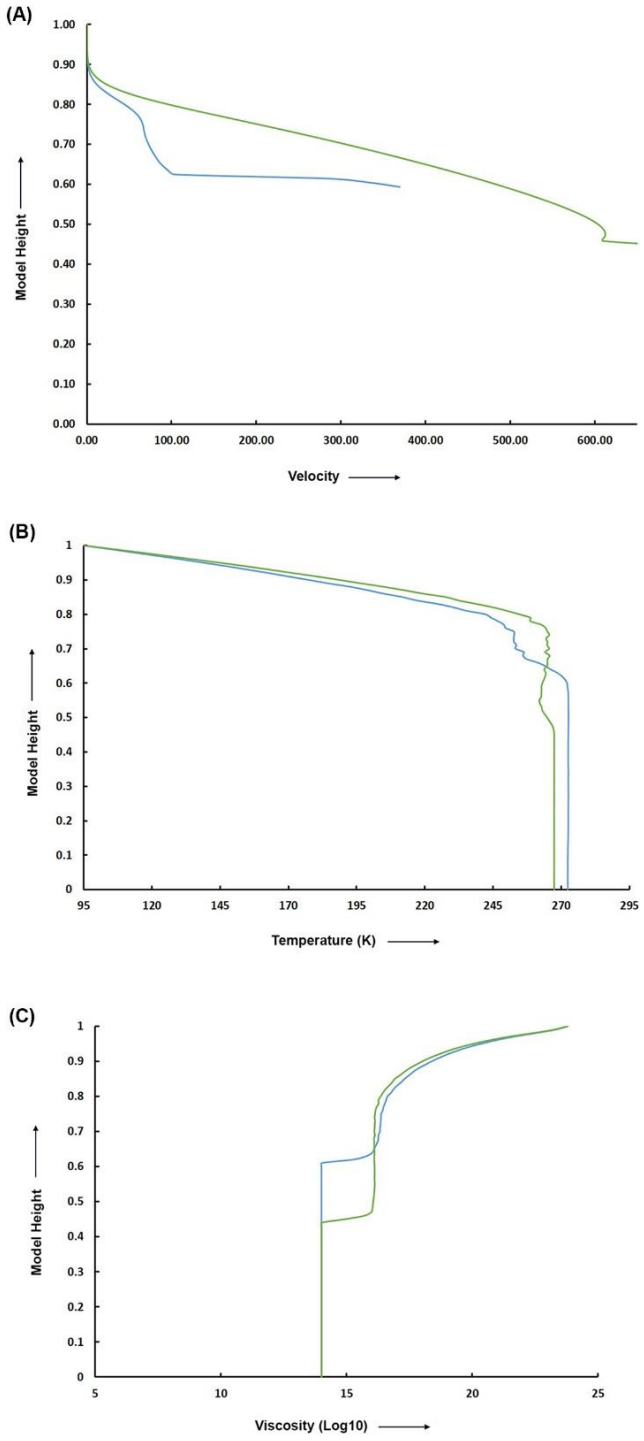

Figure 4.11. Case C1: Maximum heating localized under the viscous lid. (A) Horizontally-averaged root-mean-squared non-dimensional velocity (speed) as a function of model height corresponding to 11 Myr (blue), and 30 Myr (green) after the start of the calculation. Velocities in the liquid water ocean layer are excluded.
(B) Horizontally-averaged temperature as a function of model height corresponding to 11 Myr (blue), and 30 Myr (green), and (C) Horizontal average of logarithm of viscosity (Pas) as a function of model height corresponding to 11 Myr (blue), and 30 Myr (green) after the start of the calculation.

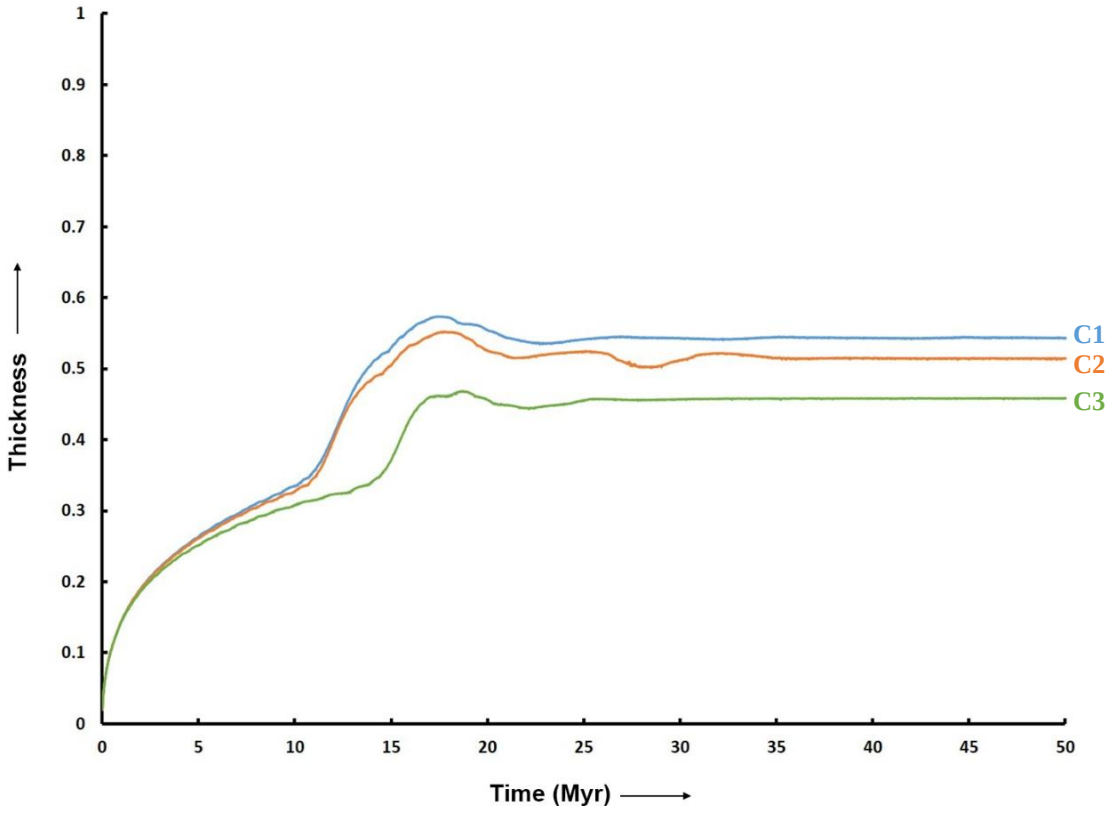

Figure 4.12. Ice-Shell thickness as a function of time: Case C. Non-dimensional shell thickness and growth rate corresponding to cases C1 localization of heat below the ice-lid (blue curve), C2 localization of heat in the middle of the shell (orange curve), and C3 localization of heat towards the base of the ice-shell (green curve).

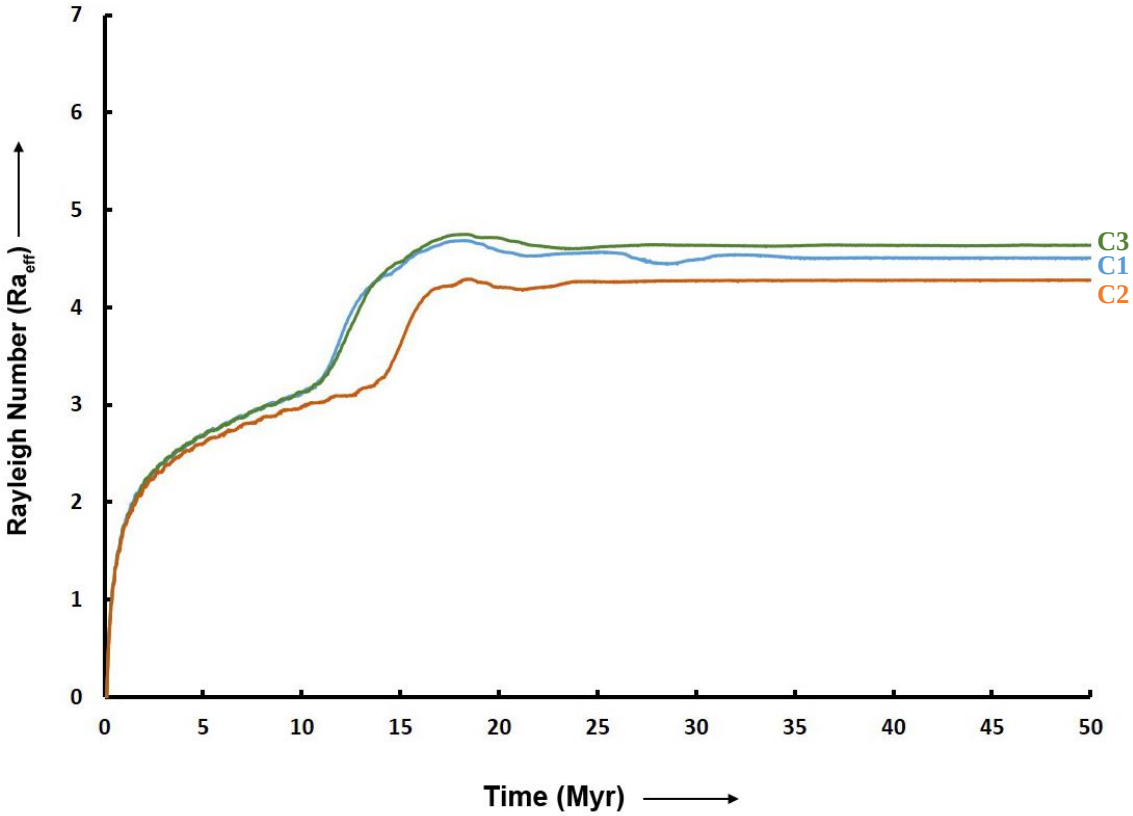

Figure 4.13. Rayleigh number as a function of time: Case C. Logarithm of effective Rayleigh number corresponding to cases C1 localization of heat below the ice-lid (blue curve), C2 localization of heat in the middle of the shell (orange curve), and C3 localization of heat towards the base of the ice-shell (green curve).

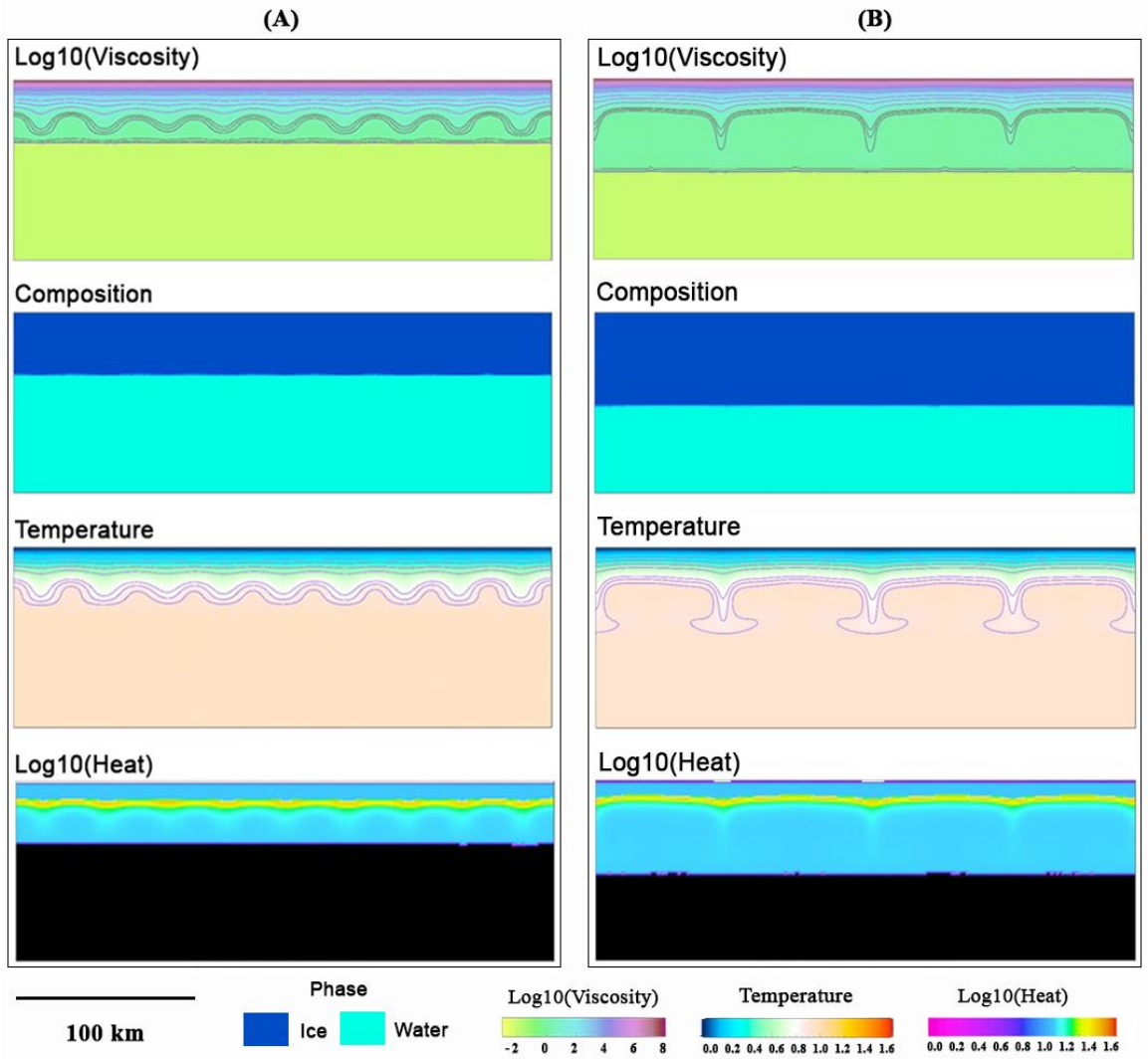

Figure 4.14. Time Snapshots from Case C2: Maximum heating localized in the middle of the shell. (A) 11 Myr; (B) 35 Myr from the beginning of the calculation. The top panel displays the logarithm of viscosity (yellow: low; purple: high) with the contours outlining each order of magnitude increase in viscosity. The second panel shows the composition (phase) where deep blue represents ice and the light blue represents the proxy fluid (the liquid ocean). The third panel displays the temperature and the bottom panel shows the logarithm of heat (magenta: low; orange: high). There is no heating in the fluid layer and is hence shown in black in the heat panel.

(3) In Case C3, the tidal heating rate is localized in the lower portion of the ice-shell i.e. maximum heating is concentrated at lower viscosities in comparison with cases C1 and C2. The heating-rate is localized in ice that outlines the shape of the ice-convection cells as shown in the heat panel of an early snapshot (~ 10 million years) in figure 4.15(A). In the temperature and viscosity panels of this snapshot, we identify the changing convection patterns in ice. The unstable convection cells in the shell merge together resulting in a sharp increase in the growth rate of the ice-shell. The ice-shell thus has fewer and larger convection cells in the snapshot (~ 26 million years) shown in figure 4.15(B). The ice-shell growth rate increases until it becomes zero when the shell attains an equilibrium thickness. Compared to cases C1 and C2, more heat is concentrated in the lower portion of the ice-shell as shown in the heat field. Thus, we expect the ice-shell to be relatively thin. Upon examining the growth rate curve (green curve in figure 4.12), we identify that after the increase in growth rate upon reconfiguration of ice-convection cells, the shell thickness remains constant at ~ 46 km. We thus expect the effective Rayleigh number (i.e. the convective vigor) to increase as the shell thickens, and remain unchanged once the shell reaches equilibrium (green curve in figure 4.13).

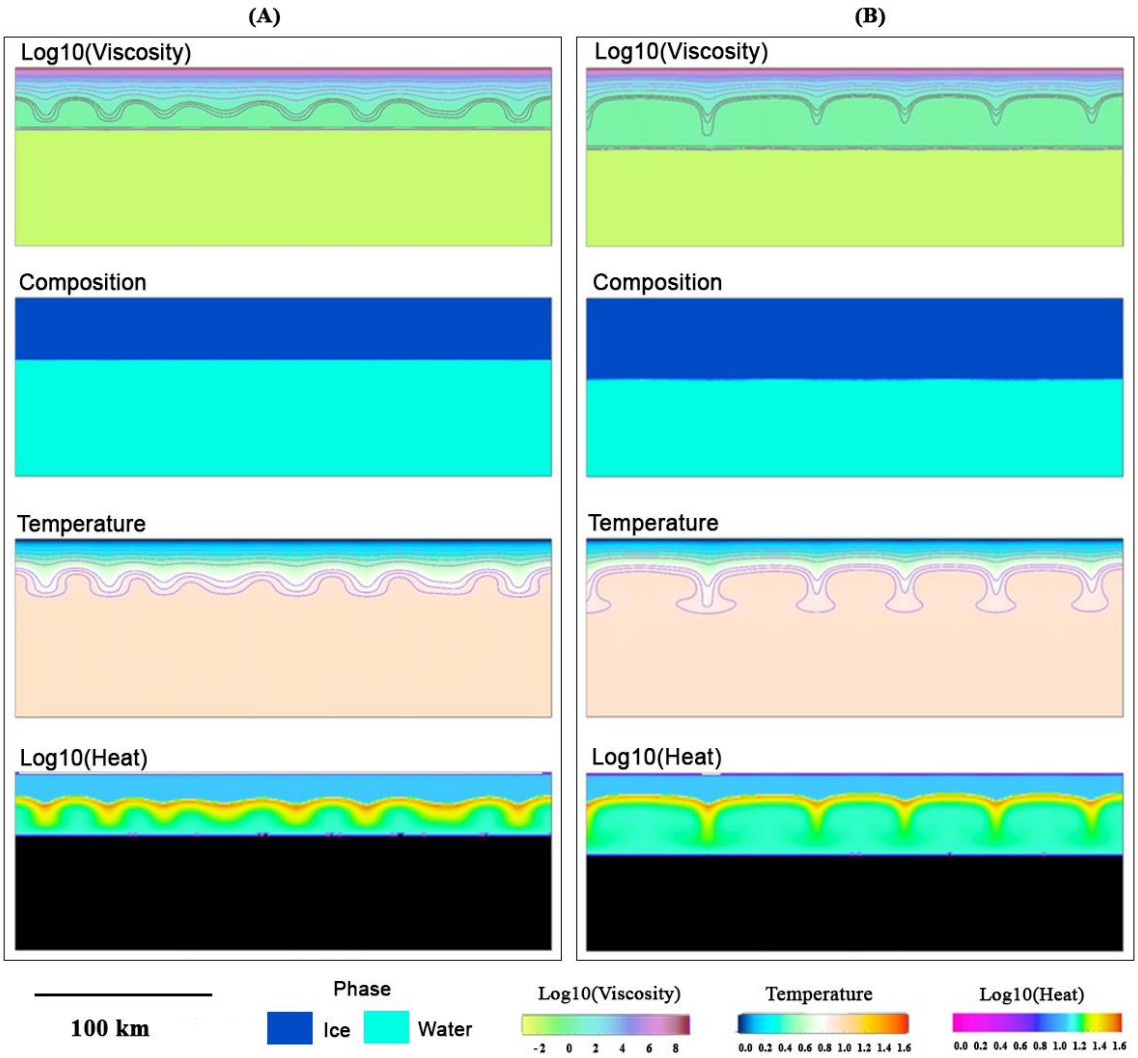

Figure 4.15. Time Snapshots from Case C3: Maximum heating localized towards the base of the shell. (A) 10 Myr; (B) 26 Myr from the beginning of the calculation. The top panel displays the logarithm of viscosity (yellow: low; purple: high) with the contours outlining each order of magnitude increase in viscosity. The second panel shows the composition (phase) where deep blue represents ice and the light blue represents the proxy fluid (the liquid ocean). The third panel displays the temperature and the bottom panel shows the logarithm of heat (magenta: low; orange: high). There is no heating in the fluid layer and is hence shown in black in the heat panel.

4.7 Discussion

In this work, we focus on investigating how the growth-rate of a thickening ice-shell changes as the system cools. In particular, we examine how the convection planform changes as the ice-shell thickens, and how this affects the growth rate. We designed the numerical experiments to be as simple as possible, to answer these specific questions. Therefore, it is important to emphasize that these experiments serve that aim, and therefore, do not serve as "simulations" of Europa. Here, we list several examples of how our experiments are intentional simplifications of a more complex planetary system.

For numerical practicality, our models use a lower Rayleigh number than may be predicted for Europa. This effectively means that our lowest viscosity for ice (at the melting temperature) is higher than that on Europa. We employ a melting viscosity of 10^{16} Pa-s, whereas estimates of melting viscosity on Europa are 10^{12}-10^{15} Pa-s [*Nimmo and Manga*, 2009]. Because we maintain a proxy fluid for the liquid ocean to have a viscosity two orders of magnitude below the melting viscosity, it becomes quite computationally expensive to employ lower values. We do not expect the higher Rayleigh number used in our calculations to change the conclusions of our study, but it will affect the interpretation of timescales and velocities, as noted earlier. We expect our calculations to have a somewhat lower vigor of convection than reality, and therefore, our timescales are longer, the growth-rates and velocities are lower.

Our experiments are performed under the Boussinesq approximation, and therefore, do not include adiabatic heating/cooling, flow-induced viscous dissipation, and latent heat of phase changes. We do not expect adiabatic effects to be important for such a thin ice-shell, and flow-induced viscous dissipation would be small compared to the tidal heating

that we employ. Latent heat could provide extra thermal energy to the system, although we would expect that much of it would be advected away by ocean currents [*Warren et al*., 2002]. Although it could serve to slow down the cooling, and therefore thickening, of the ice-shell, it is not expected to modify changes in the planform of convection, which plays the key role in our conclusions.

Our experiments also intentionally neglect heating from below the H_2O layer. We did include it in our initial, reconnaissance calculations (similar to our earlier work [*Allu Peddinti and McNamara*, 2015]); however, we found that it unnecessarily complicated our attempts to achieve final equilibrium scenarios of an ice shell existing over the top half of the H_2O layer. Each combination of bottom heating and tidal heating led to a different equilibrium thickness of the ice shell. Although it would be an interesting next step to explore the heat balance on ice-water worlds, our objective for these experiments was to generate a final system in which the ice-shell composes approximately 50% of the H_2O layer thickness. We find that inclusion of bottom heating acts to allow a reduction in tidal heating to achieve the same ice-shell thickness; however, it doesn't alter our conclusions regarding how changing convection planform modifies growth-rate of the shell.

Furthermore, our experiments assume that proxy fluid representing the liquid ocean maintains the same composition. In reality, the concentration of solutes would be expected to increase as the ice-shell thickens because the formation of new ice should mostly exclude them from the solid matrix. This would likely act to decrease the freezing temperature as the liquid ocean becomes more concentrated in solutes, in which case the ocean layer becomes more anti-freezing the thinner it gets. While this would be

interesting future work to investigate, we don't consider this effect to modify our general conclusions regarding growth-rate suddenly increasing upon a change in convective planform.

Tidal dissipation is expected to generate heat within the silicate interior and hence may affect the ice-shell thickening [*Nimmo and Manga*, 2009]. The Maxwell model of tidal dissipation is valid for Newtonian rheology of ice that we employ in our models. Non-Newtonian rheology that is dependent on the grain size would require a different model for calculating the tidal dissipation [*Barr and Showman*, 2009]. However, uncertainties in the parameters describing the ice-rheology (e.g., grain size) would only complicate the current models and hence, the grain-size dependence of ice-viscosity is not included in our models.

Studies that have included orbital coupling with Io and Ganymede suggest that the oscillatory behavior of Io could change the orbital parameters of Europa. This would affect the magnitude of tidal dissipation generated over time within Europa and has been suggested to result in oscillations in shell thickness over time [*Hussmann and Spohn*, 2004]. Tidal dissipation is also expected to vary laterally across the ice-shell [*Tobie et al.*, 2005; *Mitri and Showman*, 2008]. Our numerical experiments in Case C that include viscosity-dependent tidal heating-rate lead to different magnitudes of heating-rate in different regions within the shell. Therefore, as the ice-viscosity structure changes over time, so does the magnitude of heating-rate in the ice. We impose a peak tidal heating rate value (q_{max}) and do not explicitly account for time varying component of tidal dissipation in a manner similar to coupled orbital-thermal models [*Showman and Han*, 2010; 2011]. Nevertheless, the models demonstrate that in a simple ice-ocean system, the

shell growth rate significantly increases with reconfiguration of ice-shell convection pattern and the addition of an appropriate (if the heating-rate is very small, it behaves similar to control Case A) tidal heating-rate prevents the system from freezing.

In the control case that does not include any heating, we note that as the ice-shell thickens, the convection cells remain thin and do not considerably increase in width leading up to the freeze-over. In contrast, in cases that include heating rate in ice, and hence achieve an equilibrium shell-thickness, the convection cells remain much wider as the growth rate increases. In the control case, the ice-convection cells remain thin, likely due to the rapid thickening of the ice-shell in absence of heat sources; thus the shell freezes faster than the convection pattern can reconfigure completely.

Similar numerical experiments in ice-shells with lower and higher temperature-dependence of ice-viscosity were performed to validate our results. We find that in agreement with the results presented here, there is a sudden and significant increase in shell growth rate when the ice-convection planform changes. Higher numerical grid-resolution calculations of the cases also confirm our results.

Finally, our experiments assume that Europa initially started warm and subsequently cooled, and our conclusions are dependent on that assumption. This is simply one end-member possibility, and one can envision the opposite scenario in which the system started out completely frozen and subsequently melted.

4.7 Conclusions

We performed numerical experiments on a two-phase ice-ocean system to investigate how convection patterns evolve as the system cools and how the changing convective planform affects growth of the ice shell. We perform a control case with no heat sources,

a case with uniform tidal heating rate, and several cases with viscosity-dependent tidal heating rate. In all cases we find:

[1] The ice-shell growth rate increases when the convective planform within the shell changes, increasing the average width of convection cells. In particular, we find a sudden and dramatic increase in ice-shell growth rate upon the merging of convection cells. After convection cells merge, the timescale for ice-shell growth exceeds the timescale for further changes in convective planform. Once the shell reaches an equilibrium thickness, the convective planform changes again, significantly increasing the aspect ratio of convection cells.

[2] The change in the convective planform of a growing ice-shell differs greatly from an ice-shell at equilibrium. In a growing shell, the ice-convection cells remain narrow in width due to the rapid thickening of the shell. Whereas, in an ice-shell at equilibrium, the convection cells have sufficient time to reconfigure their pattern, and thus have a larger aspect ratio. This could have potential implications for formation of surface features over time.

[3] Tidal heating in the ice may prevent the ice-ocean system from completely freezing over, depending on the magnitude of the tidal heating-rate. The ice-shell eventually attains a fixed thickness. This is likely because the tidal heating-rate in the ice balances the heat loss via conduction and convection in the ice-shell, causing the system to reach a thermal equilibrium.

[4] Localization of tidal heating rate as a function of ice-viscosity affects the equilibrium thickness of the ice-shell. When the maximum heating-rate is localized in the ice underneath the viscous lid, the equilibrium thickness of the shell is greater than in cases

where the heating-rate is localized in the middle and lower parts of the shell. When maximum tidal heating rate is localized towards the base of the growing ice-shell, the shell remains relatively thin in comparison with the other two cases. The intermediate case, where the tidal heating is localized in the middle of the shell, results in an ice-shell with an intermediate thickness when the system reaches an equilibrium state. This probably occurs due to the larger band of relevant ice-viscosities near base of the shell resulting in a higher tidal heating rate compared to the other two cases. A larger heating in the ice slows down the freezing and results in a thinner ice-shell. In the case where maximum heating is concentrated in the upper part of the shell, the heat is expected to be efficiently conducted away to the surface without significantly affecting the freezing of ice at the interface. The thickness of the near-surface ice where the heating rate is localized is also small. This would also reduce the total amount of heat localized in this case, and hence a thicker ice-shell.

References

Allu Peddinti, D., & McNamara, A. K. (2015). Material transport across Europa's ice shell. *Geophys. Res. Lett*., *42*, 4288-4293.

Anderson, J. D., Lau, E. L., Sjogren, W. l., Schubert, G., & Moore, W. B. (1998). Europa's differentiated internal structure: inferences from two Galileo encounters. *Nature, 276*, 1236-1239.

Barr, A. C., & McKinnon, W. B. (2007). Convection in ice I shells and mantles with self-consistent grain size. *J. Geophys. Res*., *112*, E02012, 10.1029/2006JE002781.

Barr, A. C., & Pappalardo, R. T. (2005). Onset of convection in the icy Galilean satellites: influence of rheology. *J. Geophys., Res. 110*, E12005, 10.1029/2004JE002371.

Billings, S. E., & Kattenhorn, S. A. (2005). The great thickness debate: ice shell thickness models for Europa and comparisons with estimates based on flexure at ridges. *Icarus*, *177*, 397-412.

Carr, M. H., Belton, M. J. S., Chapman, C. R., Davies, M. E., Geissler, P., Greenberg, R., McEwen, A. S., Tufts, B. R., Greeley, R., Sullivan, R., Head, J. W., Pappalardo, R. T., Klaasen, K. P., Johnson, T. V., Kaufman, J., Senske, D., Moore, J., Neukum, G., Schubert, G., Burns, J. A., Thomas, & P., Veverka, J. (1998). Evidence for a subsurface ocean on Europa. *Nature, 391*, 363-365.

Cassen, P., Reynolds, R. T., & Peale, S. J. (1979). Is there liquid water on Europa? *Geophys. Res. Lett., 6*, 731-734.

Crameri, F. P., Tackley, P. J., Meilick, I., Gerya, T. V., & Kaus, B. J. P. (2012). A free plate surface and weak oceanic crust produce single-sided subduction on Earth. *Geophys. Res. Lett., 39*, L03306, 10.1029/2011G1050046.

Deschamps, F., & Sotin, C. (2001). Thermal convection in the outer shell of large satellites. *J. Geophys. Res., 106*, 5107-5121.

Dunaeva, A. N., Antsyshkin, D. V., & Kuskov, O. L. (2010). Phase diagram of H_2O: thermodynamic functions of the phase transitions of high-pressure ices. *Solar Sys. Res., 44,* 202-222.

Durham, W. B., Prieto-Ballesteros, O., Goldsby, D. L., & Kargel, J. S. (2010). Rheological and thermal properties of icy materials. *Space Sci. Rev., 153,* 273-298.

Freeman, J., Moresi, L., & May, D. A. (2006). Thermal convection with a water ice I rheology: Implications for icy satellite evolution. *Icarus, 180,* 251-264.

Goldsby, D. L., & Kohlstedt, D. L. (2001). Superplastic deformation in ice: experimental observations. *J. Geophys. Res., 106,* 11017-11030.

Greeley, R., Sullivan, R., Klemaszewski, J., Homan, K., Head, J. W., Pappalardo, R. T., Veverka, J., Clark, B. E., Johnson, T. V., Klassen, K. P., Belton, M., Moore, J., Asphaug, E., Carr, M. H., Neukam, G., Denk. T., Chapman, C. R., Pilcher, C. B., Geissler, P., Greenberg, R., & Tufts, R. (1998). Europa: Initial Galileo geological observations. *Icarus, 135,* 4-24.

Greenberg, R., Geissler, P., Hoppa, G., Tufts, B. R., Durda, D. D., Pappalardo, R., Head, J. W., Greeley, R., Sullivan, R., & Carr, M. H. (1998). Tectonic processes on Europa: tidal stresses, mechanical response, and visible features. *Icarus, 135,* 64-78.

Greenberg, R., Geissler, P., Tufts, B. R., & Hoppa, G. V. (2000). Habitability of Europa's crust: the role of tidal-tectonic processes. *J. Geophys. Res., 105,* 17551-17562.

Han, L., & Showman, A. P. (2011). Coupled convection and tidal dissipation in Europa's ice shell using non-Newtonian grain-size-sensitive (GSS) creep rheology. *Icarus, 212,* 262-267.

Hoppa, G. V., Tufts, B. R., Greenberg, R., & Geissler, P. E. (1999a). Formation of cycloidal features on Europa. *Science, 285,* 1899-1902.

Hussmann, H., & Spohn, T. (2004). Thermal-orbital evolution of Io and Europa. *Icarus, 171*, 391-410.

Hussmann, H., Spohn, T., & Wieczerkowski, K. (2002). Thermal equilibrium states of Europa's ice shell: implications for internal ocean thickness and surface heat flow. *Icarus, 156*, 143-151.

Khurana, K. K., Kivelson, M. G., Stevenson, D. J., Schubert, G., Russell, C. T., Walker, R. J., & Polanskey, C. (1998). Induced magnetic fields as evidence for subsurface oceans in Europa and Callisto. *Nature, 395*, 777-780.

Kivelson, M. G., Khurana, K. K., Joy, S., Russell, C. T., Southwood, D. J., Walker, R. J., & Polanskey, C. (1997). Europa's magnetic signature: report from Galileo's pass on 19 December 1996. *Science, 276*, 1239-1241.

Li, M., & McNamara, A. K. (2013). The difficulty for subducted oceanic crust to accumulate in upwelling mantle plume regions. *J. Geophys. Res., 118*, 1-10.

Li, M., McNamara, A. K., & Garnero, E. J. (2014). Chemical complexity of hotspots caused by cyclic oceanic crust through mantle reservoirs. *Nature Geoscience, 7*, 336-370.

McCord, T. B., Hansen, G. B., Fanale, F. P., Carlson, R. W., Matson, D. L., Johnson, T. V., Smythe, W. D., Crowley, J. K., Martin, P. D., Ocampo, A., Hibbitts, C. A., Granahan, J. C., and the NIMS team. (1998). Salts on Europa's surface detected by Galileo's near infrared mapping spectrometer. *Science, 280*, 1242-1245.

McKinnon, W. B. (1999). Convective instability in Europa's floating ice shell. *Geophys. Res. Lett., 7*, 951-954.

McNamara, A. K., Garnero, & E. J., Rost, S. (2010). Tracking deep mantle reservoirs with ultra-low velocity zones. *Earth Planet. Sci. Lett., 299*, 1-9.

Mitri, G., & Showman, A. P. (2005). Convective-conductive transitions and sensitivity of a convecting ice shell to perturbations in heat flux and tidal-heating rate: implications for Europa. *Icarus, 177*, 447-460.

Moresi, L., & Gurnis, M. (1996). Constraints on the lateral strength of slabs from three-dimensional dynamic flow models. *Earth Planet. Sci. Lett., 138,* 15-28.

Nimmo, F., & Gaidos, E. (2002). Strike-slip motion and double ridge formation on Europa. *J. Geophys. Res., 107,* 10.1029/2000JE001476.

Nimmo, F., Giese, B., & Pappalardo, R. T. (2003). Estimates of Europa's ice shell thickness from elastically-supported topography. *Geophys. Res. Lett., 20,* 10.1029/2002GL016660, 1233.

Nimmo, F., & Manga, M. (2009). Geodynamics of Europa's Icy Shell. *Europa,* edited by Pappalardo, R. T., McKinnon, W. B., & Khurana, K. K. Tucson: University of Arizona Press, pp 381-400.

Nimmo, F., Prockter, L., & Schenk, P. (2005). Europa's icy shell: past and present state, and future exploration. *Icarus, 177,* 293-296.

O'Brien, D. P., Geissler, P., & Greenberg, R. (2002). A melt-through model for chaos formation on Europa. *Icarus, 156,* 152–161.

Ojakangas, G. W., & Stevenson, D. J. (1989). Thermal state of an ice shell on Europa. *Icarus, 81,* 220-241.

Pappalardo, R. T., et al. (1999). Does Europa have a subsurface ocean? Evaluation of the geological evidence. *J. Geophys. Res., 104*(E10), 24015-24055.

Pappalardo, R. T., Head, J. W., Greeley, R., Sullivan, R. J., Pilcher, C., Schubert, G., Moore, W. B., Carr, M. H., Moore, J. M., Belton, M. J. S., & Goldsby, D. L. (1998). Geological evidence for solid-state convection in Europa's ice shell. *Nature, 291,* 365-368.

Rathbun, J., Musser Jr, G. S., & Squyres, S. W. (1998). Ice diapirs on Europa: implications for liquid water. *Geophys. Res. Lett., 25,* 4157-4160.

Ruiz, J., & Fairen, A. G. (2005). Seas under ice: stability of liquid-water oceans within icy worlds. *Earth, Moon, and Planets, 97*, 79-90.

Schenk, P. M. (2002). Thickness constraints on the icy shells of the Galilean satellites from a comparison of crater shapes. *Nature, 417*, 419-421.

Showman, A. P., & Han, L. (2004). Numerical simulations of convection in Europa's ice shell: implications for surface features. *J. Geophys. Res., 109*, E01010.

Sotin, C., Choblet, G., Head, J. W., Mocquet, A., & Tobie, G. (2004). Thermal evolution of Europa's icy crust. In: *Workshop on Europa's Icy Shell: Past, Present, and Future*, LPI Contribution No. 1195. Lunar and Planetary Institute, Houston, pp. 84-85.

Sotin, C., Head III, J. W., & Tobie, G. (2002). Europa: tidal heating of upwelling thermal plumes and the origin of lenticulae and chaos melting. *Geophys. Res. Lett., 29*, 10.1029/2001GL013884.

Spencer, J. R., Tamppari, L. K., Martin, T. Z., & Travis, L. D. (1999). Temperatures on Europa from Galileo Photopolarimeter-radiometer: nighttime thermal anomalies. *Science*, *284*, 1514-1516.

Spohn, T., & Schubert, G. (2003). Oceans in the icy Galilean satellites of Jupiter? *Icarus, 161*, 456-467.

Stengel, K. C., Oliver, D. S., & Booker, J. R. (1982). Onset of convection in a variable-viscosity fluid. *J. Fluid Mech., 120*, 411-431.

Sullivan, R., Greeley, R., Homan, K., Klemaszewski, J., Belton, M. J. S., Carr, M. H., Chapman, C. R., Tufts, R., Head III, J. W., Pappalardo, R., Moore, J., Thomas, P., & the Galileo Imaging Team. (1998). Episodic plate separation and fracture infill on the surface of Europa. *Nature, 391*, 371-373.

Tackley, P. J., & King, S. D. (2003). Testing the tracer ratio method for modeling active compositional fields in mantle convection simulations. *Geochemistry Geophysics Geosystems*, *4*(4), 8302, doi:10.1029/2001gc000214.

Takeushi, H., & Saito, M. (1972). Seismic surface waves. In *Methods in Computational Physics*, Vol. 1, edited by Bolt, B. A., pp. 217-295. New York: Academic.

Tobie, G., Mocquet, A., & Sotin, C. (2005). Tidal dissipation within large icy satellites: applications to Europa and Titan. *Icarus*, *177*, 534-549.

Turtle, E. P., & Pierazzo, E. (2001). Thickness of an Europan ice shell from impact crater simulations. *Science, 294*, 1326-1328.

Warren, S. G., Brandt, R. E., Grenfell, T. C., & McKay, C. P. (2002). Snowball Earth: Ice thickness on the tropical ocean. *J. Geophys. Res., 107* (C10), 3167, 10.1029/2001JC001123.

Zahnle, K., Schenk, P., Levison, H., & Dones, L. (2003). Cratering rates in the outer solar system. *Icarus, 163*, 263-289.

Zolotov, M. Y., & Kargel, J. S. (2009). On the chemical composition of Europa's icy shell, ocean, and underlying rocks. *Europa*, edited by Pappalardo, R. T., McKinnon, W. B., & Khurana, K. K. Tucson: University of Arizona Press, pp 431-451.

CHAPTER 5

INCORPORATION OF HETEROGENEITY IN A FORMING ICE-SHELL

5.1 Abstract

The presence of various chemical species on the surface of the icy moon Europa is evidenced by the visible "ruddy streaks" as well as by the spectral analysis of its surface. It is hypothesized that these impurities are likely endogenic and sample the possible chemical composition of the subsurface ocean. Conversely, the surface impurities could enter the ice-shell and create compositional heterogeneity within it. Additionally, an ice-shell formed by cooling of a salty ocean may also trap salts within the shell by rapid freezing. In the two-phase system, as the ice-shell forms from a cooling ocean, tracers representing impurities are mapped across the shell. We investigate the spatial and temporal pattern of entrapment of these tracers within the ice-shell, which may be used to infer the formation of heterogeneities in the ice-shell similar to brine inclusions in terrestrial sea ice.

5.2 Introduction

The surface of Europa is sparsely cratered and mostly smooth on a large scale, which has been inferred to indicate a young (< 100 Myr) surface age [*Zahnle et al.*, 2003]. The young surface also suggests that it underwent recent or current geological activity. High resolution imaging revealed a deformed surface characterized by features such as ridges, bands, domes, and chaos terrain (regions of apparent partial melting) [*Greeley et al.*, 1998]. The high albedo of the surface is indicative of pure water ice [*McCord et al.*, 1998]; however spectral analysis (both IR and UV) as well as visible imaging shows the presence of non-ice material across the surface. Of geophysical and geochemical interest

is the high concentration of the non-ice material along morphological features such as ridges and troughs. This alignment has often been interpreted as suggestive of endogenic origin of the material. Europa has a global H_2O layer (~ 80-170 km thick) [*Anderson et al.*, 1998; *Billings and Kattenhorn*, 2005] that consists of a subsurface ocean [*Khurana et al.*, 1998; *Kivelson et al.*, 1997; *Pappalardo et al.*, 1999] underneath an ice-shell. Thus, endogenic origin of surface species suggests transport of material from the ocean to the surface via the ice-shell [e.g., *McCord et al.*, 1998; *Sotin et al.*, 2003; *Carlson et al.*, 2005; *Allu Peddinti and McNamara*, 2015]. It also suggests that material from the surface could be transported to the ocean across the ice-shell. It has been hypothesized that surface material can be trapped into the ice-shell as brine pockets similar to the brine inclusions in terrestrial sea ice [*Head and Pappalardo*, 1999]. The study of terrestrial sea ice formation has revealed the presence of brine pockets and gas inclusions formed by rapid freezing and trapping within the sea ice. The sea ice, thus consists of pure water ice with brine inclusions and gas pockets that are constantly mobilizing within the ice and across the ice-water interface [*Reeburgh*, 1984; *Golden et al*., 1998]. The propagation of these brine pockets in the form of brine channels and networks depends on the temperature gradient [*Shreve*, 1967], the growth rate of ice [*Wakatsuchi and Ono*, 1983; *Reeburgh*, 1984], the age of the ice and salinity gradient [*Golden et al.*, 1998; *Light et al*., 2003].

While surface impurities provide one possible source of compositional heterogeneity in the ice-shell, initial salinity of the ocean may also contribute to formation of compositional heterogeneity in the shell as it grows by freezing. Slow freezing of ice leads to rejection of brines which leads to pure ice crystals; however rapid

freezing can trap them in the form of compositional heterogeneity within the ice. These heterogeneities are mobile and decrease in density over time as a result of brine drainage [*Eide and Martin*, 1975] and inclusion migration [*Zolotov et al*., 2004]. It has been suggested that similar processes can lead to the formation of brine inclusions in Europa's ice-shell [*Zolotov and Kargel*, 2009], which could be responsible for creating compositional buoyancy [*Pappalardo and Barr*, 2004] and the formation of surface features such as the chaos terrain [*Head and Pappalardo*, 1999; *Collins et al*., 2000]. The brine pockets are also sites within the ice that are habitable for micro-organisms such as algae [*Reeburgh*, 1984] and hence the presence of salty impurities in the Europan ice-shell is of astrobiological interest.

It has been proposed that captured solutes from the ocean are mostly trapped in the uppermost regions of a thickening ice-shell, and that brine inclusions are only stable in the lower portions of a non-convecting shell [*Zolotov and Kargel*, 2009]. It has been shown, however, that newly formed ice that could potentially capture oceanic salts can be convectively transported and circulated across the ice-shell [*Allu Peddinti and McNamara*, 2015]. In this study, we use colored tracers to represent impurities and map their movement across the growing ice-shell. The spatial distribution of heterogeneities thus formed, can provide insight into the mobility of heterogeneities in the ice-shell with time.

5.3 Hypothesis

We hypothesize that in a thickening ice-shell, non-water-ice impurities that enter the ice-shell will be spatially distributed and potentially trapped within the shell as a function of time as described by Zolotov and Kargel, 2009. We expect some of the impurities to be

trapped in the high-viscosity lid while some could be deposited in different regions within the shell via convective circulation. Depending on the time of entry, we expect that only the impurities that enter early, would be trapped in the viscous lid unless the thickness of the viscous lid increases with time. As the ice-shell thickness increases and the ice-convection plan-form changes, impurities introduced at different times would be trapped in either the lid or the ice-convection cells. We designate ice tracers of different colors to represent impurities entering the ice-shell at different times. Therefore, we do not attach any chemical composition to the impurities and the colored ice-tracers act as *passive* tracers within the ice-shell. We define the deposition of these colored ice-tracers within the shell as a potential heterogeneity. A spatiotemporal pattern of heterogeneities could thus reveal their mobility within the ice-shell over time as well their drainage into the ocean below (destruction of heterogeneity).

Heterogeneities in the ice-shell have been speculated to form either during the formation of the ice-shell from a freezing saline ocean and/or by the entrapment of surface impurities that may enter the ice-shell via tectonic/ tidal cracking/ craters [*Zolotov and Kargel,* 2009]. In our models, since we only map the distribution of impurities that already entered the shell, we consider either possible sources by introducing the tracers at different depths. Therefore impurities near the base of the shell could represent the heterogeneities formed by rapid salt water freezing (e. g. via capture of brines into ice defects). Few impurities closer to the top of the shell could potentially represent surface material that may enter the shell.

5.4 Modeling Method

We perform thermochemical convection calculations in order to test the hypothesis of depth-time-wise distribution of heterogeneities in a growing ice-shell. We adapt the two-dimensional mantle convection code, Citcom [*Moresi and Gurnis*, 1996; *McNamara et al*., 2010; *Allu Peddinti and McNamara*, 2015] modified to advect thermochemical tracers in order to solve the dimensionless, incompressible equations for conservation of mass, momentum and energy.

$$\left.\begin{aligned} &\text{Conservation of mass: } \nabla \cdot \vec{u} = 0 \\ &\text{Conservation of momentum: } -\nabla P + \nabla \cdot \left(\eta \dot{\varepsilon}\right) = Ra\left(T - BC\right) \\ &\text{Conservation of energy: } \frac{\partial T}{\partial t} + \left(\vec{u} \cdot \nabla\right)T = \nabla^2 T \end{aligned}\right\} \quad 5.1$$

where $\vec{u}$ is velocity, P is the dynamic pressure, η is the dynamic viscosity, $\dot{\varepsilon}$ is the strain rate, T is the temperature, C is the composition (C = 1 for water; C = 0 for ice), and t is the time. Ra and B are two non-dimensional parameters that control the vigor of convection and are defined as follows.

$$\text{The thermal Rayleigh number, } Ra = \frac{\alpha \rho g \Delta T h^3}{\kappa \eta_m} \quad 5.2$$

where α is the thermal expansivity, ρ is the density, κ is the thermal diffusivity, and η_m is the melting viscosity of ice; g is the acceleration due to gravity and h is the thickness of the system. All material parameters are listed in Table 5.1. ΔT is a constant related to temperature (which for convenience is usually identical to the temperature difference across the system).

The intrinsic density is represented by the buoyancy ratio, B as:

$$B = \frac{\Delta\rho}{\rho\alpha\Delta T} \qquad 5.3$$

where $\Delta\rho$ is a constant representing the density contrast between liquid water and solid ice at reference T ~ 273.15 K and P ~ 1 bar, ρ and α are material properties of ice as listed in table 5.1 and ΔT is a non-dimensional constant related to temperature (consistent with the temperature difference between top and bottom of the system).

Table 5.1

Material Parameters Used in the Numerical Models

Parameter	**Value**
Gravitational acceleration (g)	1.3 ms^{-2}
Thickness (h)	100 km
Temperature at the surface (T_s)	95 K
Melting temperature of ice (T_m)	Function of pressure (~273.15 K)
Melting viscosity of ice (η_m)	10^{16} Pa-s
Density of ice (ρ_i)	917 kgm^{-3}
Density of water (ρ_w)	1000 kgm^{-3}
Thermal expansivity of ice (α_i)	1.6 x 10^{-4} K^{-1}
Thermal diffusivity of ice (κ_i)	1.0 x 10^{-6} m^2s^{-1}

We employ a proxy fluid for the ocean layer that is 100 times less viscous than the lowest viscosity ice (Appendix A). This approximation sufficiently decouples the convection in the ice and ocean layers similar to what we expect in the real system without compromising on the computational efficiency of our numerical models [*Allu Peddinti and McNamara*, 2015]. Using a more realistic fluid velocity (i.e. lower velocity) is not expected to significantly affect our results of the current study.

Initial and boundary conditions

The governing fluid dynamics equations in 5.1 are solved in a two-dimensional Cartesian geometry. The system begins from a warm initial ocean at non-dimensional

temperature, $T = 1.0$. The temperature at the surface is isothermal and set to $T = 0.0$. There is no heat flow at the bottom boundary of the model. The velocity boundary conditions at all boundaries of the domain are free slip.

The initial test cases with a layer of passive tracers begin with a warm initial layer overlain by this layer of color-marked tracers. We use the ratio tracer method [e.g., *Tackley and King,* 2003] with compositional tracers for ice and water. The tracer species for the impurities are merely color-marked ice tracers and we do not incorporate any other chemical/ compositional species in this numerical study. The aspect ratio of the model domain varies from 6 for the initial test cases to 3 for the main cases.

Formation of Heterogeneity

We color ice-tracers to represent impurities that are introduced into the ice-shell. These tracers are placed at different depths at different times in the shell. They are grouped together as small spheres (of a pre-defined radius) and are placed at a regular distance from each other. We can therefore change the size and horizontal spacing of the spheres as well as their depth or vertical spacing within the ice-shell. This provides a method of testing a wide range of sizes of heterogeneity formation as well as to consider both the rapid freezing and surface entrapment origin of compositional heterogeneity in ice. The aim of our experiments is simply to introduce these spheres into the ice-shell at different times and depths and notice their spatial distribution as it evolves over time. We refer to their deposition within the ice-shell as potential heterogeneity in the shell.

5.5 Results and Discussion

[1] Initial tests were performed with a thin layer of passive tracers (colored ice tracers) representing potential impurities placed at the surface, and letting the ice-shell form from

a cooling ocean. This allowed us to broadly examine the distribution of surface material in the convection cells as the ice-shell grows from the ocean. The system initially consists of a warm ocean that cools quickly to form a thin ice-shell at the top. Figure 5.1 shows a very early snapshot (~ 0.15 million years) from this test case and captures the initial condition of the model. The panels from top to bottom show the tracer species, the logarithm of viscosity, the phase composition and the temperature respectively. A layer of passive tracers is placed at the top of the ice-shell as shown in the species panel. As the ice-shell thickens, the convection planform changes with time, resulting in distribution of these passive tracers across the ice-shell via convective currents. This is illustrated in figure 5.2 which shows the upper 60 kilometers of isolated panels of tracer species and temperature at three later times. In the earliest snapshot (~ 0.42 million years), the ice-shell convection pattern is reconfiguring as evidenced by the merging convection cells in the temperature panel. The passive tracers are now being mobilized by the evolving ice-convection cells. At a later time (~ 1 million years), convection pattern in ice continues to change as indicated by unstable convection cells in the middle and left half of the temperature panel. The tracer species are pushed along the downwelling ice as they are circulated along the convection cells. At an even later time (~ 1.65 million years), there is an increase in the width and height of ice-convection cells as the convection pattern keeps reconfiguring in the thickening shell. The tracers representing impurities are concentrated in the downwelling regions of ice-convection cells. Thus, we see the distribution of the surface impurities within the convecting ice-shell as they are mobilized by the convective flow. This particular experiment, however, does not develop a thick stagnant lid at the top of the shell, which prevents material from being frozen into the high-viscosity ice-lid.

Hence, we performed the next set of experiments with small tracer spheres representing impurities, and map their distribution over time.

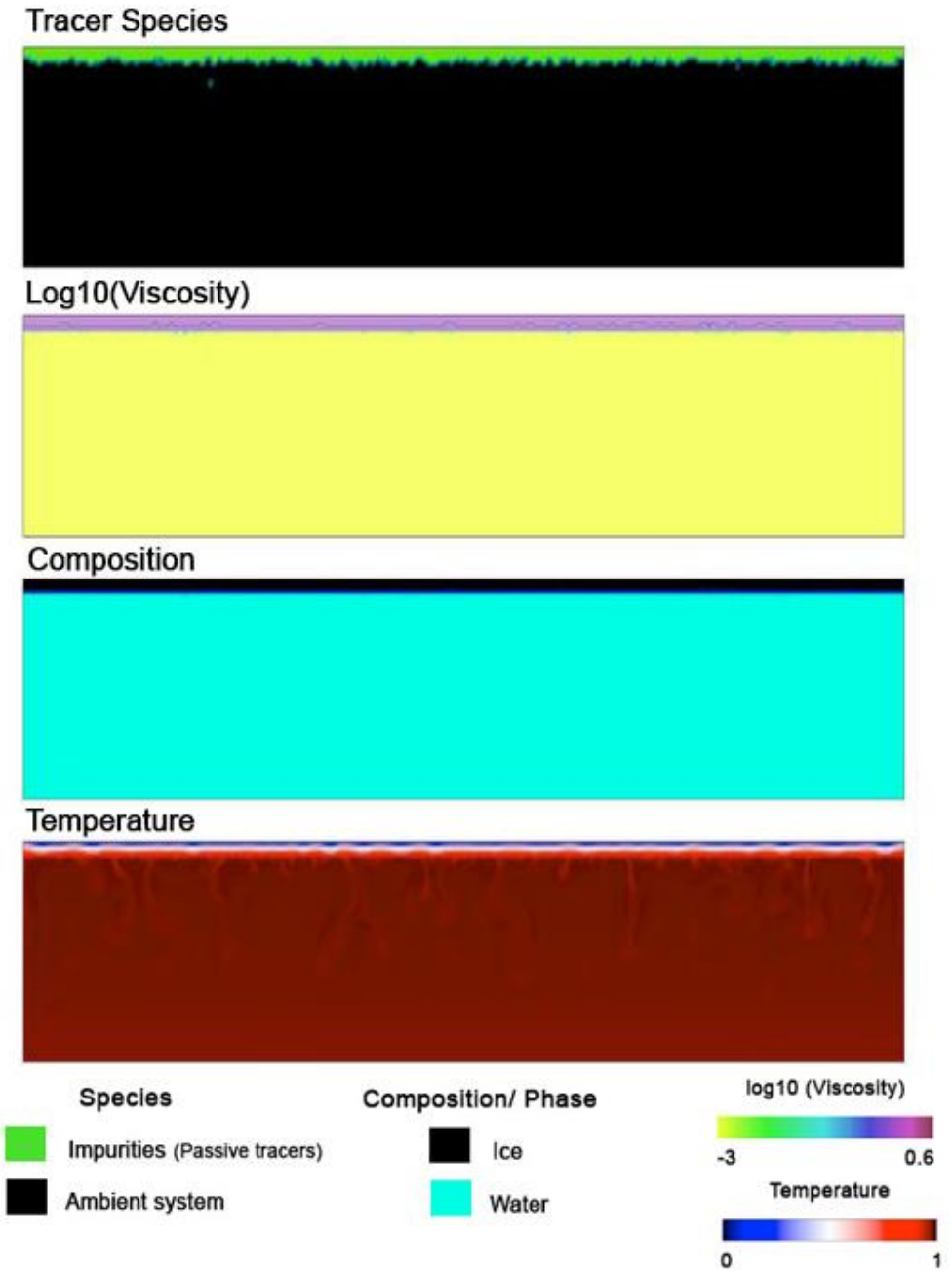

Figure 5.1. Passive tracers in ice-ocean system: Early snapshot. The top panel shows the tracer species with green color indicating impurities. The three panels below it show the logarithm of viscosity (yellow: low; purple: high), composition (light blue: water; black: ice), and temperature (blue: cold; red: hot) respectively.

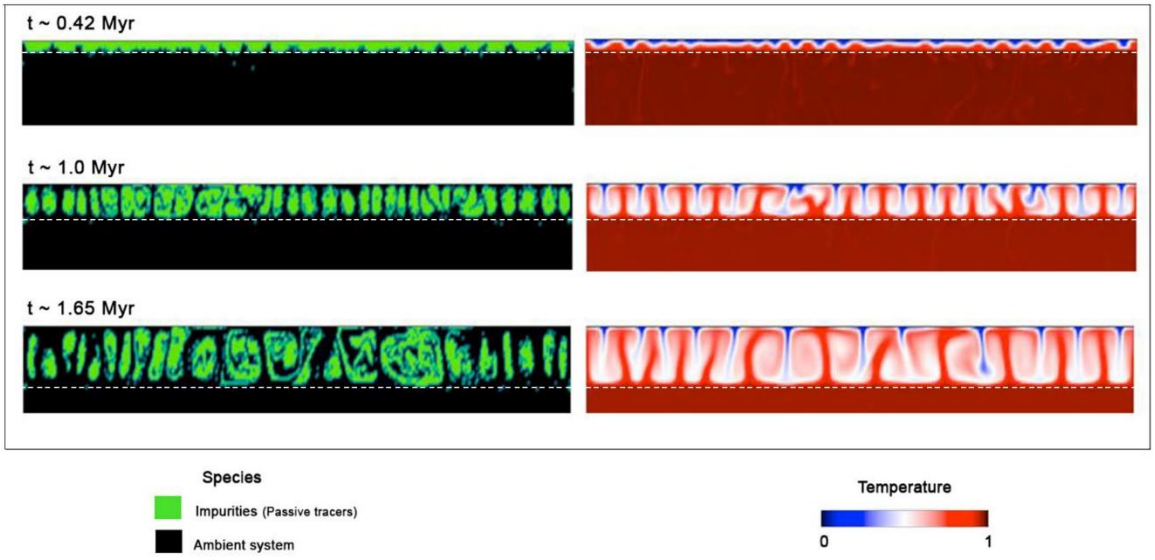

Figure 5.2. Distribution of passive tracers in ice-ocean system. The upper 60 km of the tracer species panel on the left, with green color indicating impurities; and the temperature (blue: cold; red: hot) panel on the right at three different times (0.42, 1.0 and 1.65 Myr since initiation, from top to bottom). The white dashed line represents the ice-ocean boundary.

[2] The size of the tracer spheres and their depth within the shell is expected to influence their deposition within the shell. Small tracer spheres near the top of the shell are expected to stay frozen into the high-viscosity ice-lid that forms atop the shell in all our models. Figures 5.3 and 5.4 shows snapshots from a case A (with zero heating) that tests this hypothesis. In each snapshot, the panels from top to bottom display the logarithm of viscosity, the composition, temperature, and the tracer species. The first snapshot 5.3 (A) shows the ice-ocean system at an early time (~ 0.64 million years) with the initial placement of the tracer spheres, as seen in the species panel. The spheres are placed at ~ 6 km depth from the top, about 20 km apart from each other. At a later time (~ 8.13 million years), in snapshot 5.3 (B), another set of tracer spheres are introduced in the ice-shell at a slightly greater depth, below the previous layer of spheres. The ice-shell convection is

changing its configuration at this time, indicated by the undulating contours in the temperature and viscosity panels. The high viscosities atop the shell indicate the stagnant ice-lid where the first set of tracers remain frozen. At an even later time (~ 9.64 million years), the ice-shell convection patterns have changed further, as seen in the temperature panel of the snapshot labeled (C) in figure 5.4. Another set of tracers has been introduced into the ice-shell below the previous two sets of spheres, as seen in the tracer species panel. These spheres are beginning to be mobilized by the ice-convection flow as indicated by their slight displacement in the species panel. The second set of spheres appear to remain stationary. In snapshot (D) of figure 5.4 (~ 14.76 million years), the ice-shell has thickened further and the liquid layer remains relatively thin. The ice-shell convection pattern still continues to reconfigure. The third set of tracers are circulated along the ice-convection cells in the downwelling regions. The second set of spheres also begin to be mobilized as shown by their displacement in the tracer species panel. The first set of tracer spheres, however, remain frozen in the high-viscosity ice-lid.

Due to the absence of any heat sources in this case, the system eventually freezes over. The successive generations of tracer spheres, thus remain either trapped in the ice-lid or get distributed across the ice-shell via ice-convection depending upon the time and depth at which they enter the ice-shell, as shown in the time snapshot in figure 5.5.

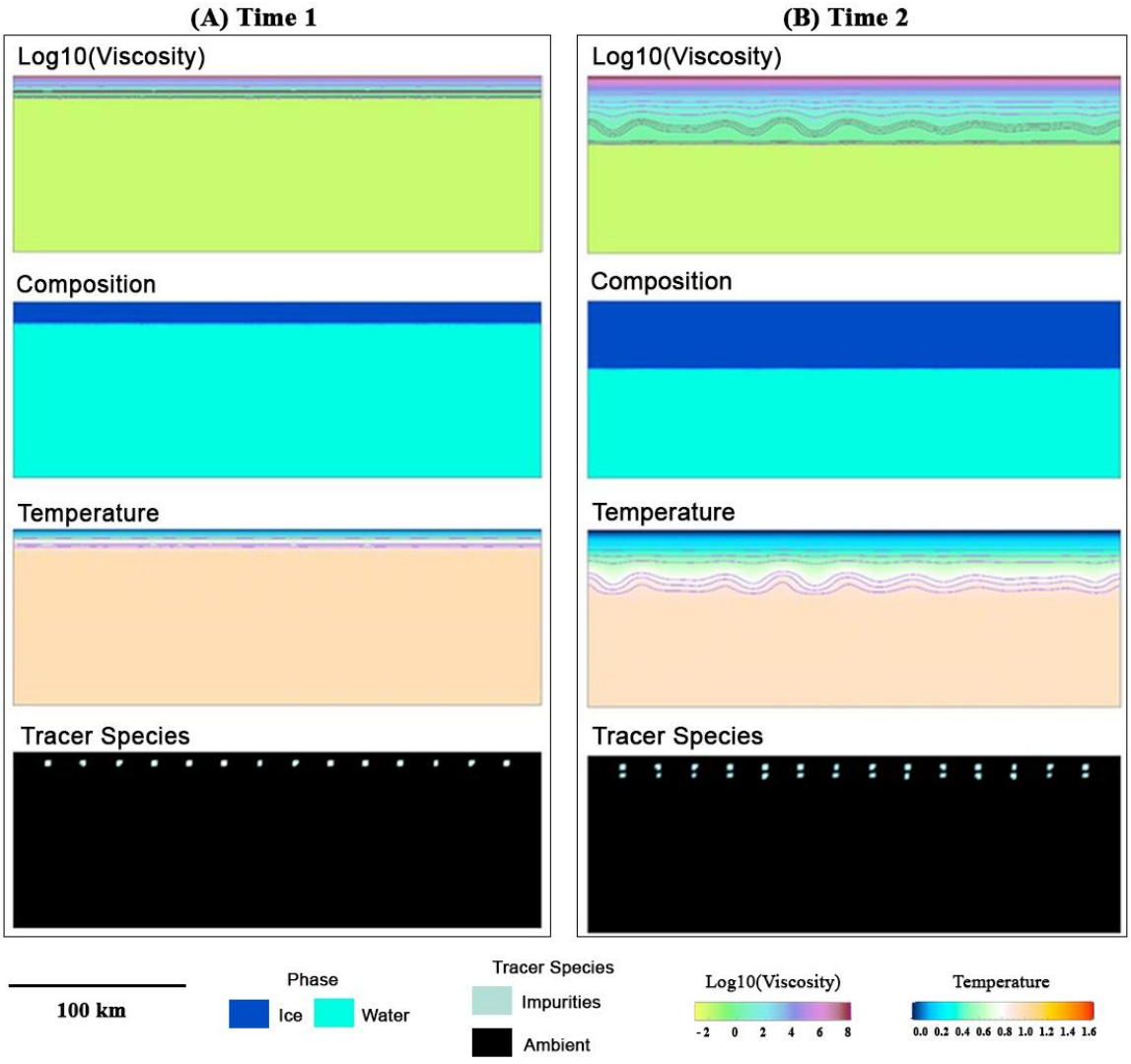

Figure 5.3. Time Snapshots from Case A. (A) 0.64 Myr; (B) 8.13 Myr from the beginning of the calculation. The top panel displays the logarithm of viscosity (yellow: low; purple: high) with the contours outlining each order of magnitude increase in viscosity. The second panel shows the composition (phase) where deep blue represents ice and the light blue represents the proxy fluid (the liquid ocean). The panel below it displays the temperature. The bottom panel shows the tracer species representing impurities in ice in whitish-green color, with black indicating ambient system.

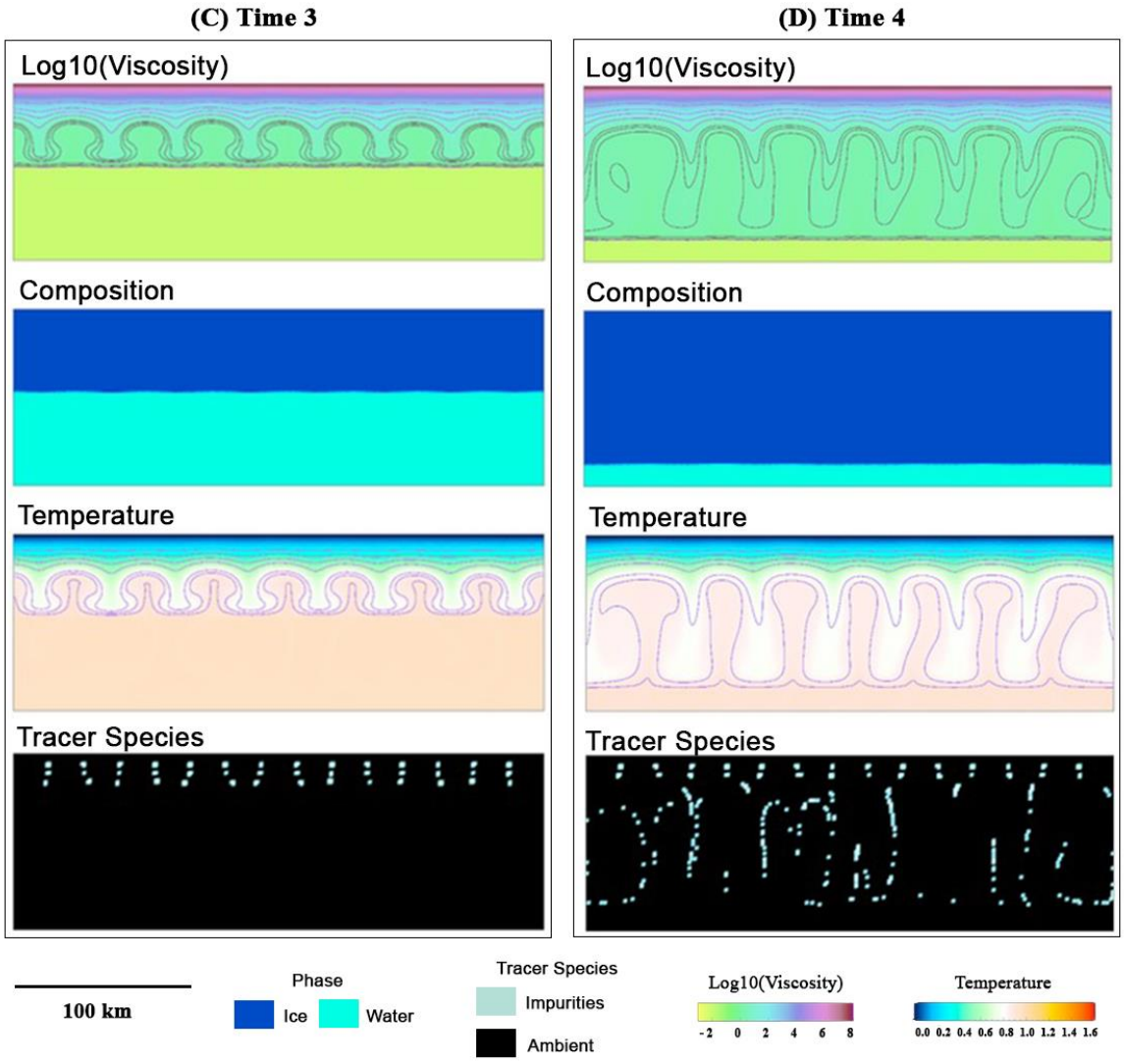

Figure 5.4. Time Snapshots from Case A. (C) 9.64 Myr; (D) 14.76 Myr since the beginning of the calculation. The top panel displays the logarithm of viscosity (yellow: low; purple: high) with the contours outlining each order of magnitude increase in viscosity. The second panel shows the composition (phase) where deep blue represents ice and the light blue represents the proxy fluid (the liquid ocean). The panel below it displays the temperature. The bottom panel shows the tracer species representing impurities in ice in whitish-green color, with black indicating ambient system.

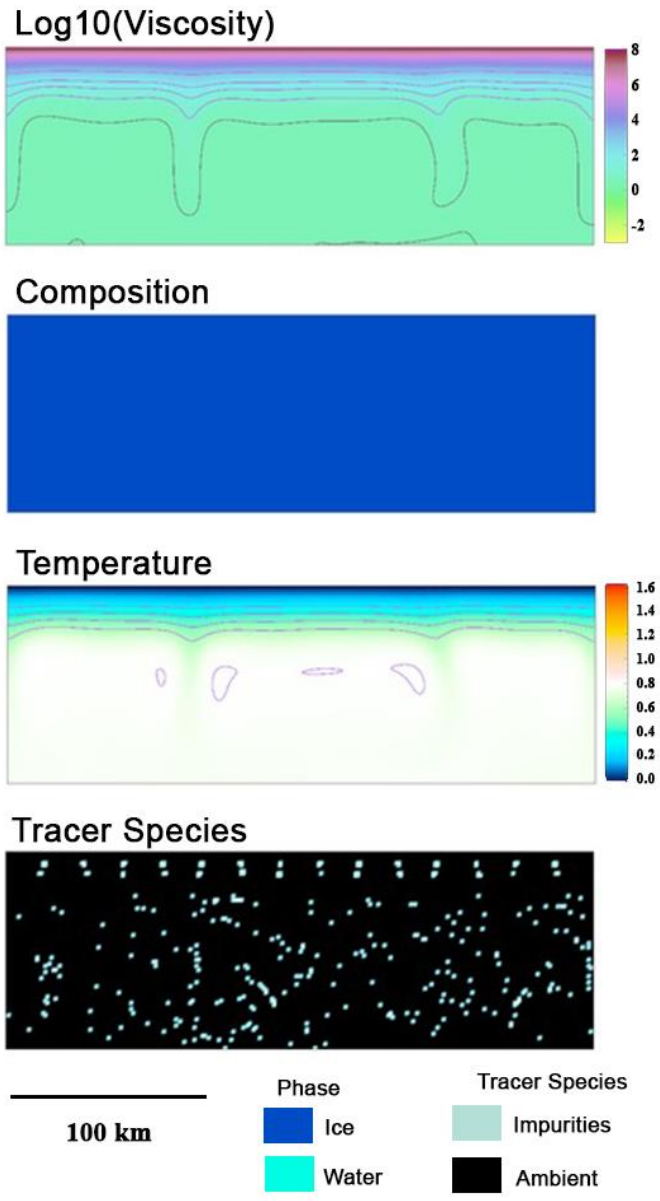

Figure 5.5. Distribution of tracers after freeze-over. Snapshot at 22 Myr since the beginning of the calculation. The top panel displays the logarithm of viscosity (yellow: low; purple: high) with the contours outlining each order of magnitude increase in viscosity. The second panel shows the composition (phase) where deep blue represents ice and the light blue represents the proxy fluid (the liquid ocean). The panel below it displays the temperature. The bottom panel shows the tracer species representing impurities in ice in whitish-green color, with black indicating ambient system.

The results of these experiments provide a simple demonstration of heterogeneity formation in the ice-shell. However, ideally the models would account for salinity of the ocean and include the effect of chemical composition of impurities on density (buoyancy) as well as the freezing and melting behavior of ice [*Zolotov and Kargel*, 2009]. We expect that inclusion of the chemical composition would thus affect the timescales as well as the detailed distribution pattern of the tracers. Additionally, localized brines are expected to enhance tidal dissipation which might also affect local ice-convection patterns [*Zolotov et al.*, 2004]. However, the general distribution pattern of tracers over time, i.e. its spatial entrapment within the ice-lid versus the entrainment into convection cells would still be expected, as shown in the numerical experiments in this study. We use a higher melting viscosity of ice than the range of viscosities generally used for Europa, which results in a lower Rayleigh number. We expect that employing a lower viscosity or higher Rayleigh number would change the vigor of convection, and hence the timescales involved. Consequently, any changes in the ice-shell thickness are not likely to change the general spatial pattern of tracers in different regions of the ice-shell.

In our models, destruction of heterogeneity only occurs if the tracers representing the impurities enter the ocean (fluid) layer. Hence the models predict that any impurities frozen in the ice-lid remain trapped perpetually. The high viscosity stagnant ice-lid is a consequence of the temperature-dependence of ice-viscosity and therefore, it can be proposed that any tectonic/ tidal fracturing of the surface could lead to the re-surfacing of the trapped material. Our numerical experiments are designed to simply test how evolving ice-convection patterns in a thickening shell mobilize impurities within the shell to form potential heterogeneity; with implications for depth-wise and time-wise

accumulation of non-ice material. The results of this study thus have implications for formation of brine pockets that have been hypothesized to be zones of structural weakness within the shell [*Schmidt et al*., 2011] as well as provide potential niches of habitability.

References

Allu Peddinti, D., & McNamara, A. K. (2015). Material transport across Europa's ice shell. *Geophys. Res. Lett., 42,* 4288-4293.

Anderson, J. D., Lau, E. L., Sjogren, W. l., Schubert, G., & Moore, W. B. (1998). Europa's differentiated internal structure: inferences from two Galileo encounters. *Nature, 276,* 1236-1239.

Billings, S. E., & Kattenhorn, S. A. (2005). The great thickness debate: Ice shell thickness models for Europa and comparisons with estimates based on flexure at ridges. *Icarus, 177,* 397–412.

Carlson, R. W., Anderson, M. S., Mehlman, R., & Johnson, R. E. (2005). Distribution of hydrate on Europa: further evidence for sulfuric acid hydrate. *Icarus, 177,* 461-471.

Eide, L., & Martin, S. (1975). The formation of brine drainage features in young sea ice. *J. Glaciol., 14,* 137-154.

Fanale, F. P., et al. (1999). Galileo's multi-instrument spectral view of Europa's surface composition. *Icarus, 139,* 179-188.

Golden, K. M., Ackley, S. F., & Lytle, V. I. (1998). The percolation phase transition in sea ice. *Science, 282,* 2238-2241.

Greeley, R., et al. (1998). Europa: Initial Galileo geological observations. *Icarus, 135,* 4-24.

Head, J. W., & Pappalardo, R. T. (1999). Brine mobilization during lithospheric heating on Europa: Implications for formation of chaos terrain, lenticula texture, and color variations. *J. Geophys., Res. 104,* 27143-27155.

Khurana, K. K., Kivelson, M. G., Stevenson, D. J., Schubert, G., Russell, C. T., Walker, R. J., & Polanskey, C. (1998). Induced magnetic fields as evidence for subsurface oceans in Europa and Callisto. *Nature, 395,* 777-780.

Kivelson, M. G., Khurana, K. K., Joy, S., Russell, C. T., Southwood, D. J., Walker, R. J., & Polanskey, C. (1997). Europa's magnetic signature: report from Galileo's pass on 19 December 1996. *Science, 276,* 1239-1241.

Light, B., Maykut, G. A., & Grenfell, T. C. (2003). Effects of temperature on microstructure of first-year Arctic sea ice. *J. Geophys. Res., 108*(C2), doi:10.1029/2001JC000887.

McCord, T. B., Hansen, G. B., Fanale, F. P., Carlson, R. W., Matson, D. L., Johnson, T. V., Smythe, W. D., Crowley, J. K., Martin, P. D., Ocampo, A., Hibbitts, C. A., Granahan, J. C., and the NIMS team. (1998). Salts on Europa's surface detected by Galileo's near infrared mapping spectrometer. *Science, 280,* 1242-1245.

McNamara, A. K., Garnero, E. J., & Rost, S. (2010). Tracking deep mantle reservoirs with ultra-low velocity zones. *Earth Planet. Sci. Lett*., *299*, 1–9.

Moresi, L., & Gurnis, M. (1996). Constraints on the lateral strength of slabs from three-dimensional dynamic flow models. *Earth Planet. Sci. Lett., 138,* 15–28.

Pappalardo, R. T., et al. (1999). Does Europa have a subsurface ocean? Evaluation of the geological evidence. *J. Geophys. Res.*, *104*(E10), 24015-24055.

Reeburgh, W. S. (1984). Fluxes associated with brine motion in growing sea ice. *Polar Biology, 3,* 29-33.

Schmidt, B. E., Blankenship, D. D., Patterson, G. W., & Schenk, P. M. (2011). Active formation of "chaos terrain" over shallow subsurface water on Europa. *Nature, 479*, 502–505.

Shreve, R. L. (1967). Migration of air bubbles, vapor figures, and brine pockets in ice under a temperature gradient. *J. Geophys. Res., 72*(16), 4093-4100.

Sotin, C., Head III, J. W., & Tobie, G. (2002). Europa: Tidal heating of upwelling thermal plumes and the origin of lenticulae and chaos melting. *Geophys. Res. Lett., 29*(23), 2109, doi:10.1029/2001GL013884.

Tackley, P. J., & King, S. D. (2003), Testing the tracer ratio method for modeling active compositional fields in mantle convection simulations. *Geochemistry Geophysics Geosystems*, *4*(4), 8302, doi:10.1029/2001gc000214.

Thomas, D. N., & Dieckmann, G. S., eds. (2003). *Sea Ice: An Introduction to its Physics, Chemistry, Biology, and Geology*. 416pp. Oxford: Blackwell Science.

Wakatsuchi, M., & Ono, N. (1983). Measurements of salinity and volume of brine excluded from growing sea ice. *J. Geophys. Res.*, *88*(C5), 2943-2951.

Zahnle, K., Schenk, P., Levison, H., & Dones, L. (2003). Cratering rates in the outer solar system. *Icarus*, *163*, 263-289.

Zolotov, M. Y., & Kargel, J. S. (2009). On the chemical composition of Europa's icy shell, ocean, and underlying rocks. *Europa*, edited by Pappalardo, R. T., McKinnon, W. B., & Khurana, K. K. Tucson: University of Arizona Press, pp 431-451.

Zolotov, M. Y., Shock, E. L., Barr, A. C., & Pappalardo, R. T. (2004). Brine pockets in the icy shell on Europa: distribution, chemistry, and habitability. *Lunar and Planetary Science Conference*, Abstract #7028.

CHAPTER 6

CONCLUDING REMARKS

Study of geodynamics of planetary ice-oceans such as that of Europa and Enceladus provides valuable insight into unraveling its geological history as well as predicting its habitability potential. Numerical modeling methods provide a powerful tool to define, scale down, and solve a geophysical problem. Constrained by observations, numerical solutions can not only reconcile the data with a physical process but also help predict the future behavior of the system. In this dissertation, I presented the results of numerical experiments to investigate the fluid dynamics of a self-consistently evolving two-phase pure-water-ice-ocean system with primary applications to the icy moon, Europa. The governing equations of the dynamics as well as the numerical methods used were summarized in Chapter 2.

In Chapter 3, I proposed and tested a hypothesis for material transport across Europa's ice-shell using geodynamical calculations. The models show that at the phase boundary between the ice-shell and the ocean layer, newly formed ice is convectively entrained into upwelling ice plumes in the shell. This newly formed ice is then transported across the ice-shell and towards the surface. The newly formed ice could potentially capture oceanic material, and thus this study demonstrates the potential of transport of oceanic material towards the surface, across a thick convecting ice-shell. Stagnant lid near the surface prevents the material from reaching the surface in our models; however tectonic and tidal weakening of the surface could allow the material to surface atop the shell.

In Chapter 4, I model the ice-shell formation from an initial warm ocean and examine the evolution of its thickness, and the growth rate in the presence of internal tidal heating. Diffuse and localized tidal heating modes of ice-shell are analyzed. The results show that the change in the ice-convection plan-form that occurs due to merging of ice-convection cells causes a dramatic increase in shell growth rate. This is confirmed for models with and without tidal heating in the ice. The addition of internal tidal heating, of sufficient magnitude, causes the ice-shell to attain an equilibrium thickness and prevents further freezing. Localization of tidal heating as a function of ice viscosity determines the equilibrium thickness of the ice-shell such that the ice-shell is thickest when maximum heat is localized under the high-viscosity lid and thinnest for maximum localization near the base of the shell.

The distribution of impurities as potential compositional heterogeneities in the ice-shell is examined in Chapter 5. We find that tracer spheres representing impurities that enter during the early stages of ice-shell formation, tend to be trapped in the stagnant lid unless the size of the spheres is too large. Over time, when second and third generation of tracer spheres are introduced at a greater depth, and as the ice-shell convection patterns change, these spheres are dragged along the convection cells. This leads to localization of heterogeneities in the downwelling regions of convection cells.

CHAPTER 7

RECOMMENDATIONS FOR FUTURE WORK

In the work presented in this dissertation, I investigated several aspects of a two-phase ice-ocean system including the transport of newly formed ice via ice-convection, the effect of tidal heating on the temporal change in ice-shell thickness as well as the entrapment of compositional heterogeneities in the forming ice-shell. This work examines shell dynamics in a simple, pure ice-water system under several assumptions. While not simulating the real *Europa*, the numerical experiments provide simple yet valid demonstration of the proposed hypotheses of material transport and shell evolution applicable to ice-ocean of Europa. However, these models can be further developed to explore the dynamics of ice-ocean system in a more realistic manner. Following are few of the factors that need to be considered and included in the future numerical models of two-phase ice-ocean system in order to better understand the icy moon evolution.

[1] *Salinity.* In this study, a pure water-ice phase is assumed in the system. A more realistic system should include the effect of salinity and hence incorporate a modified phase diagram that includes the effect of density variations due to the presence of salts. It would be interesting to study how convection in the presence of salts would affect formation of ice-shell in the two-phase system. Salt contamination of the ice would affect its melting point [*Kargel*, 1998; *Prieto-Ballesteros and Kargel*, 2005]. Dissolved salts in the ocean would reduce the freezing temperature and hence affect the ice-shell thickness. A saline system would also be expected to affect the material transport across the system. The presence of compositional heterogeneity or brine pockets in the ice-shell would be a

function of the salinity of the water and hence their formation and entrapment would also be modified by inclusion of a salinity factor.

[2] *Variable Tidal Dissipation.* It has been hypothesized that the tidal heating in ice has changed over geological time in conjunction with Europa's orbital configuration [*Hussmann and Spohn*, 2004]. It is also expected to change spatially across the ice-shell [*Mitri and Showman*, 2008]. This variation in the magnitude of tidal heating would also be expected to change the ice-shell thickness over time and perhaps lead to latitudinal variations in shell thickness. Thus the current model can be modified to include such spatiotemporal variation in the magnitude of tidal heating and determine its effect on ice-shell growth. Moreover, brine inclusions and other compositional species are expected to enhance localization of tidal heating and hence may be considered in future modeling experiments [*Zolotov and Kargel*, 2009].

[3] *Rheology of Ice.* The viscosity of ice-shell amongst other material properties of ice is important in determining the amount of tidal dissipation generated. In this study, ice is assumed to behave as a Newtonian fluid and its viscosity doesn't include any grain-size dependence. However, studies suggest that ice Ih viscosity is grain-size dependent under the temperature and stress conditions of ice-shell on Europa [*Barr et al.*, 2004; *Barr and Pappalardo*, 2005; *Barr and McKinnon*, 2007]. Thus, employing non-Newtonian rheology of ice in convection models is expected to effect the thermal evolution of the ice-shell and consequently, the heat flux and the thickness of the shell. Employing a non-Newtonian viscosity of ice in the two-phase models would also require to reformulate the tidal dissipation model used for ice which may provide a different path of ice-shell evolution.

[4] *3D Modeling.* The current study modeled the ice-ocean system in a two-dimensional domain. The next logical step would be to test these models in a three-dimensional geometry and analyze the change in results obtained. Spatial variations in both tidal dissipation and ice-shell thickness have been suggested [*Mitri and Showman*, 2008]. Tidal dissipation is expected to vary from the poles to equator. Hence, applying a 3D geometry is likely to affect the ice-shell formation over time, and hence the shell thickness at different latitudes. Lateral shell thickness variations, produced in the 3D domain, may also thus influence the material transport across the ice-shell as well as formation of compositional heterogeneities within the shell.

References

Barr, A. C., & McKinnon, W. B. (2007). Convection in ice I shells and mantles with self-consistent grain size. *J. Geophys. Res*., *112*, E02012, 10.1029/2006JE002781.

Barr, A. C., & Pappalardo, R. T. (2005). Onset of convection in the icy Galilean satellites: influence of rheology. *J. Geophys. Res.*, *110*, E12005, 10.1029/2004JE002371.

Barr, A.C., Pappalardo, R.T., & Zhong, S. (2004). Convective instability in ice I with non-Newtonian rheology: Application to the icy Galilean satellites. *J. Geophys. Res*., *109,* doi: 10.1029/2004JE002296.

Hussmann, H., & Spohn, T. (2004). Thermal-orbital evolution of Io and Europa. *Icarus, 171*, 391-410.

Kargel, J. (1998). Physical chemistry of ices in the outer Solar System. In *Solar System Ices,* edited by Schmitt, B. et al., pp. 3-32, Norwell: Kluwer Acad.

Mitri, G., & Showman, A.P. (2008). A model for the temperature-dependence of tidal dissipation in convective plumes in icy satellites: Implications for Europa and Enceladus. *Icarus, 195*, 758–764.

Prieto-Ballersteros, O., & Kargel, J. S. (2005). Thermal state and complex geology of a heterogeneous salty crust if Jupiter's satellite, Europa. *Icarus, 173,* 212-221.

Zolotov, M. Y., Shock, E. L., Barr, A. C., & Pappalardo, R. T. (2004). Brine pockets in the icy shell on Europa: distribution, chemistry, and habitability. *Lunar and Planetary Science Conference,* Abstract #7028.

REFERENCES

Alexander, C., Carlson, R., Consolmagno, G., Greeley, R., & Morrison, D. (2009). The Exploration history of Europa. In *Europa*, edited by Pappalardo, R. T., McKinnon, W. B., & Khurana, K. K. Tucson: University of Arizona Press, pp 3-26.

Allu Peddinti, D., & McNamara, A. K. (2015). Material transport across Europa's ice shell. *Geophys. Res. Lett*., *42*, 4288-4293.

Anderson, J. D., Lau, E. L., Sjogren, W. l., Schubert, G., & Moore, W. B. (1997). Europa's differentiated internal structure: inferences from two Galileo encounters. *Science*, *276*, 1236-1239.

Anderson, J. D., Schubert, G., Jacobsen, R. A., Lau, E. L., Moore, W. B., & Sjogren, W. L. (1998). Europa's differentiated internal structure: inferences from four Galileo encounters. *Science*, *281*, 2019-2022.

Barr, A. C., & McKinnon, W. B. (2007). Convection in ice I shells and mantles with self-consistent grain size. *J. Geophys. Res.*, *112*, E02012, doi:10.1029/2006JE002781.

Barr, A. C., & Pappalardo, R. T. (2005). Onset of convection in the icy Galilean satellites: influence of rheology. *J. Geophys., Res. 110*, E12005, 10.1029/2004JE002371.

Barr, A. C., & Showman, A. P. (2009). Heat Transfer in Europa's icy shell. In *Europa*, edited by Pappalardo, R. T., McKinnon, W. B., & Khurana, K., pp. 405-430, Tucson: Univ. of Arizona Press.

Barr, A.C., Pappalardo, R.T., & Zhong, S. (2004). Convective instability in ice I with non- Newtonian rheology: Application to the icy Galilean satellites. *J. Geophys. Res*., *109*, doi:10.1029/2004JE002296.

Bierhaus, E. B., Chapman, C. R., Merline, W. J., Brooks, S. M., & Asphaug, E. (2001). Pwyll secondaries and other small craters on Europa. *Icarus*, *153*, 264-276.

Billings, S. E., & Kattenhorn, S. A. (2005). The great thickness debate: ice shell thickness models for Europa and comparisons with estimates based on flexure at ridges. *Icarus, 177*, 397-412.

Canup, R.M., & Ward, W.R. (2009). *Origin of Europa and the Galilean Satellites*. In *Europa* edited by R. T. Pappalardo, W. B. McKinnon, and K. K. Khurana, pp. 431–451, Tucson: Univ. Arizona Press.

Carlson, R. W., Anderson, M. S., Mehlman, R., & Johnson, R. E. (2005). Distribution of hydrate on Europa: Further evidence for sulfuric acid hydrate. *Icarus, 177*, 461-471.

Carlson, R. W., Calvin, W. M., Dalton, J. B., Hansen, G. B., Hudson, R. L., Johnson, R. E., McCord, T. B., & Moore, M. H. (2009). Europa's Surface Composition. In *Europa* edited by R. T. Pappalardo, W. B. McKinnon, and K. K. Khurana, pp. 431–451, Tucson: Univ. Arizona Press.

Carr, M. H., Belton, M. J. S., Chapman, C. R., Davies, M. E., Geissler, P., Greenberg, R., McEwen, A. S., Tufts, B. R., Greeley, R., Sullivan, R., Head, J. W., Pappalardo, R. T., Klaasen, K. P., Johnson, T. V., Kaufman, J., Senske, D., Moore, J., Neukum, G., Schubert, G., Burns, J. A., Thomas, & P., Veverka, J. (1998). Evidence for a subsurface ocean on Europa. *Nature, 391*, 363-365.

Cassen, P., Reynolds, R. T., & Peale, S. J. (1979). Is there liquid water on Europa? *Geophys. Res. Lett., 6*, 731-734.

Collins, G. C., & Nimmo, F. (2009). Chaotic terrain on Europa. In *Europa* edited by R. T. Pappalardo, W. B. McKinnon, and K. K. Khurana, pp. 259–281, Tucson: Univ. Arizona Press.

Collins, G. C., Head, J. W., Pappalardo, R. T., & Spaun, N. A. (2000). Evaluation of models for the formation of chaotic terrain on Europa. *J. Geophys. Res., 105*, 1709-1716.

Cook, S. J., Waller, R. I., & Knight, P. G. (2006). Glaciohydraulic supercooling: The process and its significance. *Prog. Phys. Geogr., 30*(5), 577–588.

Craft, K. L., Patterson, W. & Lowell, R. T. (2013). Sill emplacement in Europa's ice shell as a mechanism for double ridge formation. In 44th *Lunar and Planetary Science Conference*, Woodlands, Texas.

Crameri, F., Tackley, P. J., Meilick, I., Gerya, T. V., & Kaus, B. J. P. (2012). A free plate surface and weak oceanic crust produce single-sided subduction on Earth. *Geophys. Res. Lett., 39*, L03306, doi:10.1029/2011GL050046.

Deschamps, F., & Sotin, C. (2001). Thermal convection in the outer shell of large satellites. *J. Geophys. Res., 106*, 5107-5121.

Dombard, A. J., Patterson, G. W., Lederer, A. P., & Prockter, L. M. (2012). Flanking fractures and the formation of double ridges on Europa. *Icarus*, *223*, 74-81.

Dunaeva, A. N., Antsyshkin, D. V., & Kuskov, O. L. (2010). Phase diagram of H_2O: thermodynamic functions of the phase transitions of high-pressure ices. *Solar Sys. Res., 44*, 202-222.

Durham, W. B., Prieto-Ballesteros, O., Goldsby, D. L., & Kargel, J. S. (2010). Rheological and thermal properties of icy materials. *Space Sci. Rev., 153*, 273-298.

Fagents, S. A. (2003). Considerations for effusive cryovolcanism on Europa: The post-Galileo perspective. *J. Geophys. Res., 108*(E12), 5139.

Figueredo, P. H., Chuang, F. C., Rathbun, J., Kirk, R. L., & Greeley, R. (2002). Geology and origin of Europa's mitten feature (Murias Chaos). *J. Geophys. Res., 107*, doi:10.1029/2001JE001591.

Fimmel, R. O., Swindell, W., & Burgess, E. (1974). *Pioneer Odyssey: Encounter with a Giant*. NASA SP-349, NASA Scientific and Technical Information Office, Washington, DC.

Fimmel, R. O., Van Allen, J. A., & Burgess, E. (1980). *Pioneer: First to Jupiter, Saturn and Beyond*. NASA SP-446, Washington DC.

Freeman, J., Moresi, L., & May, D. A. (2006). Thermal convection with a water ice I rheology: Implications for icy satellite evolution. *Icarus, 180*, 251-264.

Fricker, H. A., Popov, S., Allison, I., & Young, N. (2001). Distribution of marine ice beneath the Amery ice shelf. *Geophys. Res. Lett., 28*, 2241–2244, doi:10.1029/2000GL012461.

Galilei, G. (1610). *Siderius Nuncius*. Translated by E. S. Carlos (1929) in *A Source Book in Astronomy* (H. Shapley and Howarth, ed.). New York: McGraw-Hill.

Geissler, P. et al. (1998b). Evolution of lineaments on Europa: clues from Galileo multispectral imaging observations. *Icarus, 135*, 107-126.

Goldsby, D. L., & Kohlstedt, D. L. (2001). Superplastic deformation in ice: experimental observations. *J. Geophys. Res., 106,* 11017-11030.

Greeley, R., et al. (1998). Europa: Initial Galileo geological observations. *Icarus, 135*, 4-24.

Greeley, R., et al. (2000). Geological mapping of Europa. *J. Geophys. Res., 105,* 22559-22578.

Greeley, R., Sullivan, R., Klemaszewski, J., Homan, K., Head, J. W., Pappalardo, R. T., Veverka, J., Clark, B. E., Johnson, T. V., Klassen, K. P., Belton, M., Moore, J., Asphaug, E., Carr, M. H., Neukam, G., Denk. T., Chapman, C. R., Pilcher, C. B., Geissler, P., Greenberg, R., & Tufts, R. (1998). Europa: Initial Galileo geological observations. *Icarus, 135*, 4-24.

Greenberg, R., & Geissler, P. (2002). Europa's dynamic icy crust. *Meteoritics & Planetary Sci., 37,* 1685-1710.

Greenberg, R., et al. (1998). Tectonic processes on Europa: Tidal stresses, mechanical response, and visible features. *Icarus, 135*, 64–78.

Greenberg, R., Geissler, P., Hoppa, G., Tufts, B. R., Durda, D. D., Pappalardo, R., Head, J. W., Greeley, R., Sullivan, R., & Carr, M. H. (1998). Tectonic processes on Europa: tidal stresses, mechanical response, and visible features. *Icarus, 135*, 64-78.

Greenberg, R., Geissler, P., Tufts, B. R., & Hoppa G. V. (2000). Habitability of Europa's crust: The role of tidal-tectonic processes. *J. Geophys. Res., 105*, 17,551–17,562, doi:10.1029/1999JE001147.

Greenberg, R., Hoppa, G. V., Tufts, B. R., Geissler, P., Riley, J., & Kadel, S. (1999). Chaos on Europa. *Icarus, 141*, 263–286.

Han, L., & Showman, A. P. (2005). Thermo-compositional convection in Europa's ice shell with salinity. *Geophys. Res. Lett., 32*, L20201, doi:10.1029/2005GL023979.

Han, L., & Showman, A. P. (2011). Coupled convection and tidal dissipation in Europa's ice shell using non-Newtonian grain-size-sensitive (GSS) creep rheology. *Icarus, 212*, 262-267.

Han, L., & Showman, A.P. (2010). Coupled convection and tidal dissipation in Europa's ice shell. *Icarus*, doi:10.1016/j.icarus.2009.12.028.

Han, L., Tobie, G., & Showman, A. P. (2011). The impact of a weak south pole on thermal convection in Enceladus' ice shell. *Icarus*, *218*, 320-330.

Head, J. W., & Pappalardo, R. T. (1999). Brine mobilization during lithospheric heating on Europa: Implications for formation of chaos terrain, lenticula texture, and color variations. *J. Geophys. Res., 104*, 27143-27155.

Head, J. W., Pappalardo, R. T., & Sullivan, R. (1999). Europa: Morphological characteristics of ridges and triple bands from Galileo data (E4 and E6) and assessment of a linear diapirism model. *J. Geophys. Lett., 104*, 24223-24235.

Hoppa, G. V., & Tufts, B. R. (1999). Formation of cycloidal features on Europa. In *Lunar and Planetary Science XXX*, Abstract #1599.

Hoppa, G. V., Tufts, B. R., Greenberg, R., & Geissler, P. E. (1999a). Formation of cycloidal features on Europa. *Science, 285*, 1899-1902.

Hussmann, H., & Spohn, T. (2004). Thermal-orbital evolution of Io and Europa. *Icarus, 171*, 391-410.

Hussmann, H., Spohn, T., & Wieczerkowski, K. (2002). Thermal equilibrium states of Europa's ice shell: implications for internal ocean thickness and surface heat flow. *Icarus, 156*, 143-151.

Johnston, S. A., & Montesi, L. G. J. (2014). Formation of ridges on Europa above cyrstallizing water bodies inside the ice shell. *Icarus, 237*, 190-201.

Kadel, S. D., Fagents, S. A., Greeley, R., & the Galileo SSI Team. (1998). Trough-bounding ridge pairs on Europa – considerations for an endogenic model of formation. In *Lunar and Planetary Science XXIX*, Abstract #1078. Lunar Planetary Institute, Houston.

Kargel, J. (1998). Physical chemistry of ices in the outer Solar System. In *Solar System Ices*, edited by Schmitt, B. et al., pp. 3-32, Norwell: Kluwer Acad.

Kargel, J. S., Kaye, J. Z., Head, J. W., Marion, G. M., Sassen, R., Crowley, J. K., Ballesteros, O.P., Grant, S. A., & Hogenboom, D. L. (2000). Europa's crust and ocean: Origin, composition, and the prospects for life. *Icarus, 148*, 226–265.

Kattenhorn, S. A., & Prockter, L. M. (2014). Evidence for subduction in the ice shell of Europa. *Nature Geoscience, 7*, 762–767.

Khurana, K. K., Kivelson, M. G., Stevenson, D. J., Schubert, G., Russell, C. T., Walker, R. J., & Polanskey, C. (1998). Induced magnetic fields as evidence for subsurface oceans in Europa and Callisto. *Nature, 395*, 777-780.

Kivelson, M. G., Khurana, K. K., Joy, S., Russell, C. T., Southwood, D. J., Walker, R. J., & Polanskey, C. (1997). Europa's magnetic signature: report from Galileo's pass on 19 December 1996. *Science, 276*, 1239-1241.

Kivelson, M. G., Khurana, K. K., Russell, C. T., Volwerk, M., Walker, R. J., & Zimmer, C. (2000). Galileo magnetometer measurements: a stronger case for a subsurface ocean at Europa. *Science, 289,* 1340-1343.

Kuiper, G. P. (1957). Infrared observations of planets and satellites. *Astron. J., 62,* 291-306.

Lee, S., Pappalardo, R. T., & Makris, N. C. (2005). Mechanics of tidally driven fractures in Europa's ice shell. *Icarus, 177,* 367-379.

Lewis, E. L., & Perkin, R. G. (1986). Ice pumps and their rates. *J. Geophys. Res., 91,* 11,756–11,762, doi:10.1029/JC091iC10p11756.

Li, M., & McNamara, A. K. (2013). The difficulty for subducted oceanic crust to accumulate in upwelling mantle plume regions. *J. Geophys. Res., 118,* 1-10.

Li, M., McNamara, A. K., & Garnero, E. J. (2014). Chemical complexity of hotspots caused by cyclic oceanic crust through mantle reservoirs. *Nature Geoscience, 7,* 336-370.

Lipps, J. H., & Rieboldt, S. (2005). Habitats and taphonomy of Europa. *Icarus, 177,* 515-527.

Marion, G. M., Fritsen, C. H., Eicken, H., & Payne, M. C. (2003). The search for life on Europa: limiting environmental factors, potential habitats, and Earth analogues. *Astrobiology, 3*:785–811.

McCollom, T. M. (1999). Methanogenesis as a potential source of chemical energy for primary biomass production by autotrophic organisms in hydrothermal systems on Europa. *J. Geophys. Res., 104*(E12), 30729-30742.

McCord, T. B., Hansen, G. B., Fanale, F. P., Carlson, R. W., Matson, D. L., Johnson, T. V., Smythe, W. D., Crowley, J. K., Martin, P. D., Ocampo, A., Hibbitts, C. A., Granahan, J. C., and the NIMS team. (1998). Salts on Europa's surface detected by Galileo's near infrared mapping spectrometer. *Science, 280,* 1242-1245.

McCord, T. B., Teeter, G., Hansen, G. B., Sieger, M. T., & Orlando, T. M. (2002). Brines exposed to Europa surface conditons. *J. Geophys. Res., 107*(E1), 5004, 10.1029/2000JE001453.

McKinnon, W. B. (1999). Convective instability in Europa's floating ice shell. *Geophys. Res. Lett., 7*, 951–954, doi:10.1029/1999GL900125.

McNamara, A. K., Garnero, E. J., & Rost, S. (2010). Tracking deep mantle reservoirs with ultra-low velocity zones. *Earth and Planetary Science Letters*, *299*(1-2), 1-9, doi:10.1016/j.epsl.2010.07.042.

Michaut, C., & Manga, M. (2014). Domes, pits, and small chaos on Europa produced by water sills. *J. Geophys. Res. Planets*., *119*, doi: 10.1002/2013JE004558.

Mitri, G., & Showman, A. P. (2005). Convective-conductive transitions and sensitivity of a convecting ice shell to perturbations in heat flux and tidal-heating rate: implications for Europa. *Icarus, 177*, 447-460.

Mitri, G., & Showman, A.P. (2008). A model for the temperature-dependence of tidal dissipation in convective plumes in icy satellites: Implications for Europa and Enceladus. *Icarus, 195*, 758–764.

Moore, M. H., Hudson, R. L., & Carlson, R. W. (2007). The radiolysis of SO2 and H2S in water ice: implications for the icy jovian satellites. *Icarus, 189*, 409-423.

Moresi, L. N., & Solomatov, V. S. (1995). Numerical Investigation of 2d Convection with Extremely Large Viscosity Variations. *Physics of Fluids*, *7*(9), 2154-2162, doi:10.1063/1.868465.

Moresi, L., & Gurnis, M. (1996). Constraints on the lateral strength of slabs from three dimensional dynamic flow models. *Earth and Planetary Science Letters*, *138*(1-4), 15-28, doi:10.1016/0012-821x(95)00221-W.

Nimmo, F., & Gaidos, E. (2002). Strike-slip motion and double ridge formation on Europa. *J. Geophys. Res., 107*(E4), 5021, doi:10.1029/2000JE001476.

Nimmo, F., & Manga, M. (2009). Geodynamics of Europa's Icy Shell. *Europa*, edited by Pappalardo, R. T., McKinnon, W. B., & Khurana, K. K. Tucson: University of Arizona Press, pp 381-400.

Nimmo, F., Giese, B., & Pappalardo, R. T. (2003). Estimates of Europa's ice shell thickness from elastically-supported topography. *Geophys. Res. Lett.*, *20*, 10.1029/2002GL016660, 1233.

Nimmo, F., Prockter, L., & Schenk, P. (2005). Europa's icy shell: past and present state, and future exploration. *Icarus, 177*, 293-296.

O'Brien, D. P., Geissler, P., & Greenberg, R. (2002). A melt-through model for chaos formation on Europa. *Icarus, 156*, 152–161.

Ojakangas, G. W., & Stevenson, D. J. (1989). Thermal state of an ice shell on Europa. *Icarus*, *81*, 220-241.

Pappalardo, R. T., & Barr, A. C. (2004). The origin of domes on Europa: The role of thermally induced compositional diapirism. *Geophys. Res. Lett*., *31*, L01701, doi:10.1029/2003GL019202.

Pappalardo, R. T., & Head, J. W. (2001). The thick-shell model of Europa's geology: implications for crustal processes. In *Lunar and Planetary Science Conference XXXII*, Abstract #1866. Lunar Planetary Institute, Houston.

Pappalardo, R. T., et al. (1999). Does Europa have a subsurface ocean? Evaluation of the geological evidence. *J. Geophys. Res.*, *104*(E10), 24015-24055.

Pappalardo, R. T., Head, J. W., Greeley, R., Sullivan, R. J., Pilcher, C., Schubert, G., Moore, W. B., Carr, M. H., Moore, J. M., Belton, M. J. S., & Goldsby, D. L. (1998). Geological evidence for solid-state convection in Europa's ice shell. *Nature, 291*, 365-368.

Pappalardo, R., & Coon, M. D. (1996). A sea ice analog for the surface of Europa. In *Lunar and Planetary Science Conference XXVII*, pp. 997-998. Lunar Planetary Institute, Houston.

Pilcher, C. B., Ridgeway, S. T., & McCord, T. B. (1972). Galilean satellites: Identification of water frost. *Science, 178*, 1087-1089.

Price, P. B. (2003). Life in solid ice on Earth and other planetary bodies. In *Bioastronomy* 2002: Life among the stars. In: Norris R and Stootman F (eds) IAU Symposium series no. *213*, pp 363–366.

Prieto-Ballersteros, O., & Kargel, J. S. (2005). Thermal state and complex geology of a heterogeneous salty crust if Jupiter's satellite, Europa. *Icarus. 173*, 212-221.

Prockter, L. M., & Pappalardo, R. T. (2000). Folds on Europa: Implications for crustal cycling and accommodation of extension. *Science, 289*, 941–943.

Prockter, L. M., Head, J., Pappalardo, R., Sullivan, R., Clifton, A. E., Gliese, B., Wagner, R., & Neukum, G. (2002). Morphology of Europan bands at high resolution: A mid-ocean ridge-type rift mechanism. *J. Geophys. Res. 107*, 1-26.

Rathbun, J., Musser Jr, G. S., & Squyres, S. W. (1998). Ice diapirs on Europa: implications for liquid water. *Geophys. Res. Lett., 25*, 4157-4160.

Robin, E. B., Tinto, K., Das, I., Wolovick, M., Chu, W., Creyts, T. T., Frearson, N., Abdi, A., & Paden, J. D. (2014). Deformation, warming and softening of Greenland's ice by refreezing meltwater. *Nature Geoscience, 7*, 497–502.

Rudolph, M. L., & Manga, M. (2009). Fracture penetration in planetary ice shells. *Icarus, 199*, 536-541.

Ruiz, J., & Fairen, A. G. (2005). Seas under ice: stability of liquid-water oceans within icy worlds. *Earth, Moon, and Planets, 97*, 79-90.

Ruiz, J., Montoya, L., Lopez, V., & Amils, R. (2007). Thermal diapirism and the habitability of the icy shell of Europa. *Orig. Life. Evol. Biosph., 37*, 287-295.

Schenk, P. M. (2002). Thickness constraints on the icy shells of the Galilean satellites from a comparison of crater shapes. *Nature, 417*, 419-421.

Schenk, P. M., & Pappalardo, R. (2004). Topographic variations in chaos on Europa: implications for diapiric formation. *Geophys. Res. Lett., 31*, L1703, doi:10.1029/2004GL019978.

Schenk, P. M., Chapman, C. R., Zahnle, K. M., & Jeffrey, M. (2004). Ages and interiors: The cratering record of the Galilean satellites. *Jupiter: The Planet, Satellites and Magnetosphere* edited by Bagenal, F. et al. Cambridge: Cambridge Univ., pp. 427-456.

Schmidt, B. E., Blankenship, D. D., Patterson, G. W., & Schenk, P. M. (2011). Active formation of "chaos terrain" over shallow subsurface water on Europa. *Nature, 479*, 502–505.

Schubert, G., Turcotte, D. L., & Olson, P. (2001). *Mantle Convection in the Earth and Planets*. Cambridge: Cambridge University Press.

Showman, A. P., & Han, L. (2004). Numerical simulations of convection in Europa's ice shell: Implications for surface features. *J. Geophys. Res., 109*, E01010, doi:10.1029/2003JE002103.

Showman, A.P., & Han, L. (2005). Effects of plasticity on convection in an ice shell: Implications for Europa. *Icarus, 177*, 425–437.

Smith, B. A., & the Voyager Imaging Team. (1979). The Galilean satellites of Jupiter: Voyager 2 imaging science results. *Science, 206*, 951-972.

Soderlund, K. M., Schmidt, B. E., Wict, J., & Blankenship, D. D. (2014). Ocean dynamics of Europa: Implications for chaos distribution and ice-ocean coupling. *Nature Geoscience, 7*, 16–19.

Sotin, C., Choblet, G., Head, J. W., Mocquet, A., & Tobie, G. (2004). Thermal evolution of Europa's icy crust. In: *Workshop on Europa's Icy Shell: Past, Present, and Future*, LPI Contribution No. 1195. Lunar and Planetary Institute, Houston, pp. 84-85.

Sotin, C., Head III, J. W., & Tobie, G. (2002). Europa: Tidal heating of upwelling thermal plumes and the origin of lenticulae and chaos melting. *Geophys. Res. Lett., 29*(23), 2109, doi:10.1029/2001GL013884.

Spaun, N. A., Head, J. W., Collins, G. C., Prockter, L. M., & Pappalardo, R. T. (1998). Conamara chaos region, Europa: Reconstruction of mobile polygonal ice blocks. *Geophys. Res. Lett., 25*, 4277–4280.

Spencer, J. R., Grundy, W. M., Dumas, C., Carlson, R. W., McCord, T. B., Hansen, G. B., & Terrile, R. J. (2006). The nature of Europa's dark non-ice surface material: spatially resolved high spectral resolution spectroscopy from the Keck telescope. *Icarus, 182*, 202-210.

Spencer, J. R., Tamppari, L. K., Martin, T. Z., & Travis, L. D. (1999). Temperatures on Europa from Galileo Photopolarimeter-radiometer: nighttime thermal anomalies. *Science, 284*, 1514-1516.

Spohn, T., & Schubert, G. (2003). Oceans in the icy Galilean satellites of Jupiter? *Icarus, 161*, 456-467.

Stengel, K. C., Oliver, D. S., & Booker, J. R. (1982). Onset of convection in a variable-viscosity fluid. *J. Fluid Mech., 120*, 411-431.

Sullivan, R., et al. (1998). Episodic plate separation and fracture infill on the surface of Europa. *Nature, 391*, 371–373.

Sullivan, R., Greeley, R., Homan, K., Klemaszewski, J., Belton, M. J. S., Carr, M. H., Chapman, C. R., Tufts, R., Head III, J. W., Pappalardo, R., Moore, J., Thomas, P., & the Galileo Imaging Team. (1998). Episodic plate separation and fracture infill on the surface of Europa. *Nature, 391*, 371-373.

Tackley, P. J. (2000b). Self-consistent generation of tectonic plates in time-dependent, three-dimensional mantle convection simulations. 1. Pseudoplastic yielding. *Geochem. Geophys. Geosyst., 1*, 2000GC000036.

Tackley, P. J., & King, S. D. (2003). Testing the tracer ratio method for modeling active compositional fields in mantle convection simulations. *Geochemistry Geophysics Geosystems*, *4*(4), 8302, doi:10.1029/2001gc000214.

Takeushi, H., & Saito, M. (1972). Seismic surface waves. In *Methods in Computational Physics*, Vol. 1, edited by Bolt, B. A., pp. 217-295. New York: Academic.

Tobie, G., Choblet, G., & Sotin, C. (2003). Tidally heated convection: Constraints on Europa's ice shell thickness. *J. Geophys. Res.*, *108*(E11), 5124, doi:10.1029/2003JE002099.

Tobie, G., Mocquet, A., & Sotin, C. (2005). Tidal dissipation within large icy satellites: Applications to Europa and Titan. *Icarus*, *177*, 534-549.

Tufts, B. R., Greenberg, R., Hoppa, G., & Geissler, P. (1999). Astypalaea Linea: A large scale strike-slip fault on Europa. *Icarus*, *141*, 53-64.

Tufts, B. R., Greenberg, R., Hoppa, G., & Geissler, P. (2000). Lithospheric dilation on Europa. *Icarus*, *146*, 75-97.

Turcotte, D. L., & Schubert, G. (2002). Geodynamics: Applications of Continuum Physics to Geological Problems. New York: Wiley.

Turtle, E. P., & Pierazzo, E. (2001). Thickness of an Europan ice shell from impact crater simulations. *Science*, *294*, 1326-1328.

Turtle, E. P., Melosh, H. J., & Phillips, C. B. (1998). Tectonic modeling of the formation of europan ridges. *Eos Trans. AGU.*, *79*, F541.

Van Keken, P. E., King, S. D., Schmeling, H., Christensen, U. R., Neumister, D., & Doin, M.-P. (1997). A comparison of methods for the modeling of thermochemical convection. *J. Geophys. Res.*, *102*, 22,477–22,495, doi:10.1029/97JB01353.

Vance, S., & Goodman, J. C. (2009). Oceanography of an ice-covered moon. *Europa*, edited by R. T. Pappalardo,W. B.McKinnon, and K. K. Khurana, pp. 459–482, Tucson: University of Arizona Press.

Wang, H., & Stevenson, D. J. (2000). Convection and internal melting of Europa's ice shell. In *Lunar and Planetary Science XXXI*, Abstract #1293. Houston: Lunar and Planetary Institute.

Warren, S. G., Brandt, R. E., Grenfell, T. C., & McKay, C. P. (2002). Snowball Earth: Ice thickness on the tropical ocean. *J. Geophys. Res., 107*(C10), 3167, doi:10.1029/2001JC001123.

Watts, A. B. (2001). *Isostasy and Flexure of the Lithosphere*. Cambridge: Cambridge Univ.

Zahnle, K., Schenk, P., Levison, H., & Dones, L. (2003). Cratering rates in the outer solar system. *Icarus, 163*, 263-289.

Zolotov, M. Y., & Kargel, J. S. (2009). On the chemical composition of Europa's icy shell, ocean, and underlying rocks. *Europa*, edited by R. T. Pappalardo, W. B. McKinnon, and K. K. Khurana, pp. 431–451, Tucson: University of Arizona Press.

Zolotov, M. Y., Shock, E. L., Barr, A. C., & Pappalardo, R. T. (2004). Brine pockets in the icy shell on Europa: distribution, chemistry, and habitability. *Lunar and Planetary Science Conference*, Abstract #7028.

APPENDIX A

PROXY FLUID APPROXIMATION

Liquid water has very low viscosity compared to solid ice. Since our calculations do not aim at modeling the dynamics of the ocean part of the system, we propose to introduce a proxy fluid in lieu of liquid water while still sufficiently approximating the ice-ocean system. The large viscosity contrast between solid ice and liquid water decouples the dynamics of the two layers in Europa, assuming that any possible phase gap between solidus and liquidus plays a negligible role in viscous coupling. We adjust the viscosity of the proxy fluid in order to achieve this decoupling of convective dynamics. The proxy fluid thus has a viscosity higher than that of liquid water but still much lower than that of solid ice. We achieve this by continually decreasing the proxy fluid viscosity by an order of magnitude until we find that further decrease does not significantly affect the overall dynamics of the ice system (i.e. sufficient decoupling is achieved). We performed this exercise for different melting viscosities of ice (η_m ~10^{18} – 10^{15} Pa-s) and concluded that using a fluid viscosity value which is at least a hundredth of the melting viscosity of ice and more appropriately a thousandth the melting viscosity of ice, conveniently approximates the decoupling of the two layers in the real system. This means that any further decrease of proxy fluid viscosity does not affect the dynamics within the ice-shell considerably, and hence, we use the minimum requirement to increase the computational efficiency and make the problem tractable.

In order to demonstrate the proxy fluid approximation in figures A1 through A3, we define a viscosity contrast as the ratio between the proxy fluid viscosity and the lowest viscosity of ice (i.e the melting viscosity of ice). Therefore,

Viscosity contrast = Ratio of viscosity of proxy fluid to melting viscosity of the ice

$$\Delta\eta = \frac{\eta_{proxy\,fluid}}{\eta_m} \quad \text{(A.1)}$$

Where the numerator is the proxy fluid viscosity and η_m is the melting viscosity of ice as defined in our models (10^{18} – 10^{15} Pa-s).

Figure A1 illustrates how shell-ocean decoupling for fixed values of η_m and ΔT depends upon the value of $\Delta\eta$. Five snapshots are shown, each corresponding to a different value of $\Delta\eta$. In each snapshot, the three panels from top to bottom display the logarithm of viscosity, the phase and the temperature. For a given ΔT, the shell convection patterns change with decreasing viscosity contrast. The coupling of convection patterns in the ice and the fluid layers decreases with every order of magnitude decrease in the viscosity contrast (i.e. the viscosity of the proxy fluid), as shown in the temperature field. We notice that a proxy fluid viscosity that is at least 100x less than the lowest ice-viscosity provides sufficient decoupling of convection between the ice and fluid layers for our numerical study. Further decrease in proxy fluid viscosity while being more accurate approximation of the real ice-ocean system is desirable but not necessary condition for our modeling experiments. In all the snapshots shown, because the low viscosity proxy-fluid convects more vigorously (resulting in increased heat loss and a thinner ice-shell), the value of numerical parameter ΔT needs to be decreased accordingly to allow a thicker ice-shell to develop by reducing the heat in the system.

Figure A2 further demonstrates how the numerical parameter ΔT can be used to control the ice-shell thickness. For a fixed melting viscosity of ice and a fixed proxy fluid viscosity, the value of ΔT can be adjusted to achieve a system where there is no bulk freezing and melting at the interface i.e. the ice-shell thickness can be held constant. In

Chapter 3, we use such a *stable* system in order to track only the new ice formed at the interface that is entrained in the ice plumes. Increasing the value of this parameter when other parameters are fixed, results in a progressively thinner ice-shell as shown in the composition panel of the snapshots.

The proxy fluid approximation is further demonstrated in figure A3. Here we fix the values of both melting viscosity of ice and the numerical parameter ΔT. The viscosity of the proxy fluid is reduced by an order of 10 from one case to another. The apparent decoupling of convection in the ice and the fluid layers that is achieved by lowering the proxy fluid viscosity is shown in the temperature field. Here we note that when other parameters are fixed, the decoupling of convection by reducing the proxy fluid viscosity determines the thickness of the ice-shell. The lower the fluid viscosity, the thinner the ice-shell, as shown in the phase panel. Upon investigation of this approximation for other values of melting viscosity of ice, we concluded that a hundredth of the ice-viscosity works as a suitable upper limit while a thousandth of ice-viscosity is most appropriate for approximating the decoupled convection in an ice-ocean system analogous to that of Europa, for the hypotheses tested in our numerical experiments.

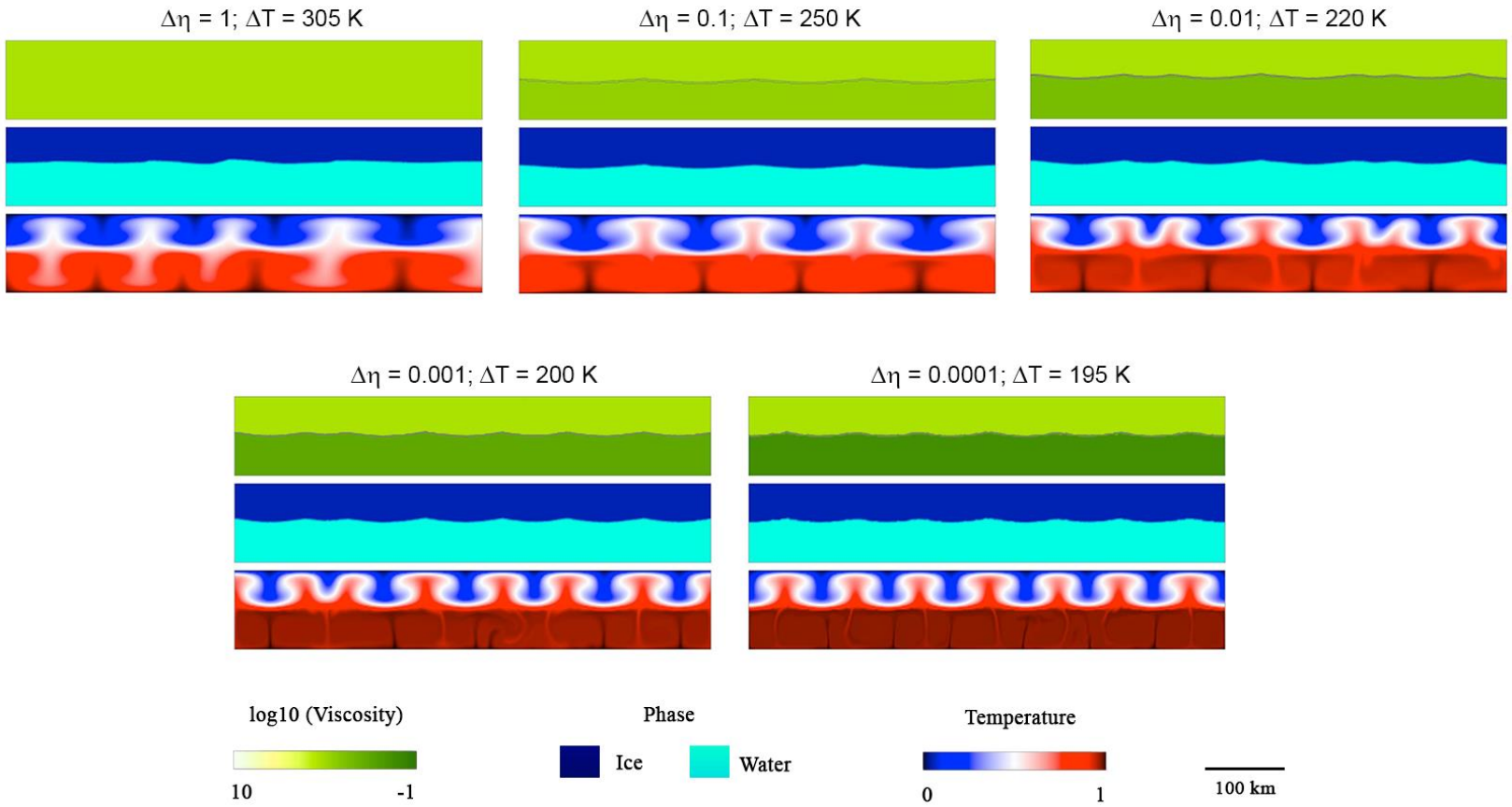

Figure A1. Exploring the low viscosity proxy fluid approximation. Snapshots from five cases are shown here to demonstrate the low viscosity proxy fluid approximation used in our models. Three panels are shown in each snapshot. The top panel shows the logarithm of viscosity, the middle panel shows the phase – the light blue layer represents the proxy fluid while the darker blue phase represents the solid ice. The bottom panel displays the temperature. The melting viscosity of ice (η_m) in all the cases is fixed at 10^{18} Pa-s. The ratio of the viscosity of the proxy fluid to the melting viscosity of ice indicated by $\Delta\eta$ is varied such that from first case to the last case, the viscosity of proxy fluid is reduced by an order of 10 relative to the previous case. Therefore, in the last case the viscosity of proxy fluid is 1/10,000th that of the lowest ice viscosity. The numerical parameter ΔT, as explained in the text, is adjusted for each case such that a stable convecting system is attained.

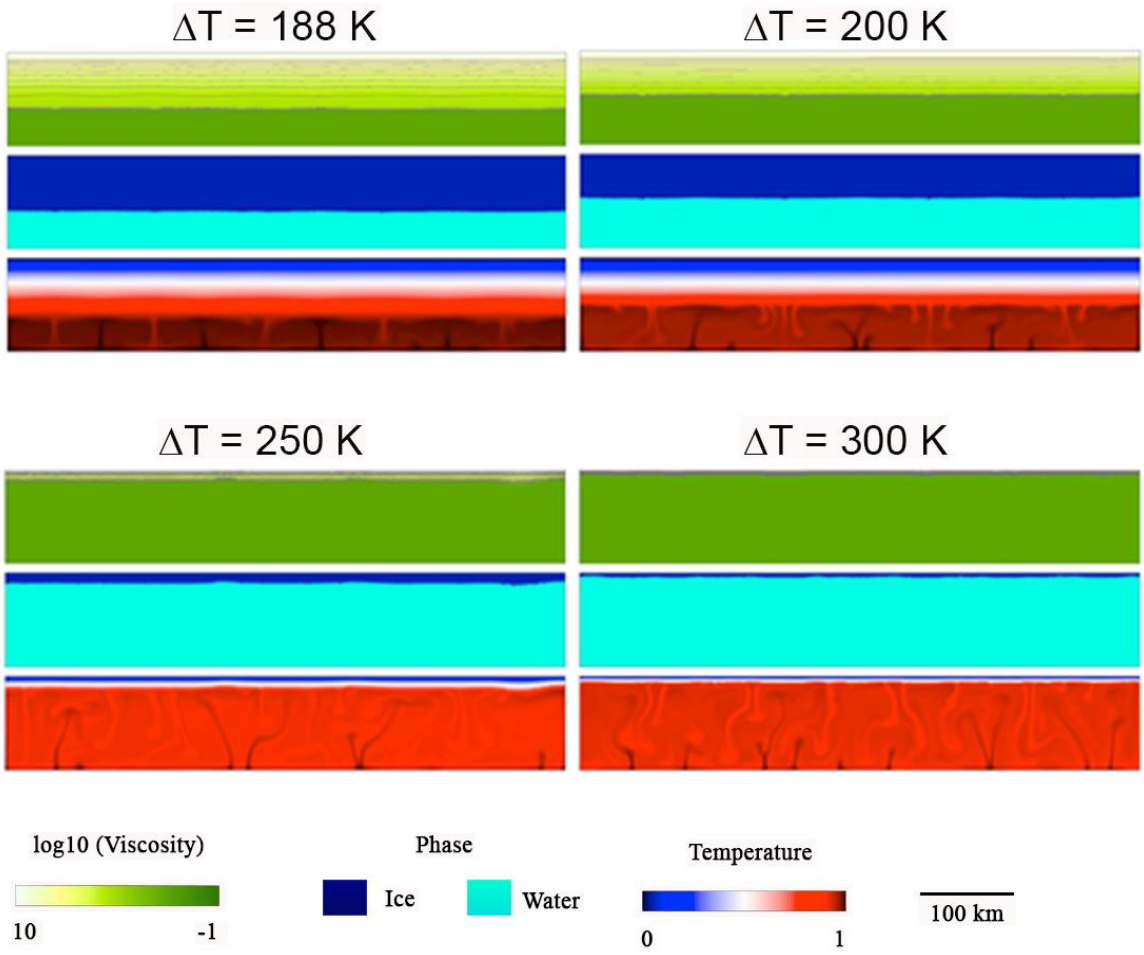

Figure A2. Demonstration of the numerical parameter ΔT in the two-phase models. Snapshots of four cases are shown here with a fixed melting viscosity of 10^{18} Pa-s and a fixed proxy fluid viscosity value equivalent to a 1/1,000th of the melting viscosity of ice. Each snapshot has three panels – the top panel shows the logarithm of the viscosity, the middle panel shows the phase – the light blue represents the proxy fluid and the darker blue represents the solid ice. The bottom panel shows the temperature. The value of the temperature contrast across the system represented by the numerical parameter ΔT is modified in each case. A stable convecting system is a two-phase convecting system where there is no bulk freezing or melting and is controlled by this numerical parameter.

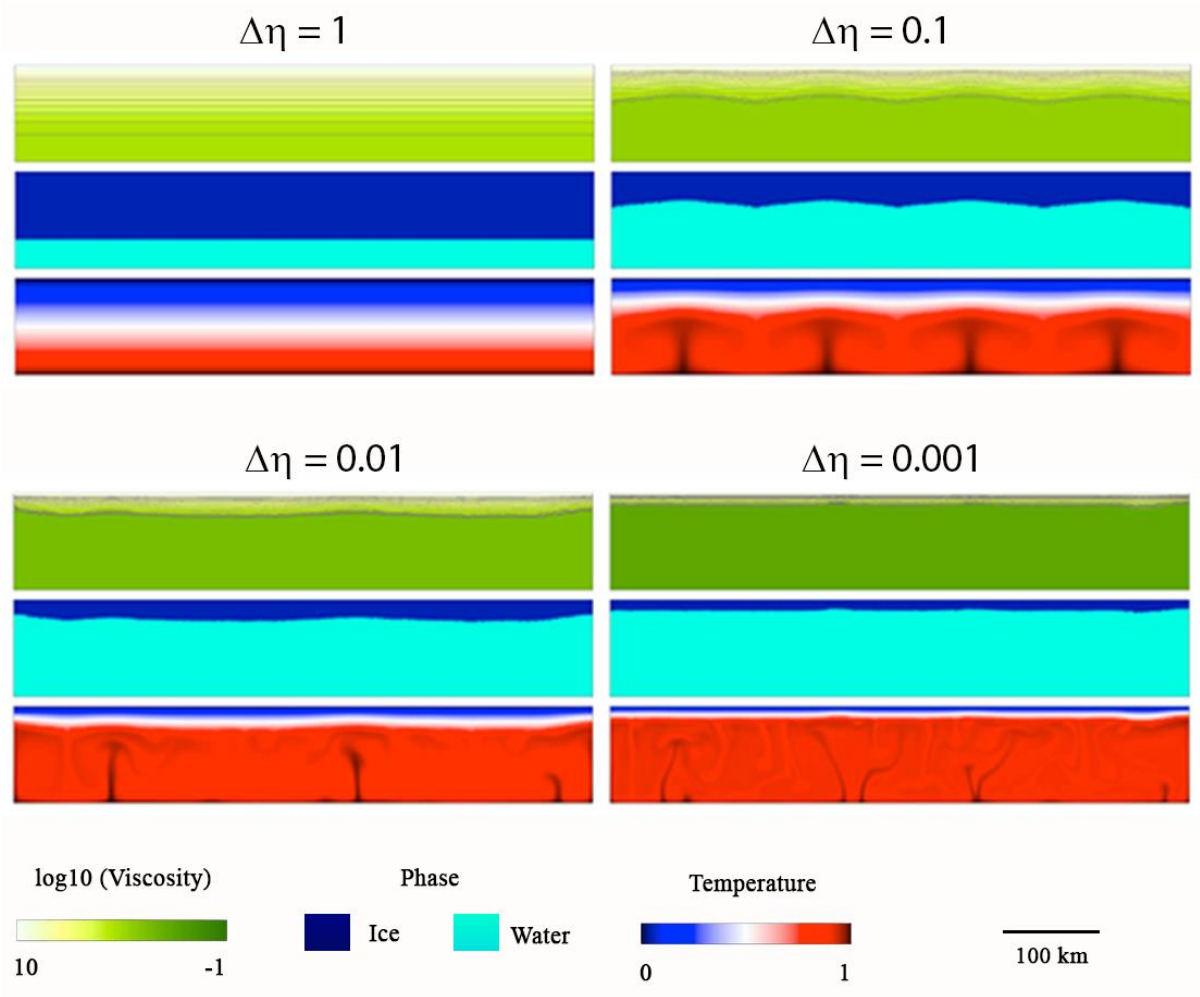

Figure A3. Effect of viscosity of proxy fluid on formation of two-phase convection system. Snapshots of four cases with decreasing viscosities of proxy fluid are shown here. Each snapshot has three panels – the top panel shows the logarithm of viscosity, the middle panel shows the phase with light blue representing proxy fluid and darker blue representing ice, and the bottom panel shows the temperature. The melting viscosity of ice (η_m) in all the four cases shown is fixed at 10^{18} Pa-s. The temperature contrast across the system represented by the numerical parameter ΔT is also fixed. $\Delta\eta$ indicates the ratio of viscosity of the proxy fluid to the lowest viscosity of ice. Hence, in the first case, the viscosities of the ice and proxy fluid are equal while in the last case, the proxy fluid is 1,000 times less viscous than the lowest viscosity ice.